INDOOR POSITIONING USING ACOUSTIC PSEUDO-NOISE BASED TIME DIFFERENCE OF ARRIVAL

A Thesis

presented to

the Faculty of California Polytechnic State University,

San Luis Obispo

In Partial Fulfillment

of the Requirements for the Degree

Master of Science in Electrical Engineering

by

Nicholas Joseph Luong

June 2020

COMMITTEE MEMBERSHIP

TITLE: Indoor Positioning Using Acoustic Pseudo-Noise Based Time Difference of Arrival

AUTHOR: Nicholas Joseph Luong

DATE SUBMITTED: June 2020

COMMITTEE CHAIR: Vladimir Prodanov, Ph.D.

Associate Professor of Electrical Engineering

COMMITTEE MEMBER: Wayne Pilkington, Ph.D.

Associate Professor of Electrical Engineering

COMMITTEE MEMBER: Fred W. DePiero, Ph.D.

Professor of Electrical Engineering

ABSTRACT

Indoor Positioning Using Acoustic Pseudo-Noise Based Time Difference of Arrival

Nicholas Joseph Luong

The Global Positioning System (GPS) provides good precision on a global scale, but is not suitable for indoor applications. Indoor positioning systems (IPS) aim to provide high precision position information in an indoor environment. IPS has huge market opportunity with a growing number of commercial and consumer applications especially as Internet of Things (IoT) develops. This paper studies an IPS approach using audible sound and pseudo-noise (PN) based time difference of arrival (TDoA). The system's infrastructure consists of synchronized speakers. The object to be located, or receiver, extracts TDoA information and uses multilateration to calculate its position. The proposed IPS utilizes sound waves since they travel much slower compared to electromagnetic waves, allowing for easier measurements. Additionally, the audible spectrum has a large availability of low directivity speakers and microphones allowing for a large coverage area compared to highly directive ultrasonic transceivers. This paper experimentally evaluates the feasibility of the proposed IPS.

Keywords: Indoor Positioning, Sensor Network, Ranging, TDoA, Pseudo-Noise, PN, Acoustic, Audible Sound, Time Reversal

ACKNOWLEDGMENTS

To Dr. Prodanov, thank you for being such an excellent teacher and advisor. It has been an honor learning from you in your classes and being your Master's student. The success of this thesis is largely due to your advising. Your knowledge and passion for EE is inspiring. I thoroughly enjoyed studying under you.

To Dr. Pilkington and Dr. DePeiro, thank you for serving on the committee and providing valuable feedback to my thesis.

To the Cal Poly EE department, thank you for reimbursing parts purchased for this thesis.

To my friends and classmates, thank you for all of the fun memories and technical discussions, even at late hours of the night.

To my mom, dad, brother and sisters, thank you for your love, support and encouragement. You are the reason I work hard, and I would not be where I am today without you.

To my grandmother, Nana, who lives in San Luis Obispo, thank you for all the Sunday dinners we have had over the last five years. I feel so blessed to have had you close by throughout my college experience.

TABLE OF CONTENTS

LIST OF TABLES

Table Page

LIST OF FIGURES

Figure Page

1 INTRODUCTION

1.1 Statement of Problem

Position location is vital information that enables a variety of applications. The Global Positioning System (GPS) provides good precision on a global scale, but is not suitable for indoor applications. Thus, there is a void of high precision coverage for indoor applications. Indoor positioning systems (IPS) aim to provide high precision position information in an indoor environment. IPS is a rapidly changing field that is attracting interest for its big market opportunity to apply the technology [1].

IPS are complex systems that involve all electrical engineering disciplines and requires knowledge of the full system to make informed design decisions. There are many factors that affect system performance. Some major factors this paper focuses on includes system impulse response, code tracking, sampling frequency, transmitter locations, and the positioning algorithm. Studying these problems requires knowledge of communications theory, digital signal processing (DSP), analog design, digital design, and programming.

1.2 List of Terms

Table 1.1: List of terms

AC	Alternating Current
ADC	Analog to Digital Converter
AoA	Angle of Arrival
AUX	Auxiliary
CDMA	Code Division Multiple Access
DC	Direct Current
DLL	Delay Locked Loop
DSP	Digital Signal Processing
DSSS	Direct Sequence Spread Spectrum
FIR	Finite Impulse Response
FPGA	Field Programmable Gate Array
GPS	Global Positioning System
HP	Hewlett-Packard
IPS	Indoor Positioning System

IV	Current-Voltage
KVL	Kirchhoff's Voltage Law
LFSR	Linear Feedback Shift Register
LMS	Least Mean Squared
LPF	Low Pass Filter
LTI	Linear Time-Invariant
MCU	Microcontroller
MLS	Maximum Length Sequence
m-Sequence	Maximum Length Sequence
PMOD	Peripheral Module Interface
PN	Pseudo-noise
PSD	Power Spectral Density
RAIM	Receiver Autonomous Integrity Monitoring
RF	Radio Frequency
RSS	Received Signal Strength
Rx	Receiver
TDoA	Time Difference of Arrival
ToA	Time of Arrival
TP1	Test Point 1
TR	Time Reversal
Tx	Transmitter
2D	2-Dimensional
3D	3-Dimensional

1.3 Purpose of Study

Studying acoustic IPS advances the field of IPS and adds to the literature. Current literature still studies both ultrasonic [2] [3] [4] [5], and audible sound [6] [7] [8] [9] IPS in search of a practical solution to the IPS problem. Despite the obvious drawback that humans can hear an acoustic IPS, an acoustic IPS still has great potential to achieve sub-centimeter accuracy and provide greater coverage than an ultrasonic system. For this reason, the study of acoustic based IPS is very important to the IPS field.

2 BACKGROUND

2.1 Indoor Positioning Systems

Indoor positioning systems (IPS) aim to provide high precision position information for indoor applications. There are a variety of IPS technologies and techniques, each with their own advantages and disadvantages. The comparison criteria between IPS is accuracy, coverage and cost.

In general, positioning requires ranging measurements and a multilateration computation which uses ranging measurements to solve for position. The range measurements could be RSS (received signal strength), ToA (time of arrival), TDoA (time difference of arrival), or AoA (angle of arrival). Signals for range measurements include RF, light, sound, or magnetic field [1].

Multilateration requires ranging measurements to known locations. The transmitters or receivers at known locations is the infrastructure. Brena [1] defines a passive infrastructure as one that generates signals, and the object to be located receives the signals and computes position. An active infrastructure is the opposite, where the object to be located generates the signals and the infrastructure receives them [1]. In both cases, the multilateration computation is the receiver's job. Positioning algorithms or estimators usually perform the positioning computation.

Each ranging measurement type and method have tradeoffs. This paper focuses on TDoA using audible sound. TDoA is advantageous because it does not require receiver and transmitter synchronization. Instead, infrastructure node synchronization enables time difference measurements.

Using sound is advantageous to RF on an indoor scale since the wave speed is lower by 6 orders of magnitude. This allows for a much lower clock requirement in an audio system versus RF. A slower clock allows for reduced power consumption, computational resources and increased system accuracy. RF indoor positioning systems like WiFi and Bluetooth have not been able to achieve sub-centimeter accuracy [6].

Ultrasonic is superior to audible sound in applications where discreet[1] positioning systems are necessary. However, most ultrasonic transceivers are highly directive, which limits system coverage. Using audible sound allows for use of low directivity speakers and microphones, which allows for increased IPS coverage.

[1] A discreet positioning system refers to a system that operates without obtruding on nearby humans.

Additionally, acoustic-based systems allows for modern devices like smartphones to leverage the system without any additional hardware. Multipath susceptibility is one disadvantage to low directivity speakers and microphones. Section 5.3 discusses methods to combat multipath.

2.2 Pseudo-Noise Sequences

Pseudo-noise (PN) sequences are very important to modern communication techniques. Code Division Multiple Access (CDMA) is a well-known direct sequence spread spectrum (DSSS) technique that uses PN sequences [10]. PN sequences are also popular in range finding applications. A major example is GPS, which uses Gold sequences with RF carriers to obtain ranging measurements [11].

There are three well-known PN sequence families: m-sequence, Gold sequence, and Kasami sequence [12]. M-sequences and Gold sequences are used throughout this paper, so their properties are briefly discussed in Sections 2.2.1 and 2.2.2.

2.2.1 m-Sequences

m-Sequences or maximal length sequences are the easiest PN sequences to generate and are typically generated using linear feedback shift registers (LFSR) [12]. Figure 2.1 shows the Fibonacci configuration for m-Sequence generation. Generation polynomials describe the LFSR. Equation (2.1) shows a general generation polynomial equation for the Fibonacci configuration.

$$f(x) = c_m \cdot x^m + c_{m-1} \cdot x^{m-1} + \cdots + c_0 \tag{2.1}$$

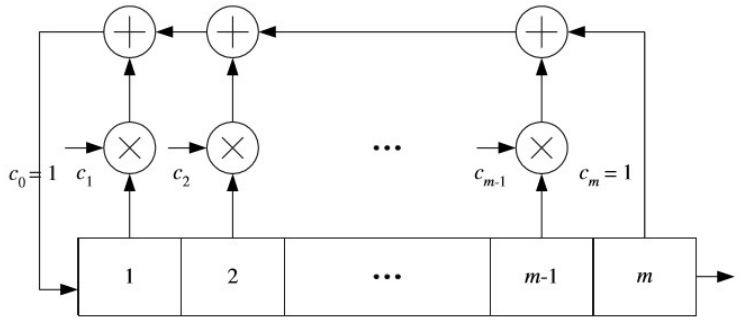

Figure 2.1: m-Sequence Generator using Fibonacci configuration, where "+" is a logical xor and "x" is a logical and [12]

The PN sequence generator produces a periodic sequence, where the PN sequence is the periodic sequence. The length of the sequence is given by $L = 2^m - 1$, where m is the number of shift registers. The generation polynomial $f(x) = x^3 + x + 1$ generates a PN sequence of "1110010" which repeats over time. The most important property of PN sequences is its correlation properties. Auto and cross correlation uses a bipolar transformed sequence where 0's become -1. Figure 2.2 shows the autocorrelation of the PN sequence "1110010". For an ideal PN sequence, there is a maximum of L when perfectly aligned and a minimum of -1 when misaligned. Additionally, good PN sequences have low cross correlation to other signals.

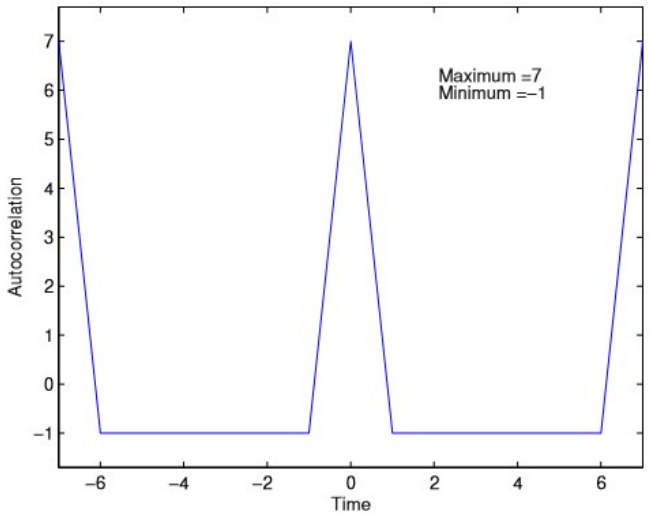

Figure 2.2: Autocorrelation of the sequence 1110010 [12]

The correlation properties are extremely useful for ranging measurements since peaks represent time instants when a signal is received. Identifying peaks, and taking the difference between their times yield TDoA measurements.

Many m-sequences have large cross-correlation [12]. If multiple m-sequences are used, this leads to increased probability of false TDoA measurements. Orthogonal PN sequences are required to identify multiple transmitters. Gold sequences are best for applications with many transmitters.

2.2.2 Gold Sequences

Gold sequences or Gold codes are sometimes preferred over m-sequences because they provide low cross correlation between codes at the expense of a somewhat degraded autocorrelation function. Low cross correlation is more suitable for CDMA since many users are using the same band of frequencies [12]. GPS also uses Gold codes for a maximum of 32 total satellites, with only 24 currently in orbit [11] [13].

Gold sequences are generated by logically adding (xor-ing) two m-sequences [12]. Figure 2.3 shows an example Gold sequence generation block diagram. Figure 2.4 shows the autocorrelation of the sequence generated by Figure 2.3. The correlation of a misaligned Gold sequence is larger relative to an m-sequence. This is the price to pay for low cross correlation between codes.

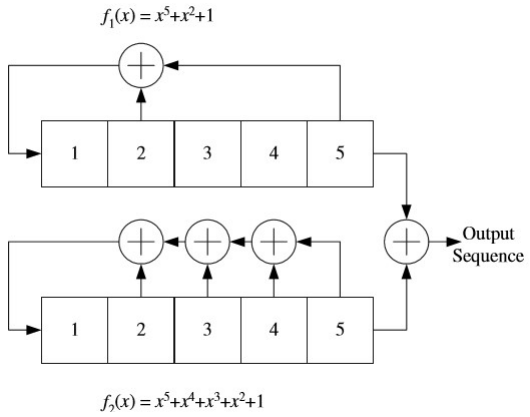

Figure 2.3: Example Gold sequence generation block diagram, where "+" is a logical xor [12]

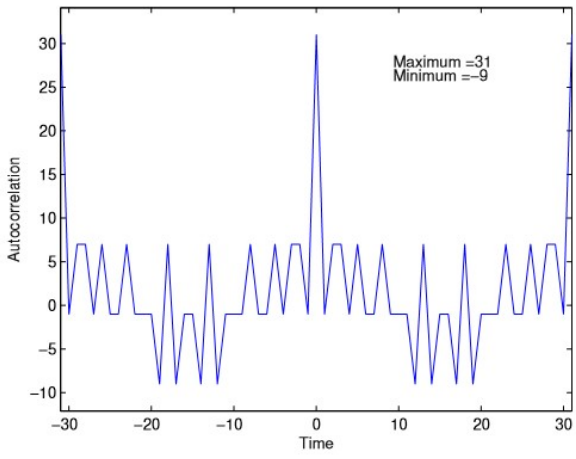

Figure 2.4: Autocorrelation of Gold sequence generation example [12]

2.3 Code Acquisition and Tracking

Code acquisition and tracking loops are paramount in GPS and CDMA receivers. Demodulation of CDMA and GPS signals requires RF carrier and code phase alignment [14] [15]. The purpose of code acquisition and tracking is to lock to the carrier and PN code. Of course, the receiver must know the PN code to demodulate the signal. It is important to understand the implementation of code tracking to identify performance tradeoffs associated with the proposed IPS's design decisions. Figure 2.5 shows the block diagram of a code and carrier tracking loop. The block diagram is reflective of code and carrier tracking for a band-pass system, such as GPS. Note that the proposed IPS operates at baseband and does not require carrier tracking. Additionally, the proposed IPS may or may not require code tracking depending on the sampling frequency of the system. Code tracking is only necessary when there are more than one samples per chip.

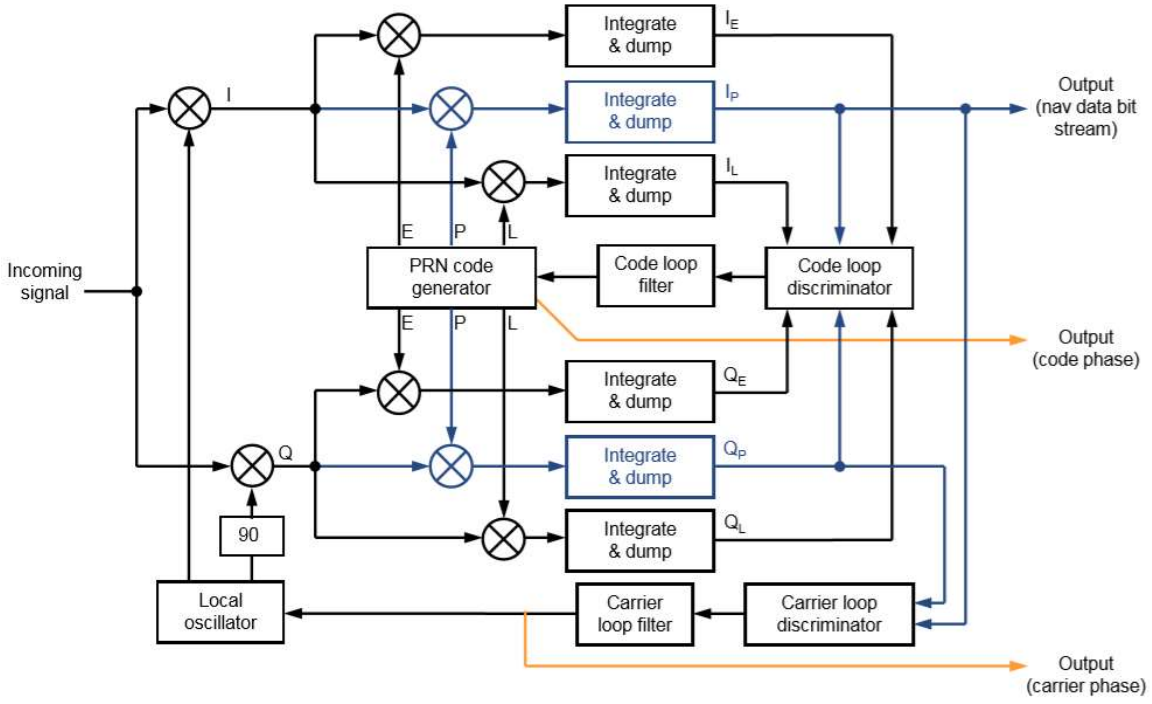

Figure 2.5: Code and carrier tracking loop [14]

The code and carrier tracking loop is a version of a delay locked loop (DLL). Integrate and dump blocks integrate for the PN code symbol period and dump the correlation result. The result is dumped to the next

stage for use and the integrator is cleared to start the accumulation process again. Figure 2.6 shows early, prompt, and late correlations visually. Recall the autocorrelation of PN sequences takes on a triangle shape within one chip of alignment. As seen, early, prompt, and late correlations are samples of the correlated waveform.

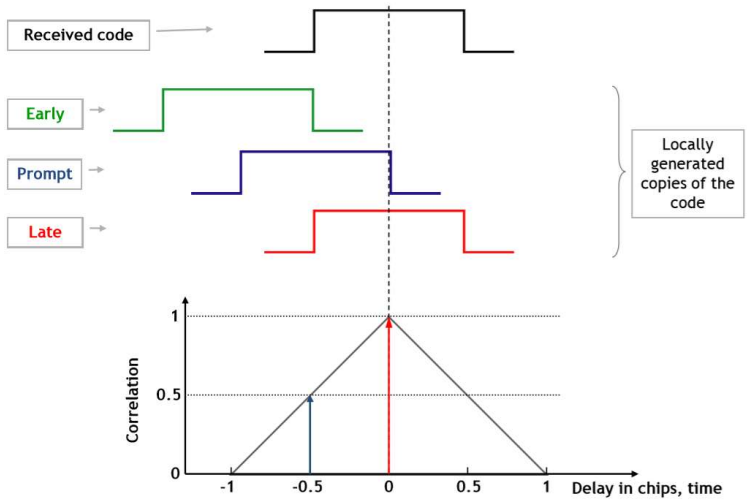

Figure 2.6: Early, prompt, and late correlation for code tracking [14]

The code discriminator uses early, prompt, and late correlations to align to the PN code phase. Similarly, the carrier discriminator uses I and Q prompt correlations to align to the carrier. Carrier tracking is only necessary in band-pass implementations like GPS. The proposed IPS transmits PN codes at baseband, so carrier tracking is not required.

Note the DLL can only find the peak when early, prompt, and late correlations are within one chip of the peak. When early, prompt, and late correlations are outside one chip, their correlations are equal in the ideal case and so the DLL does not know which direction to move to find the peak.

Code acquisition aims to find the code phase within one chip. Code acquisition precedes code tracking in all cases. There are a variety of code acquisition techniques that include serial, parallel and hybrid search approaches [16] [17] [18]. In general, the tradeoff is computation resources and acquisition time.

A GPS receiver tracks one code per visible satellite, and uses differences in code phases from the DLL for TDoA measurements. So, tracking error leads to TDoA measurement error. Multipath is one of the major

issues that leads to phase alignment error in GPS. Some methods to combat multipath include special antennas, special DLL and discriminator designs, and receiver autonomous integrity monitoring (RAIM) to identify erroneous measurements [14]. Special DLL and discriminator designs are most applicable to the proposed IPS [19] [20].

2.4 TDoA Positioning Algorithms

TDoA positioning algorithms, also known as hyperbolic positioning algorithms or estimators, use TDoA measurements and infrastructure node locations to calculate position. The positioning algorithm is an essential step in a positioning system and directly impacts system performance and accuracy.

The solution to the problem is by no means trivial. Equation (2.2) shows the hyperbolic equation for the range difference between the ith node and first node [21]. If there are n nodes in the infrastructure, then there are n-choose-2 nonlinear hyperbolic equations to solve for position. Even with no error in the ranging measurements, a unique solution may not exist. Multiple intersection points in the hyperboles determined from TDoA measurements cause position ambiguity [21].

$$R_{i,1} = R_i - R_1 \tag{2.2}$$

$$= \sqrt{(X_i - x)^2 + (Y_i - y)^2 + (Z_i - z)^2} - \sqrt{(X_1 - x)^2 + (Y_1 - y)^2 + (Z_1 - z)^2}$$

The literature includes a variety of methods to solve the set of nonlinear equations [21] [22] [23] [24] [25] [26] [27] [28]. Iterative methods like the Taylor-Series method are computationally intensive and usually requires a good initial guess. Chan and Ho's method [29] provides a non-iterative closed-form solution to the problem and is an approximation to the maximum likelihood estimator when TDoA measurement error is small [21]. Current literature studying positioning algorithms typically propose new or modified methods to reduce computational intensity or increase accuracy and coverage. Algorithm performance and accuracy is highly dependent on infrastructure node locations. Diez-Gonzalez et. al. recently proposed a method to solve the 3D TDoA problem with 4 sensors. Optimizing infrastructure node location is part of their solution [28].

3 PROPOSED INDOOR POSITIONING SYSTEM

Figure 3.1 shows an overview of the proposed IPS. The system utilizes audible sound waves and TDoA measurements to locate the user. The infrastructure consists of synchronized speakers at anchor locations that transmit orthogonal Gold codes. The user receives the signals with a microphone, acquires TDoA information, and computes the user's location.

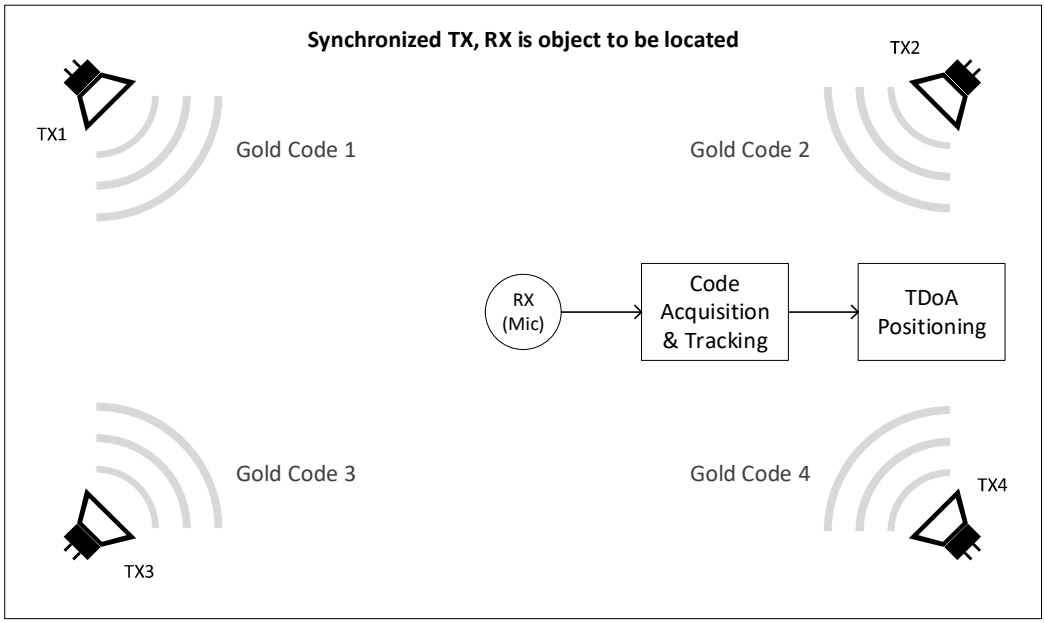

Figure 3.1: Overview of proposed IPS

Using audible sound provides several advantages including inexpensive implementation, larger location service coverage area, and compatibility with existing devices. Off the shelf speakers are largely available and inexpensive. Stereo Logitech S120 AUX inputs speakers are $8.49 on Amazon [30]. Many consumer devices like smartphones and computers already have both microphones and speakers. Additionally, working with the speed of sound compared to speed of light allows for much slower sampling frequency, saving analog and digital hardware expenses. An advantage to using audible sound over ultrasonic is the availability of low directive speakers and microphones. Low directivity eliminates receiver and transmitter orientation constraints and increases location service coverage. Finally, using audible sound allows the possibility of old devices to leverage the system. For example, smart phones and laptops already meet the hardware requirement of a speaker or microphone and processor. To demo this, some of the experiments discussed in Section 4 and Section 5 were conducted with a laptop as the receiver.

3.1 Gold Codes

The Gold codes used for ranging determine the speed, range and noise immunity of the system. A longer Gold code results in a slower system, but extends the range and increases noise immunity. The Gold code generation polynomials match GPS [13]. The system's bandwidth constraint defines the chipping and symbol period used to transmit the codes. The frequency response of the speakers and microphones defines the system's bandwidth constraint. The best case assumes a 20 Hz – 20 kHz bandwidth constraint. Modeling the Gold code as a square wave with a frequency equal to the chipping rate gives the worst case Gold code bandwidth requirement. Figure 3.2 shows the worst case model. The maximum chipping frequency is double the bandwidth constraint of 20 kHz. This ensures the fundamental frequency of the square wave model is within the bandwidth constraint. Multiplying the symbol period by the speed of sound yields range without ambiguity. Objects located outside the symbol period radius requires a priori information to properly scale the time of flight measurements for accurate positioning. Table 3.1 shows the calculated values.

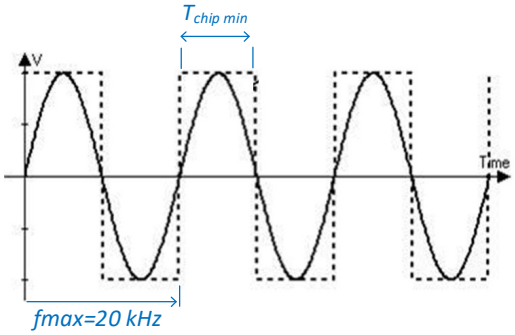

Figure 3.2: Worst case Gold code bandwidth requirement time domain model

Table 3.1: Proposed IPS PN characteristics summary

PN Type	Gold
$f_1(x)$	$x^{10} + x^3 + 1$
$f_2(x)$	$x^{10} + x^9 + x^6 + x^3 + x^2 + 1$
# chips	1023
T_{chip}	0.025 ms
T_{symbol}	25.575 ms
Bit rate	39.1 bps
Range w/o ambiguity	8.77m (28.77 ft)

3.2 Receiver Requirements

The receiver is the user of the positioning service and requires a microphone and processor to calculate position. Ideally, the microphone is omnidirectional and has flat frequency response up to 20 kHz. Nyquist theorem requires a sampling frequency of at least 40 kHz. A faster sampling frequency improves overall system accuracy. The processor should be fast enough to perform code acquisition and tracking. Serial acquisition approaches can lower the computation resource necessity in situations where computation resources are scarce. A serial acquisition approach is slower than parallel acquisition, but requires less resources [16] [17] [18].

Inexpensive hardware requirements for receivers is a huge advantage for audible sound positioning systems. Microphones being common on consumer devices leaves opportunity for existing devices to leverage an audible sound positioning system via software development.

3.3 Infrastructure Requirements

The transmitters are the infrastructure of the positioning service. The transmitters are synchronized and placed at known locations so the receiver can calculate its position based on TDoA measurements. Note that each transmitter plays a unique Gold code. Orthogonality is desirable for low cross correlation between codes, regardless of time shift. Recall that cross correlation between codes is not zero, even in the ideal case. A single correction filter on the receiving end requires identical transmitting speakers. Section 4.4 discusses correction filters. Additionally, each transmitter should only have a single speaker; no tweeter and woofer pairs or stereo used as mono pairs. Section 5.2.1 discusses this requirement. Full range 20-20 kHz speakers maximize correlation performance. Inexpensive, low quality off the shelf speakers and a microcontroller to generate the Gold codes are sufficient hardware to implement the infrastructure. Again, a major advantage of an audible sound positioning system is the inexpensive infrastructure requirement. Section 5.5.1 simulates positioning performance, but note that increasing the number of transmitting nodes generally increases overall system positioning.

3.4 Variations

In the case where it is too computationally intensive for a device to be a receiver which requires code acquisition and tracking and TDoA positioning, one variation is a flipped system where the user transmits and the anchors receive. In the flipped system, the intensive computation moves to the infrastructure and requires additional channel to communicate to the user its location. Additionally, with multiple users the flipped system is more prone to the near-far problem. Section 6.1.1 discusses the near-far problem. The flipped system is not directly studied in this paper, however both systems share the same fundamentals. Other variations include using longer or shorter PN sequences to improve system speed or noise immunity. PN variations are also not studied in this paper.

3.5 Limitations

Using audible sound also comes with the obvious and major disadvantage that humans would have to hear the pseudo-noise signals. This makes the system impractical for discreet[2] positioning applications. A low transmitter duty cycle could decrease the annoyance to humans. Similarly, the flipped system could also be less annoying as the user would be triggering the audible noise. The disadvantage could be irrelevant in applications where a discreet positioning service is not required. Some robotics, mapping or tracking applications may not require a discreet IPS. For example, a warehouse that uses moving autonomous robots. Nakashima et al. and Suzuki and Ogiso studied an acoustic IPS that digitally watermarks audio with PN sequences [9] [7]. In theory, watermarked music could provide indoor location services without disturbing humans. This modification expands the practical applications of an acoustic IPS.

[2] A discreet positioning system refers to a system that operates without obtruding on nearby humans.

4 PRELIMINARY TESTING

This section details all preliminary testing prior to testing the proposed IPS. Preliminary tests include characterizing the channel, experimenting with channel correction techniques, and adjusting receiver and transmitter parameters. The purpose of the preliminary testing is to determine if an IPS using acoustic PN based TDoA is possible. Section 5 studies a 4 node infrastructure implementation.

4.1 Custom Receiver Board

Development of a custom receiver board provides flexibility during testing, and allows the option to develop a real time IPS with an FPGA dev board. This alleviates the "black box" of DSP employed by laptop or smart phone microphones and ensures accurate test results. "Black box" DSP includes optimization for voice applications and noise and echo reduction which is not suitable for testing the proposed IPS. Additionally, laptop and smart phone microphones typically only have set sampling frequencies of 44.1 kHz and 48 kHz.

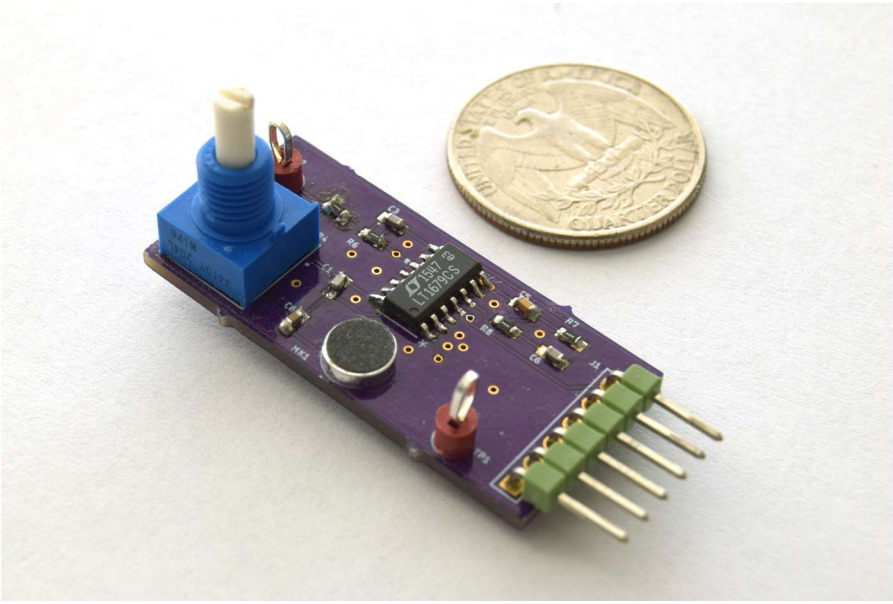

Figure 4.1: Custom receiver board with CMC-6015-42P microphone and MAX1285 ADC

4.1.1 Requirements

Functionally, the board is an analog front end to a digital receiver. Figure 4.2 depicts the high level block diagram of the analog front end. Table 4.1 outlines the requirements for each block in the design.

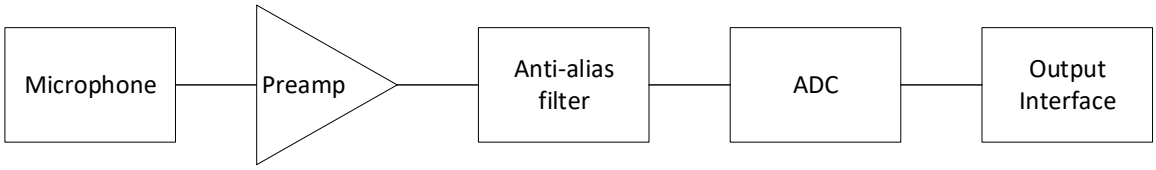

Figure 4.2: High level block diagram of the custom receiver board

Table 4.1: Custom receiver board design requirements

Block	Requirement	Justification
Microphone	Omnidirectional	Proposed IPS requires low directivity microphone
	Analog	Provide ability to adjust analog gain, probe waveform with a scope
Preamp	Low noise	Maximize receiver performance
	Adjustable analog gain	Provides testing flexibility, not expensive to include
Anti-alias filter	4^{th} order Butterworth, 20 kHz cutoff	Magnitude distortion in the passband is undesired
	Low noise	Maximize receiver performance
ADC	Internal reference	Eliminate design need for stable reference voltage
	ADC with variable sampling frequency up to 400 kHz	Provide testing flexibility
Output Interface	PMOD compatible	Ability to use Rx board with FPGA or MCU dev board for real time system development

4.1.2 Component Selection

The design calls for a microphone, op amps, and an ADC to be selected.

Table 4.2 shows the components selected to meet the design requirements outlined in Table 4.1.

Table 4.2: Custom receiver board component selection

Component required	Selected Component	Specs
Microphone	CMC-6015-42P	Omnidirectional, -42dB sensitivity, Ø6.0 x 1.5 mm
Op amp	LT1677	Rail-to-rail, 7.2MHz GBW, low noise
ADC	MAX1285	12 bit, 400ksps, 2.5V internal reference

4.1.3 Analog Front End Design

Figure 4.3 shows the schematic of the analog front end. This section details the design associated with each block of the analog front end.

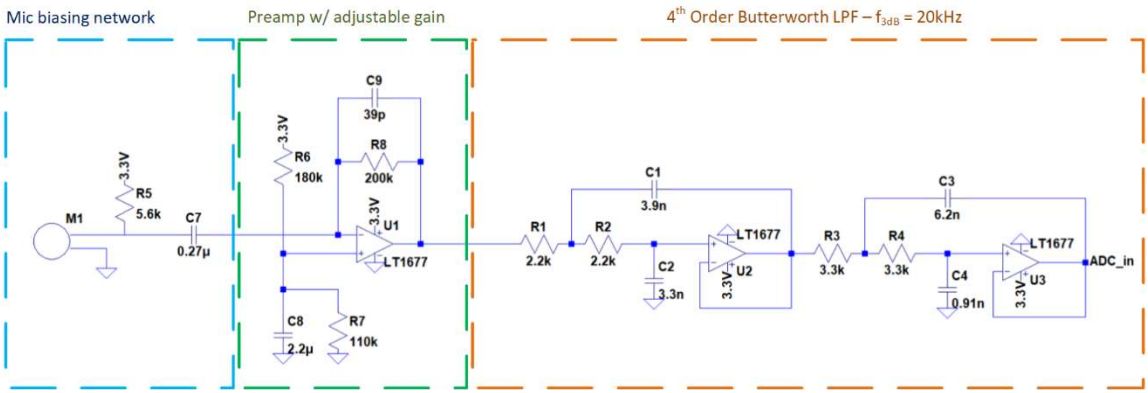

Figure 4.3: Custom receiver schematic

4.1.3.1 Microphone Biasing

Figure 4.4 shows the CMC-6015-42P measurement circuit. RL determines the voltage terminal 1 sits at. The terminal should sit at half the supply voltage to maximize voltage swing. Proper RL sizing requires microphone IV characteristic measurements. Figure 4.5 shows the measured IV characteristics of the two CMC-6015-42P microphones.

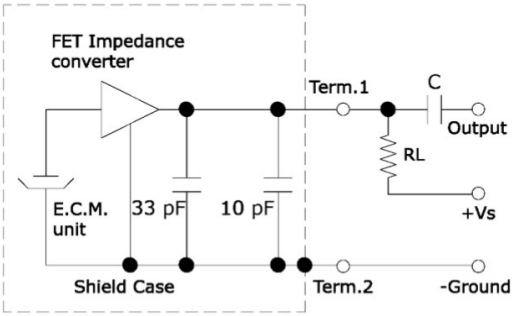

Figure 4.4: CMC-6015-42P measurement circuit [31]

Applying KVL to the measurement circuit yields Equation (4.1). Solving Equation (4.1) for RL yields Equation (4.3). To maximize voltage swing, V_{mic} should sit at the midpoint between the microphone on voltage and supply voltage. Equation (4.2) describes V_{mic}. A standard value bias resistor of 5.6k is a compromise between the two CMC-6015-42P microphone IV characteristics.

The PMOD interface requirement constraints the supply voltage to 3.3V. Figure 4.5 shows the CMC-6015-42P has a Von of 0.5V. Calculating and rounding RL to a standard value yields of 5.6kΩ.

$$V_s - I_{mic} * RL - V_{mic} = 0\ V \tag{4.1}$$

$$V_{mic} = \frac{V_s - V_{on}}{2} + V_{on} = \frac{3.3V - 0.5V}{2} + 0.5V = 1.9V \tag{4.2}$$

$$RL = \frac{V_s - V_{mic}}{I_{mic}} = \frac{3.3V - 1.9V}{236.4\mu A} = 5.922k\Omega \rightarrow 5.6k\Omega \tag{4.3}$$

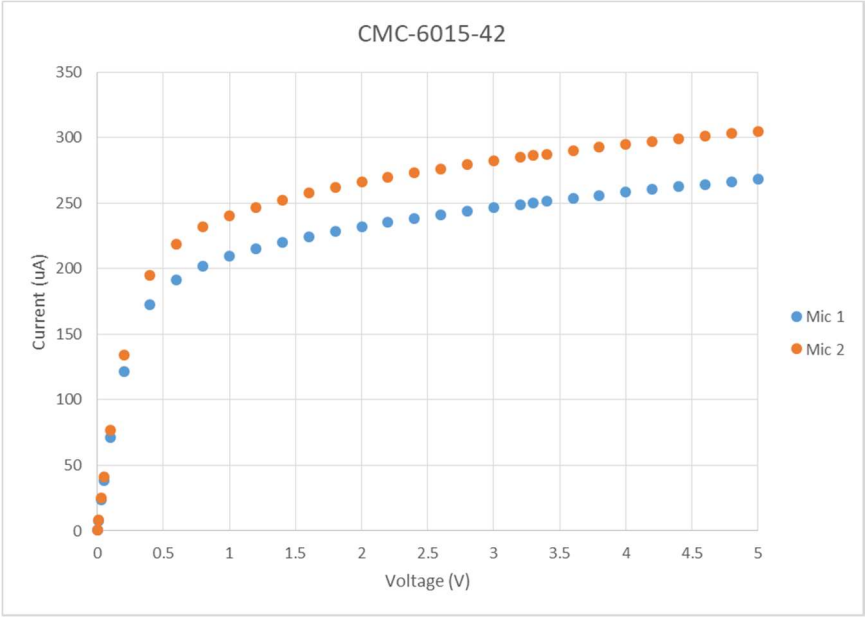

Figure 4.5: CMC-6015-42P measured IV characteristics

4.1.3.2 Preamp

The preamp design uses a Texas Instruments single-supply, electret microphone pre-amplifier reference design, shown in Figure 4.6. Note that the AC coupling network in the reference design (R5, C5 and R6) was not used since the a 4th order Butterworth follows the preamp stage.

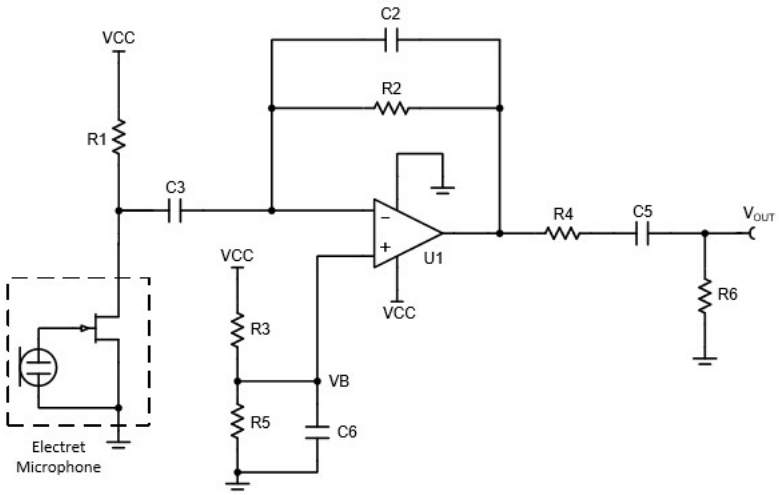

Figure 4.6: Texas Instruments single-supply, electret microphone pre-amplifier reference design [32]

The following Texas Instruments equations are used to select C3 and C6:

$$C_3 = \frac{1}{2\pi R_1 f_c} = \frac{1}{2\pi * 5.6k\Omega * 100Hz} = 0.284\mu F \rightarrow 0.27\mu F \tag{4.4}$$

$$C_6 = \frac{1}{2\pi (R_3 \parallel R_5) f_c} = \frac{1}{2\pi (R_3 \parallel R_5) f_c} = \mu F \rightarrow 2.2\mu F \tag{4.5}$$

The reference voltage of the ADC is 2.5V, so a 1.25V preamp bias voltage maximizes voltage swing. An exhaustive search script finds standard R3 and R5 to achieve bias voltage of 1.25V from a 3.3V supply with minimum squared error. R2 is a 200kΩ potentiometer. Section 4.1.4 sizes C2 through simulation.

4.1.3.3 4th Order Butterworth LPF

Figure 4.7 shows two cascaded Sallen-Key low pass architectures implementing a 4th order Butterworth LPF. Equation (4.6) gives the second order transfer function of a single Sallen-Key low pass stage [33]. Setting R1=R2 simplifies Equation (4.6) to Equation (4.7). The normalized pole and zeros of a 4th order Butterworth are given in Table 4.3 by Maxim [33].

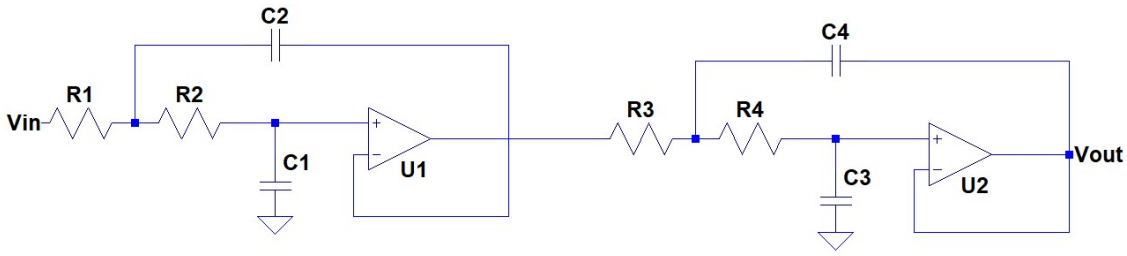

Figure 4.7: 4th order Butterworth Sallen-Key LPF architecture

$$\frac{V_o}{V_i} = \frac{1}{s^2(R1R2C1C2) + sC1(R1 + R2) + 1} \tag{4.6}$$

$$\frac{V_o}{V_i} = \frac{1}{s^2(R1^2C1C2) + s(2R1C1) + 1} \tag{4.7}$$

Table 4.3: 4th order normalized Butterworth pole locations [33]

Poles (a ± jb)	Quadratic Expression
-0.9239 ± 0.3827	$s^2 + 1.8478s + 1$
-0.3827 ± 0.9239	$s^2 + 0.7654s + 1$

Selecting a 20 kHz cutoff frequency and setting R1=R2, R3=R4 the design equations become:

$$C1R1 = \frac{1.8478}{2 * 2\pi * 20kHz} \quad (4.8)$$

$$C2R1 = \frac{2}{1.8478 * 2\pi * 20kHz} \quad (4.9)$$

$$C3R3 = \frac{0.7654}{2 * 2\pi * 20kHz} \quad (4.10)$$

$$C4R3 = \frac{2}{0.7654 * 2\pi * 20kHz} \quad (4.11)$$

An exhaustive search script finds standard resistor and capacitor values that minimize squared error. Table 4.4 shows error introduced to the design equations, by using standard value components. Figure 4.8 shows the standard value 20 kHz cutoff, 4th order Butterworth circuit. Figure 4.9 shows the simulated AC response to the circuit.

Table 4.4: 4th order Butterworth ideal and standard value RC product

Product	Ideal (µs)	Standard Value (µs)	% Error
$C1R1$	7.352	7.260	1.25%
$C2R1$	8.613	8.580	0.39%
$C3R3$	3.045	3.003	1.39%
$C4R3$	20.794	20.460	1.60%

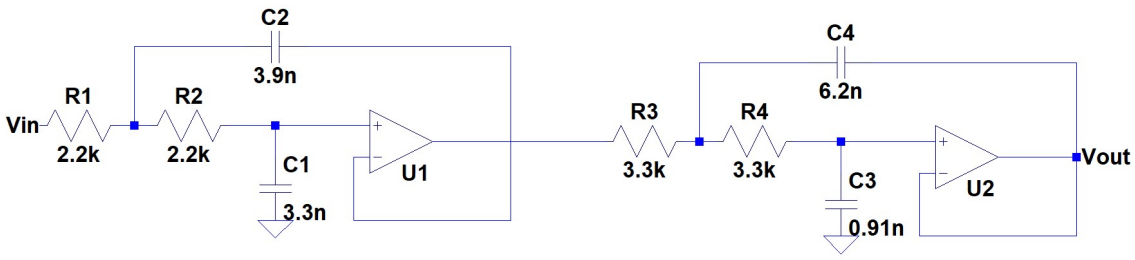

Figure 4.8: Standard value 20 kHz cutoff, 4th order Butterworth circuit

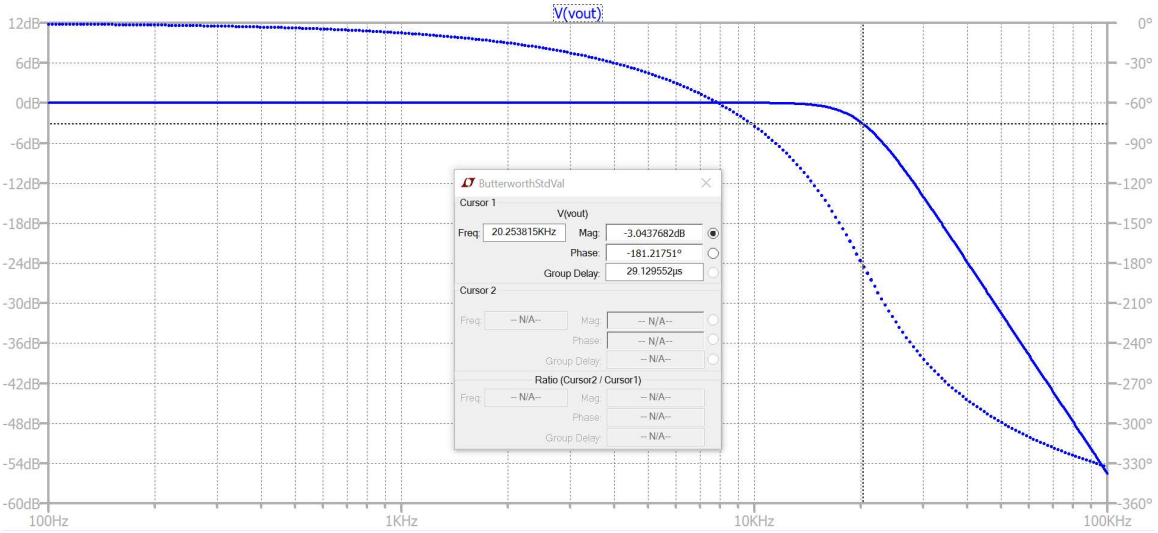

Figure 4.9: 4th order Butterworth frequency response LTSpice simulation

4.1.4 Analog Front End Simulation

Figure 4.11 shows the noise analysis simulation of the complete front and confirms proper resistor sizing. R5 as the dominant noise source is desirable since the microphone IV characteristics strictly determines R5 with no possible variation. Figure 4.12 shows the analog front end response to a 0.05ms pulse, simulating the fastest pulse the front end could receive. The feedback capacitor, C7, compensates for potential instability introduced by the op amp's parasitic capacitance at the inverting input. C7 is selected by visual inspection to minimize ringing, while not affecting the transfer function within the bandwidth.

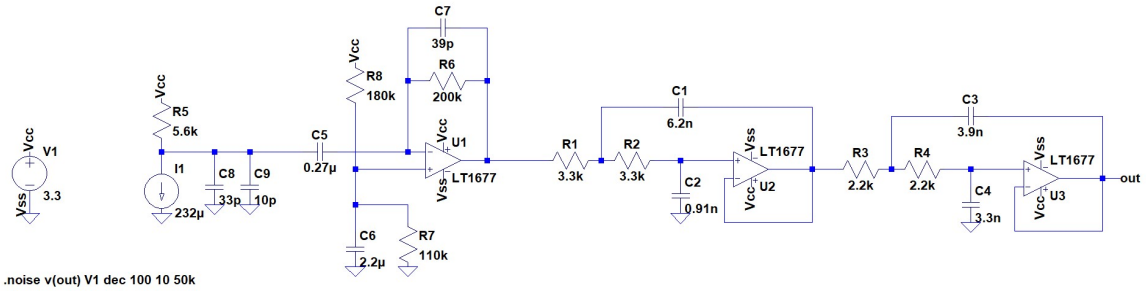

Figure 4.10: Analog front end LTSpice simulation schematic

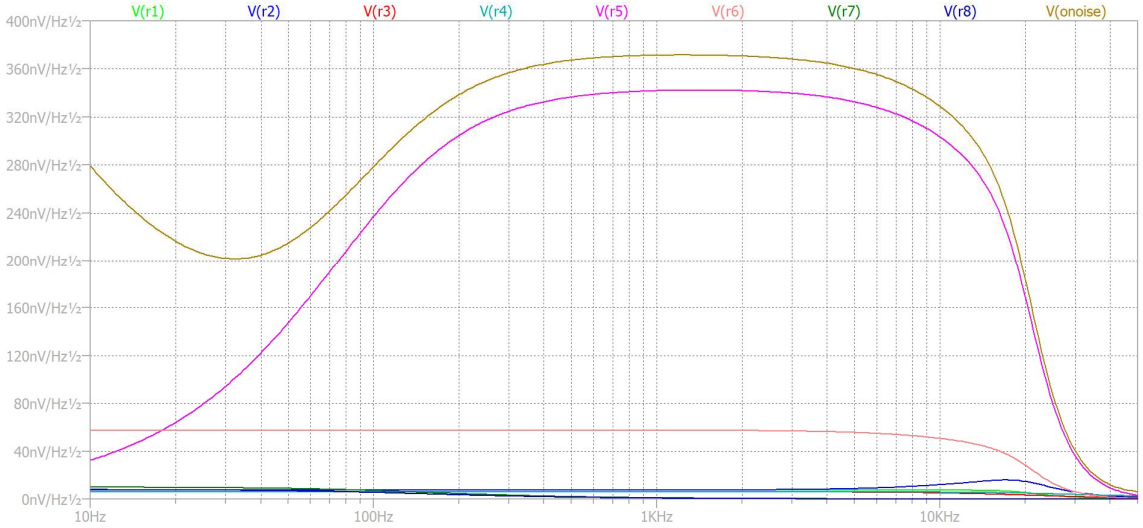

Figure 4.11: Analog front end LTSpice noise analysis

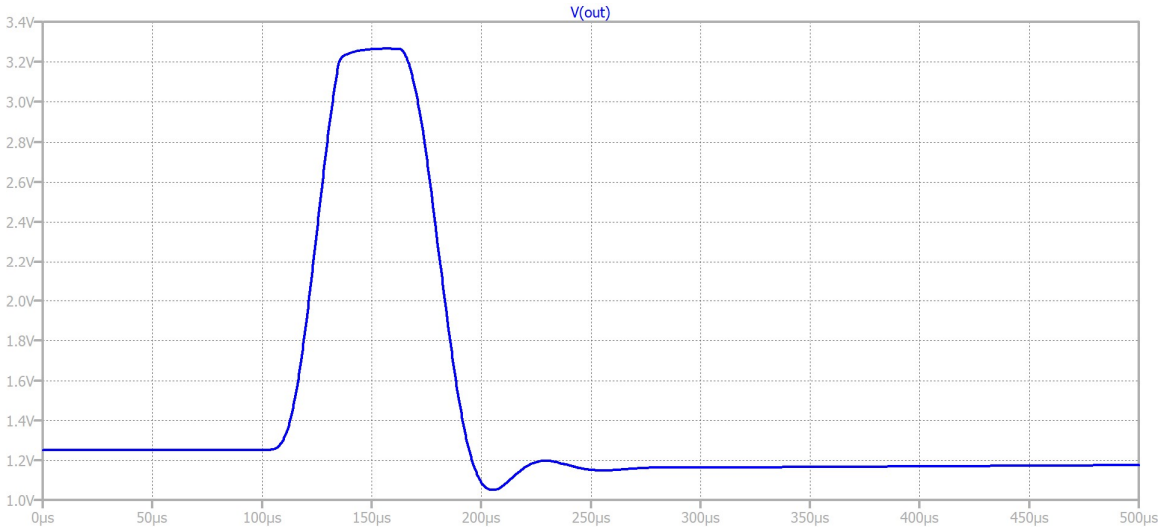

Figure 4.12: Analog front end 0.05ms transient pulse response LTSpice simulation

4.2 Fabrication

A 2 layer board was designed using Eagle and the board was fabricated using Oshpark. Figure 4.13 shows the full custom receiver board schematic. Figure 4.14 and Figure 4.15 show the top and bottom layers of the board respectively. Test points after the preamplifier and 4th order Sallen-Key LPF allow for easy probing.

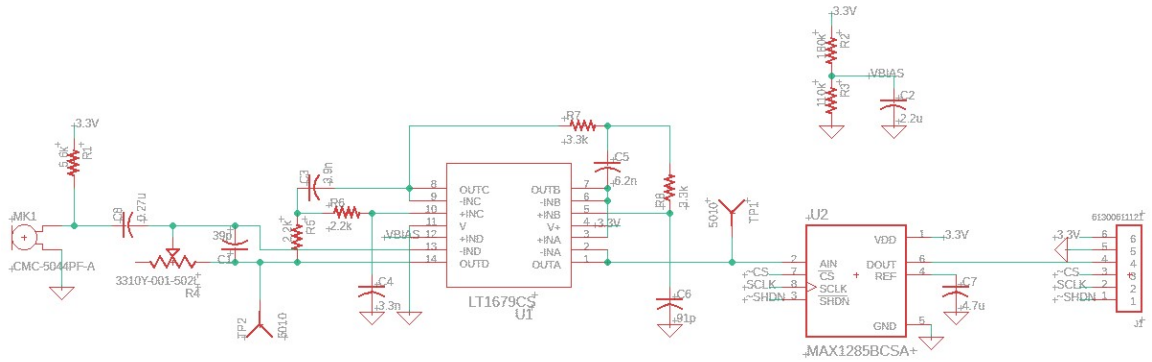

Figure 4.13: Custom receiver Eagle schematic

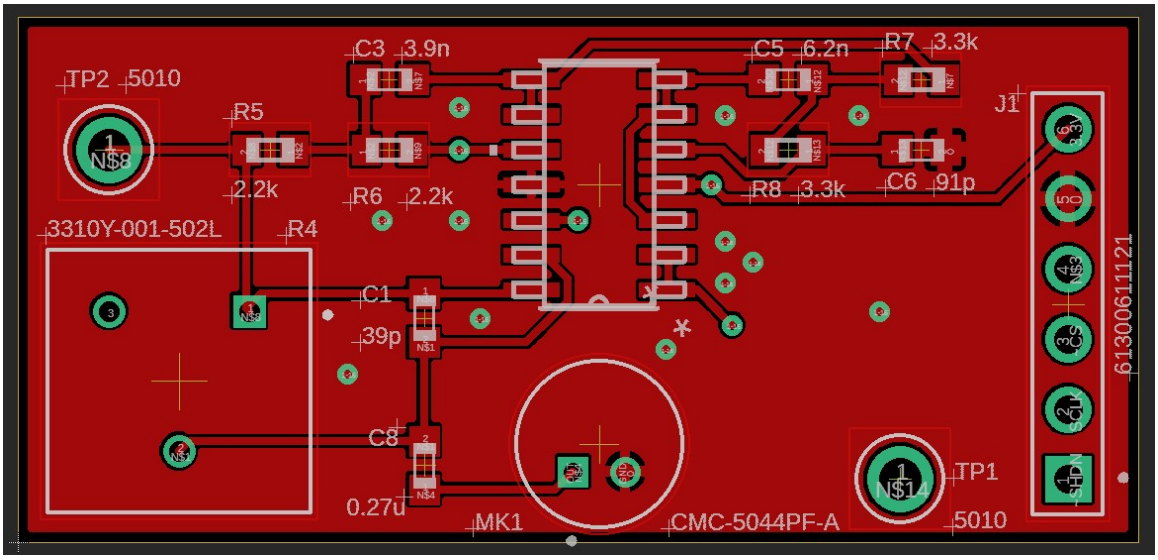

Figure 4.14: Custom receiver Eagle top board layout

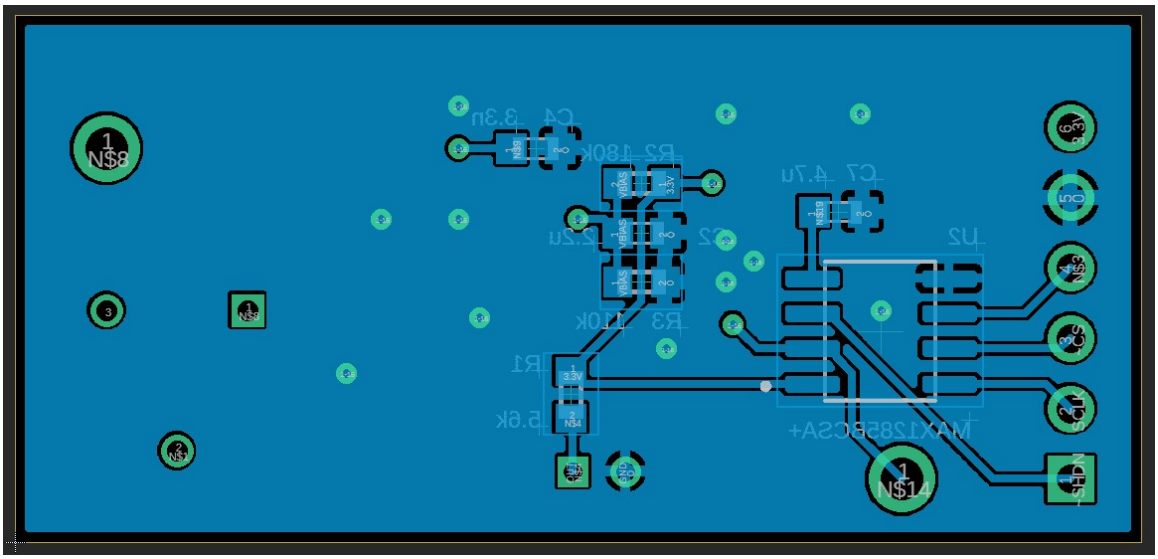

Figure 4.15: Custom receiver Eagle bottom board layout

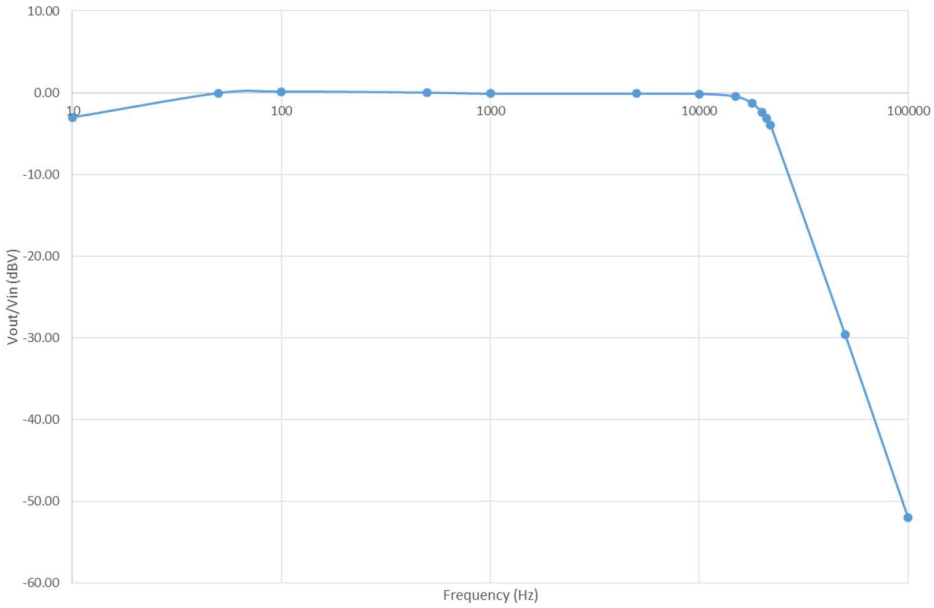

Figure 4.16: 4th order Butterworth measured frequency response

4.3 System Impulse Response

Figure 4.17 shows the LTI model of the proposed IPS. Each stage distorts the original PN signal and degrades code acquisition and tracking performance. Applying a correction filter before code acquisition and tracking can improve performance. Correction filter design requires a system impulse response measurement.

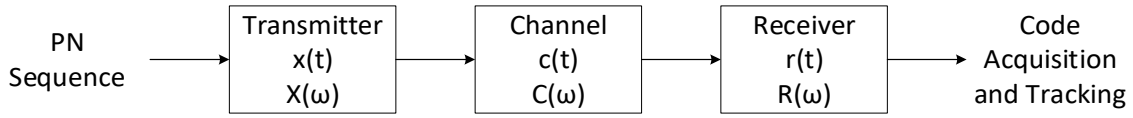

Figure 4.17: Proposed IPS LTI model

4.3.1 Measurement Method

A maximum-length-sequence (MLS) signal can be used to measure the impulse response of a room [34]. Let h(t) represent the system impulse response, depicted in Equation (4.12) where * represents convolution. Let p(t) represent an ideal PN sequence input to the LTI system and y(t) represent the received waveform used in code acquisition and tracking. So, y(t) is p(t) convolved with h(t) shown in Equation (4.13). Correlating p(t) with y(t) yields Equation (4.14). Since p(t) is a MLS, the autocorrelation of p(t) is approximately equal to a Dirac delta function. Equation (4.14) becomes Equation (4.15). Therefore, correlating the ideal MLS with the received, filtered MLS yields the system impulse response, h(t).

$$h(t) = x(t) * c(t) * r(t) \tag{4.12}$$

$$y(t) = p(t) * h(t) \tag{4.13}$$

$$p(-t) * p(t) * h(t) = p(-t) * y(t) \tag{4.14}$$

$$h(t) = \delta(t) * h(t) \cong p(-t) * y(t) \tag{4.15}$$

4.3.2 Measurements

The system impulse response is measured by transmitting a single, nonrepeating MLS. The MLS uses a chipping rate of 40 kHz, as detailed in section 3.1. The transmitter is the Samsung Galaxy Prime smart phone and the receiver is the custom receiver board. Figure 4.18 shows the received MLS waveform on TP1 of the custom receiver board. The received waveform does not resemble a square wave due to significant filtering from the system impulse response.

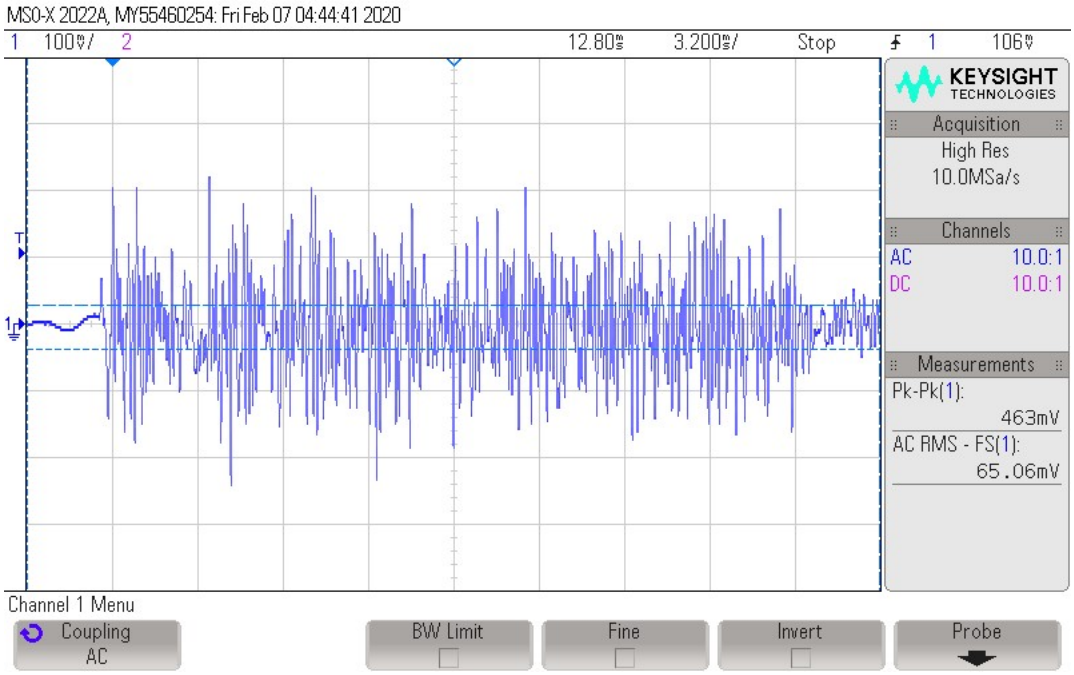

Figure 4.18: Received PN waveform, probed at TP1 on custom receiver board

Five measurement trials are used to observe the system impulse response variation from trial to trial. Table 4.5 shows the received waveform statistics of the trials. Figure 4.19 shows the normalized correlation of the trials with the ideal MLS and their average. There is minimal variation in the measured impulse response between trials temporally close to the peak. The impulse response lasts about 0.8 ms. Note the ringing after 0.8 ms is due to an MLS autocorrelation without wrapping. Figure 4.20 shows there is noise 1 symbol period on each side of the peak. Another interesting artifact in Figure 4.20 is reverb due to the room, caused by delayed and decayed versions of the transmitted MLS arriving at the microphone. The impulse response continues ringing even 1 symbol period after the peak.

Table 4.5: Received PN waveform statistics

Trial	Vrms (mV)	Vpkpk (mV)
1	65.1	463
2	71.1	454
3	66.4	486
4	73.7	542
5	86.7	646

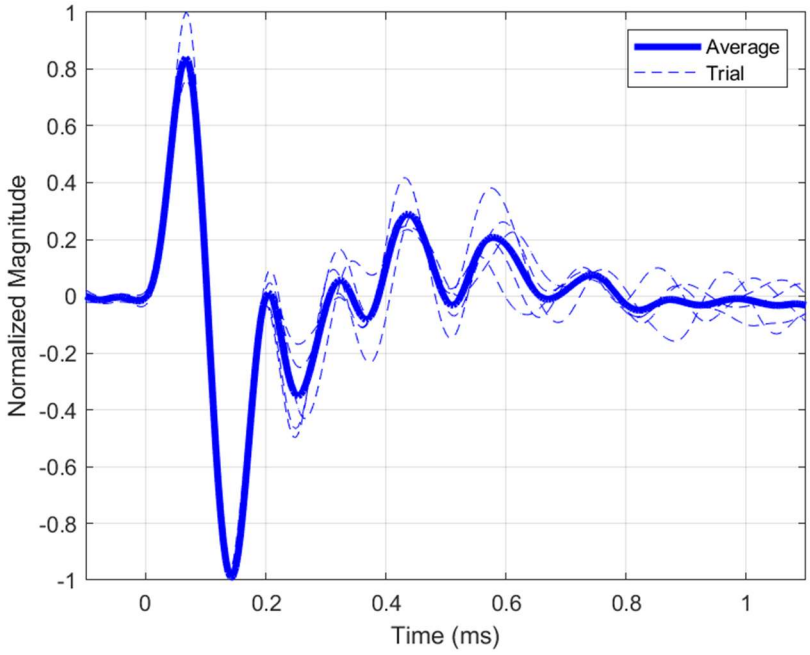

Figure 4.19: Galaxy Prime, custom receiver board measured system impulse response

Recall that code acquisition aims to find the phase within one chipping period and tracking uses early, prompt, and late samples of the correlated waveform to find the peak. The odd symmetry of the impulse response poses an issue to code acquisition and symbol decoding. The negative and positive peak are close in magnitude and very close to each other in time, making symbol decoding difficult. Section 4.4 presents correction method to improve code acquisition and symbol decoding.

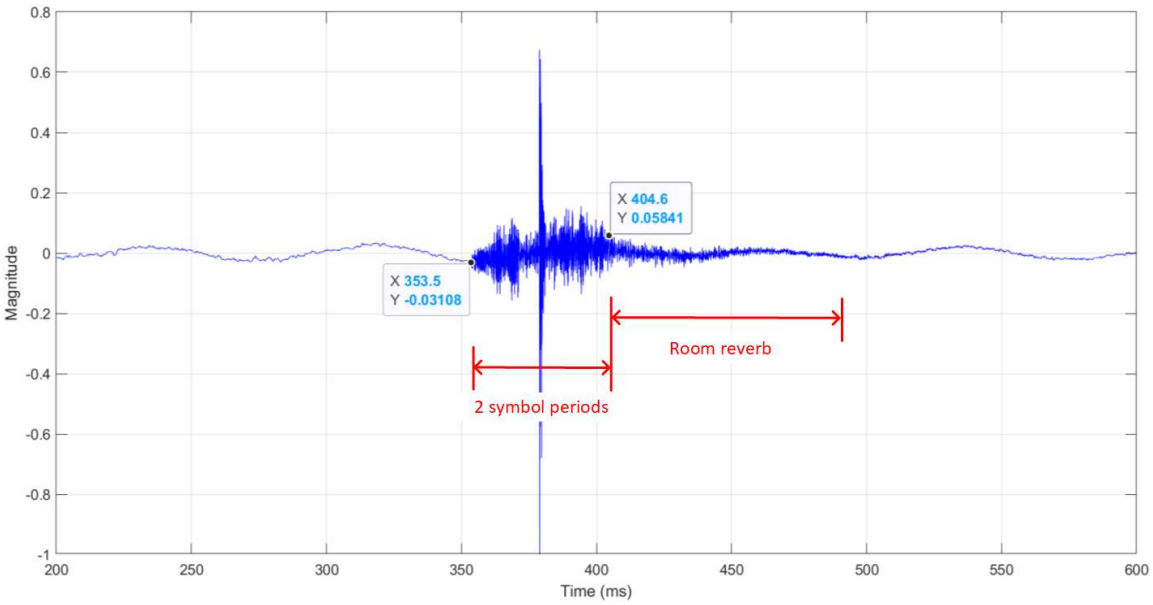

Figure 4.20: System impulse response zoomed out

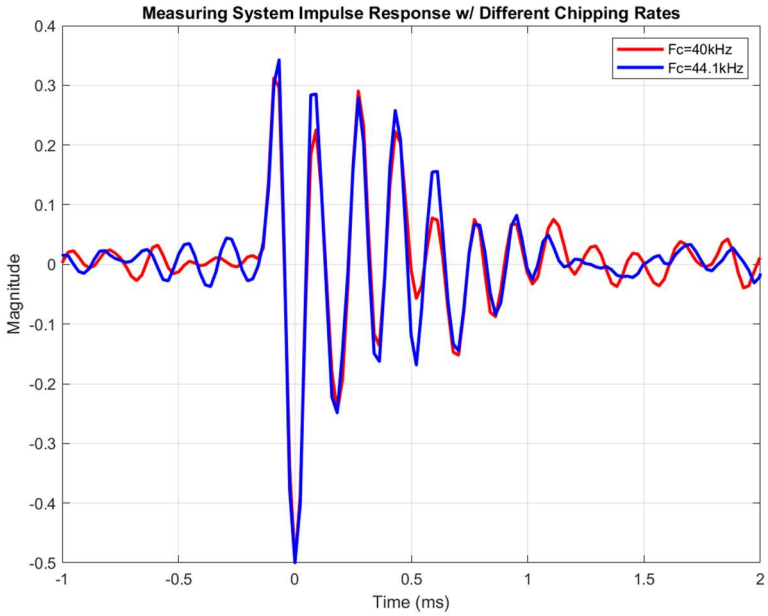

Figure 4.21: Samsung Galaxy Prime, Snowball Ice system impulse response when receiving at 0 degrees, with respect to its cardioid radiation pattern [35]

Figure 4.21 shows the measured impulse response between the Samsung Galaxy Prime and Snowball Ice microphone using two different chipping rates. The Snowball Ice microphone has a sampling rate of 44.1 kHz

[35]. Note the negligible difference between the two measured impulse responses. This confirms that upsampling on the processing end has minimal impact on the response. The impulse response is about 1.2 ms. Figure 4.21 also shows significant ringing compared to Figure 4.19. Significant ringing reduces code acquisition performance, as it may not lock to the global peak, thereby introducing measurement error. Section 4.4 discusses methods to correct the impulse response.

4.4 System Impulse Response Correction

Odd symmetric impulse responses with lots of ringing, as seen in Section 4.3.2 yields poor code acquisition and symbol decoding performance. Correcting the system impulse response improves code acquisition and symbol decoding performance. This section details three methods to correct the channel impulse response.

4.4.1 Adaptive Filter

One equalization technique for FIR systems uses adaptive filters to design a correction filter [36] [37] [38]. Figure 4.22 shows the block diagram for the technique. The adaptive filter weights are updated via the LMS (Least Mean Square) Algorithm to minimize distortion caused by the plant. Figure 4.23 shows a summary of the LMS Algorithm, where W is the adaptive filter weights and X is the system input. The adaptive filter length is set equal to the length of the measured impulse response. The delay is set equal to the length of the plant and adaptive filter combined, or twice the length of the plant or adaptive filter since they are equal. The step size, μ, is set to 0.009 and run for 30000 iterations. Figure 4.25 shows the corrected impulse response.

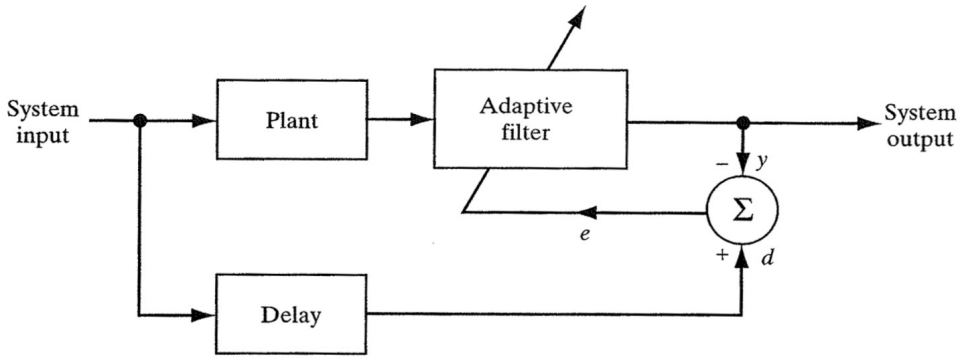

Figure 4.22: Adaptive filter architecture for channel equalization [37]

Step 1: initialization

Step 2: for each iteration *n*

$$X(n) = [x(n), x(n-1), \ldots, x(n-M)]^T$$
$$W(n) = [w_0(n), w_1(n), \ldots, w_M(n)]^T$$
$$y(n) = W^T(n)X(n)$$
$$e(n) = d(n) - y(n)$$
$$W(n+1) = W(n) + 2\mu e(n)X(n)$$

Repeat step 2 if necessary

Figure 4.23: Summary of LMS algorithm corresponding to Figure 4.22 [37]

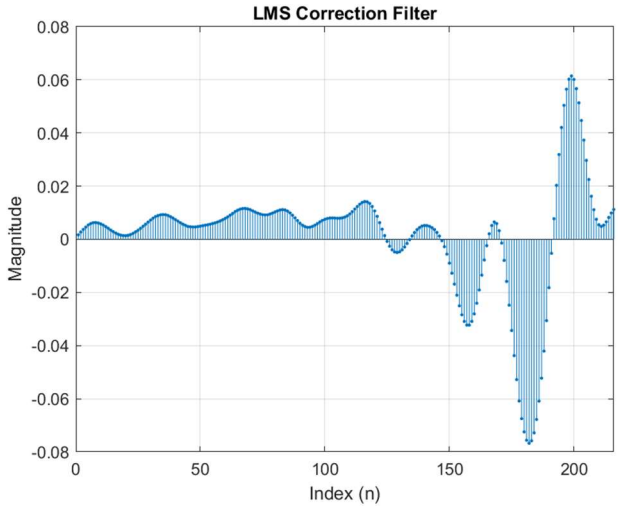

Figure 4.24: LMS correction filter, Fs = 240 kHz

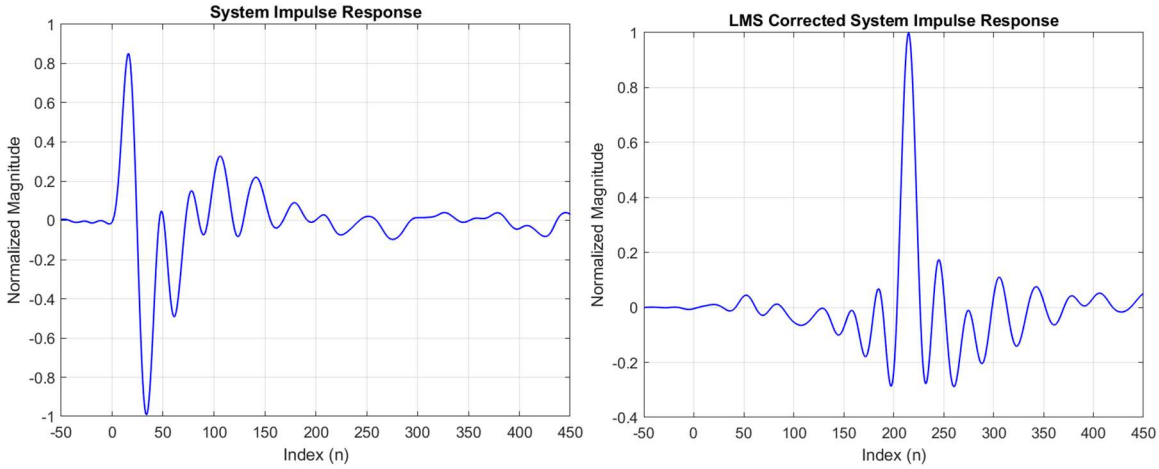

Figure 4.25: LMS corrected system impulse response, Fs = 240 kHz

There is significant improvement in the post-correction system impulse response. The impulse response is now even symmetric and ringing is within 30%. Interestingly, Figure 4.24 shows the LMS correction filter converged to a filter that resembles a time revered system impulse response before correction. This caused some research into time reversal.

4.4.2 Time Reversal

Time reversal (TR) filtering is an inverse filter that only compensates for phase distortions. TR dates to 1957 as an automatic technique to correct for delay-distortion of transmission networks [39]. There has also been research into using TR with wireless communications and wave focusing applications [39] [40] [41].

The phase correction filter works by creating a causal, time reversed version of the system impulse response. Assume signal, x, is input to a system with impulse response h. Equation (4.16) gives the time domain TR phase corrected output, y. The Fourier Transform of Equation (4.16) yields Equation (4.17) [10]. As seen, the TR filter successfully corrects the phase response introduced by the system.

$$y(t) = x(t) * h(t) * h(T - t) \tag{4.16}$$

$$Y(\omega) = X(\omega) \cdot |H(\omega)|^2 \cdot e^{-j\omega T} \tag{4.17}$$

Figure 4.26 shows the TR correction filter derived from Galaxy Prime, custom receiver board system impulse response.

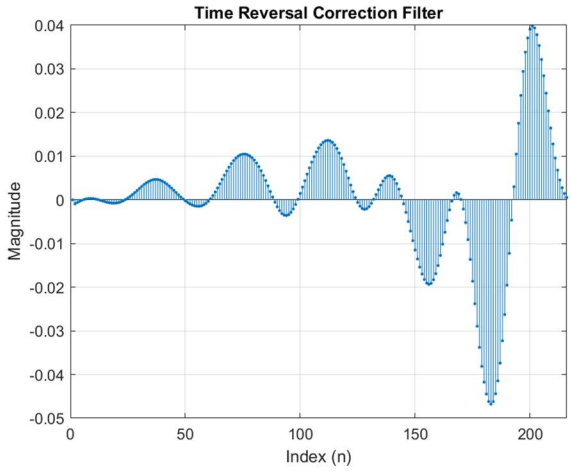

Figure 4.26: Time reversal system impulse response correction filter, Fs = 240 kHz

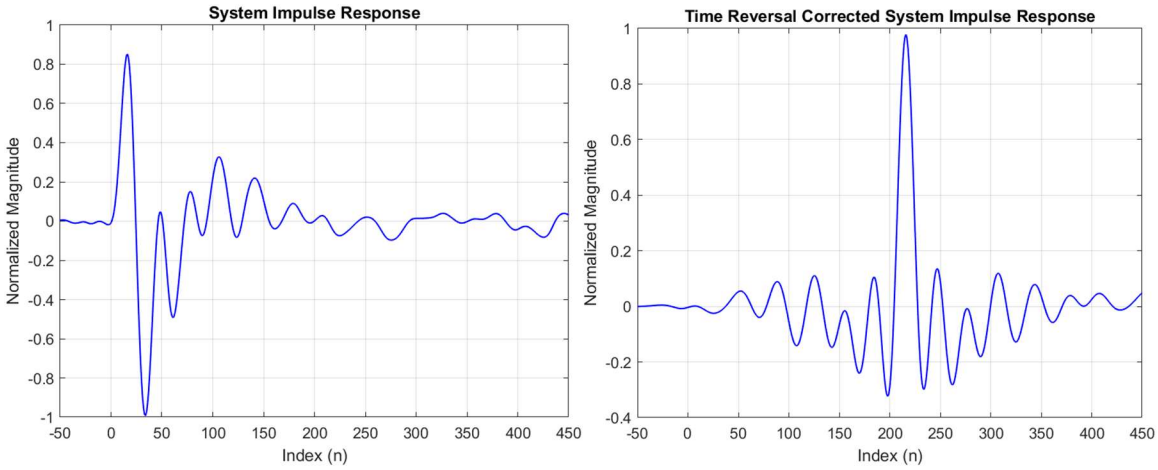

Figure 4.27: Samsung Galaxy Prime, custom Rx board time reversal corrected system impulse response, Fs = 240 kHz

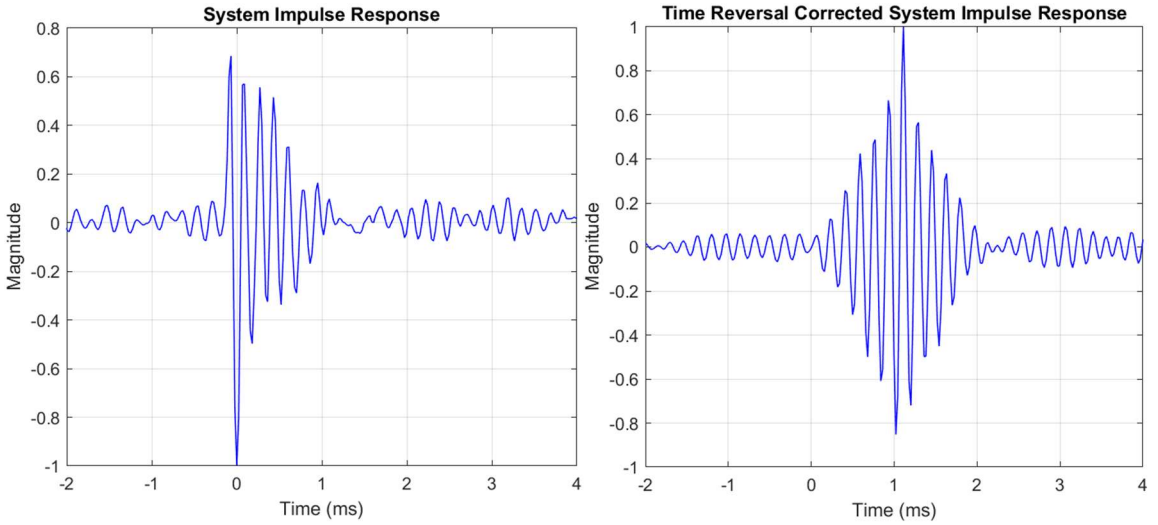

Figure 4.28: Samsung Galaxy Prime, Snowball Ice system impulse response at 0 degrees, 90% power truncated time reversal filter corrected

As seen in Figure 4.27 and Figure 4.28, a time reversal correction filter makes the impulse response even symmetric. A performance improvement is especially seen in Figure 4.27 where the ringing reduces to less than 40% of the peak. This particular impulse response would thrive in a serial code acquisition approach since selecting a false phase is unlikely. Figure 4.28 becomes even symmetric, however significant ringing over 80% of the peak occurs. Despite even symmetry, it is hardly an improvement since uncorrected maximum ringing is also approximately 80%.

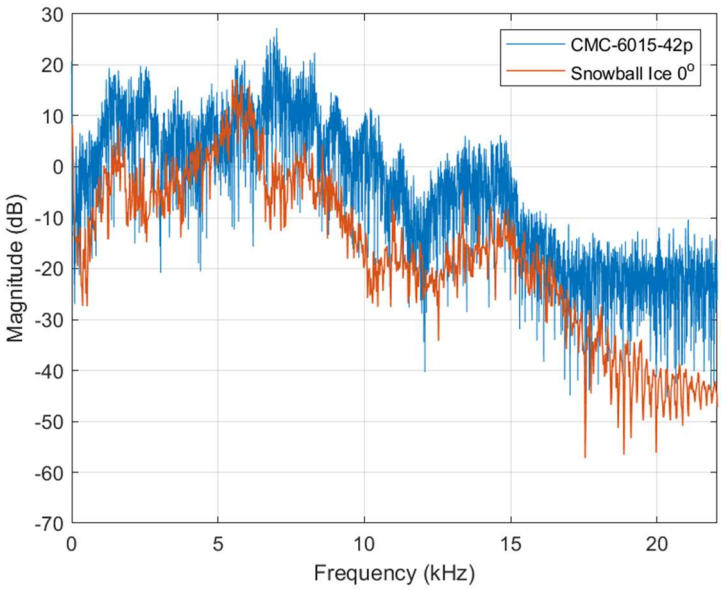

Figure 4.29: Samsung Galaxy Prime, custom Rx board and Snowball Ice system PSD

Figure 4.29 shows the PSD of the two systems. Note the system using the CMC-6015-42p has a flatter frequency response compared to the Snowball Ice. Note both PSD's have significant attenuation and do not take full advantage of the 20 kHz bandwidth. The CMC microphone performs well with less than 40% ringing, despite only using about 7 kHz of bandwidth. The Snowball Ice microphone has significant ringing, but has a small 3 dB bandwidth centered around 6 kHz. A relation between ringing and bandwidth is apparent. Section 4.4.5 will explore how to further correct the impulse response using magnitude correction.

4.4.3 Effect of Truncating the Correction Filter, h(t)

Truncating the correction filter minimizes computation resources. Figure 4.30 shows the 90% energy truncated time reversal correction filter for the Samsung Galaxy Prime and custom receiver board pair. This truncation reduces the filter length from over 200 to 72. Recall the original TR correction filter shown in Figure 4.26.

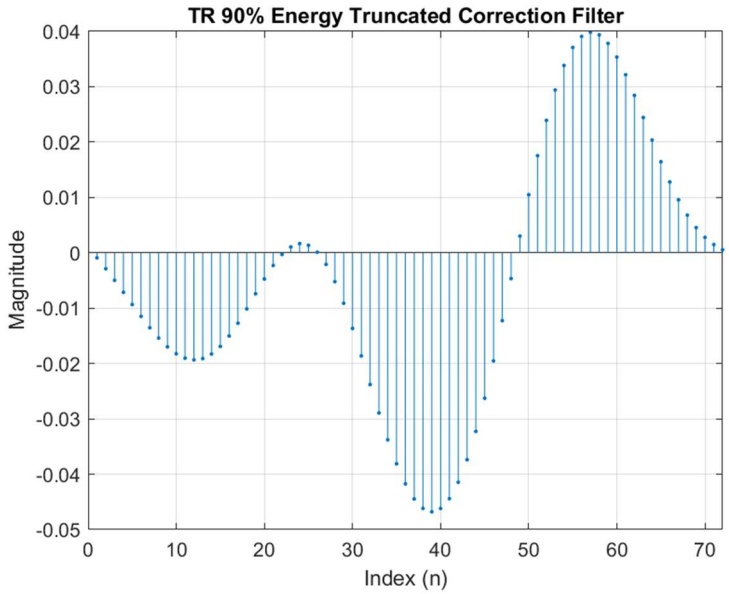

Figure 4.30: 90% energy truncated TR correction filter

Figure 4.31 shows the normalized corrected system impulse response at different truncation lengths. 100% energy is the full TR correction while 0% energy is no correction filter. Notice how as the correction filter gets shorter, the impulse response moves back to odd symmetry. Visually, the point of diminishing returns is at around 90% energy; increasing the filter length to 100% energy hardly improves performance. Equation (4.18) gives the equation to calculate correction filter energy.

$$E = \int_0^T h(t)^2 dt \tag{4.18}$$

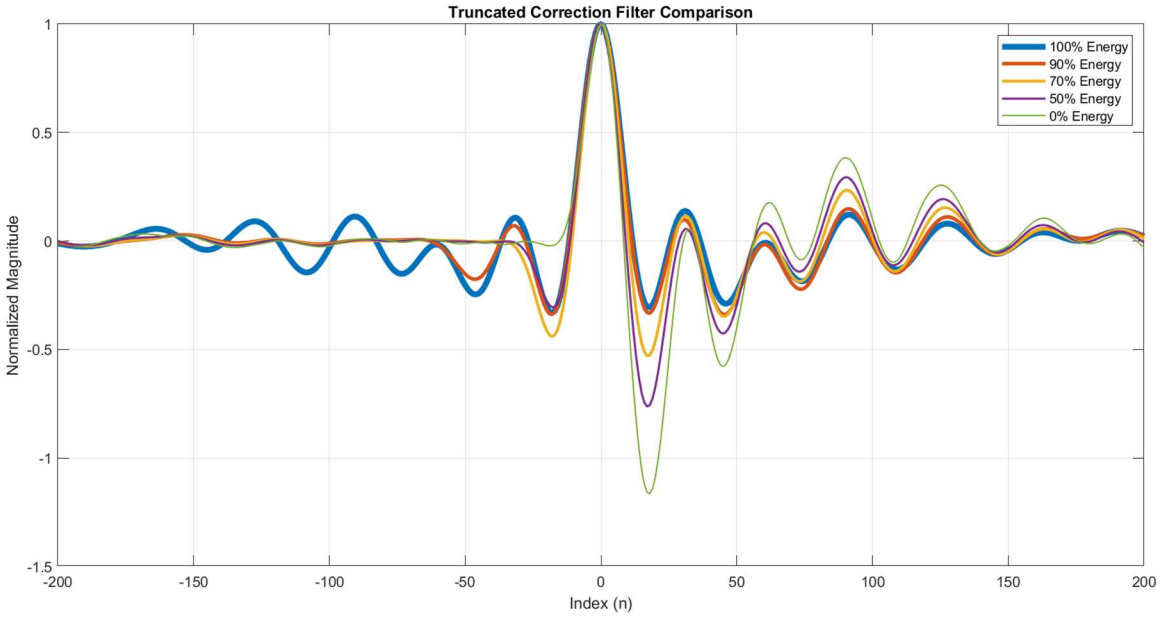

Figure 4.31: Corrected system impulse response using a truncated correction filter

4.4.4 Correction Filter on Tx vs Rx

It is important to note that placing the Rx designed correction filter on the Rx side is not equivalent to placing it on the Tx side. Rx designed correction filters refers to correction filters that are designed for the Rx side. Sections 4.4.1 and 4.4.2 discusses methods to design Rx correction filters. Figure 4.32 shows the LTI model between the two. Placing a digital correction filter on the Tx inherently samples the PN analog waveform. Without an anti-alias filter, sampling and reconstruction on the Tx end introduces distortion to the ideal PN analog waveform. This extra distortion leads to degraded correction performance, not to mention complicating the transmitters and reducing the power efficiency. Using an anti-alias filter adds another block to the LTI model, and requires re-characterization of the system impulse response for correction filter design.

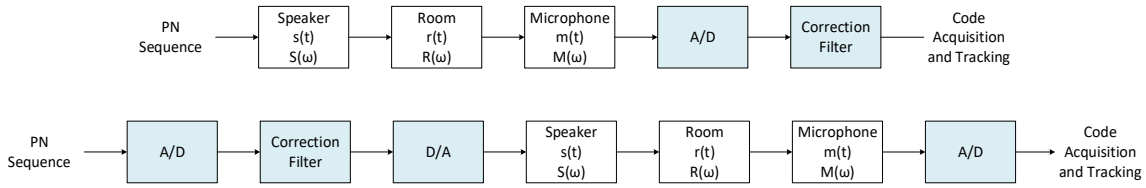

Figure 4.32: Correction filter on Rx side (top) vs Tx side (bottom) model

Figure 4.33 and Figure 4.34 confirm that it is not equivalent to place the Rx designed correction filter on the transmitter side when considering implementation. Both figures show the corrected impulse response between the Samsung Galaxy Prime and custom receiver board. As expected, the performance degrades when placing the Rx designed correction filter on the Tx side. More ringing occurs with the Rx designed correction filter on the Tx side, therefore a Rx designed correction filter should not be on the Tx side. Additionally, since placing the correction filter on the Tx side complicates the transmitter and adds hardware, the correction filter should only be placed on the Rx side.

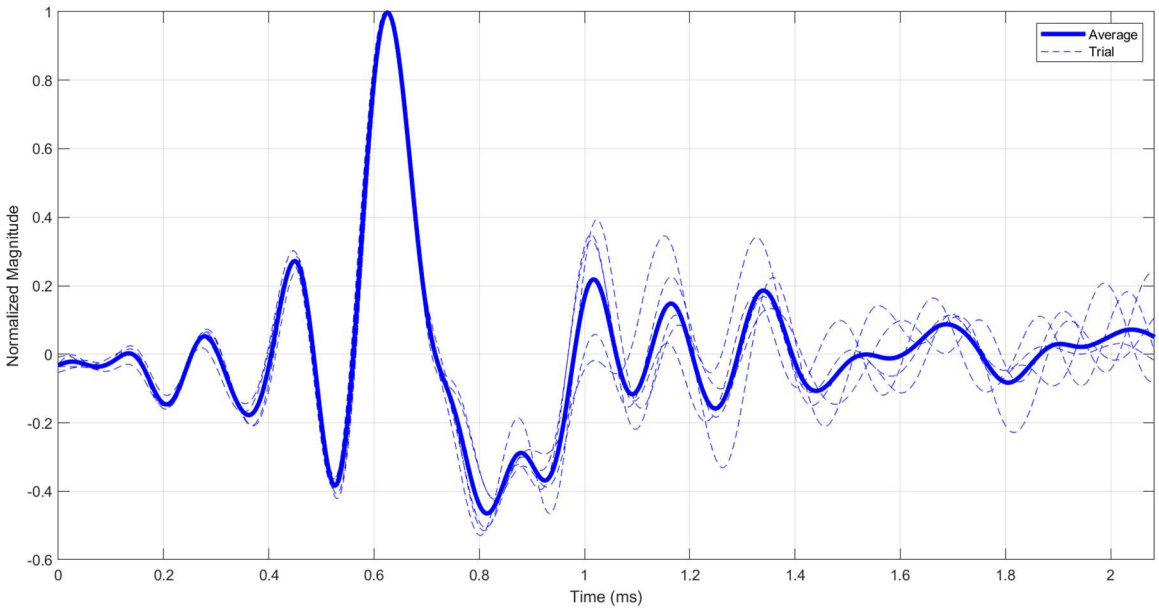

Figure 4.33: Corrected system impulse response with correction filter on Tx side

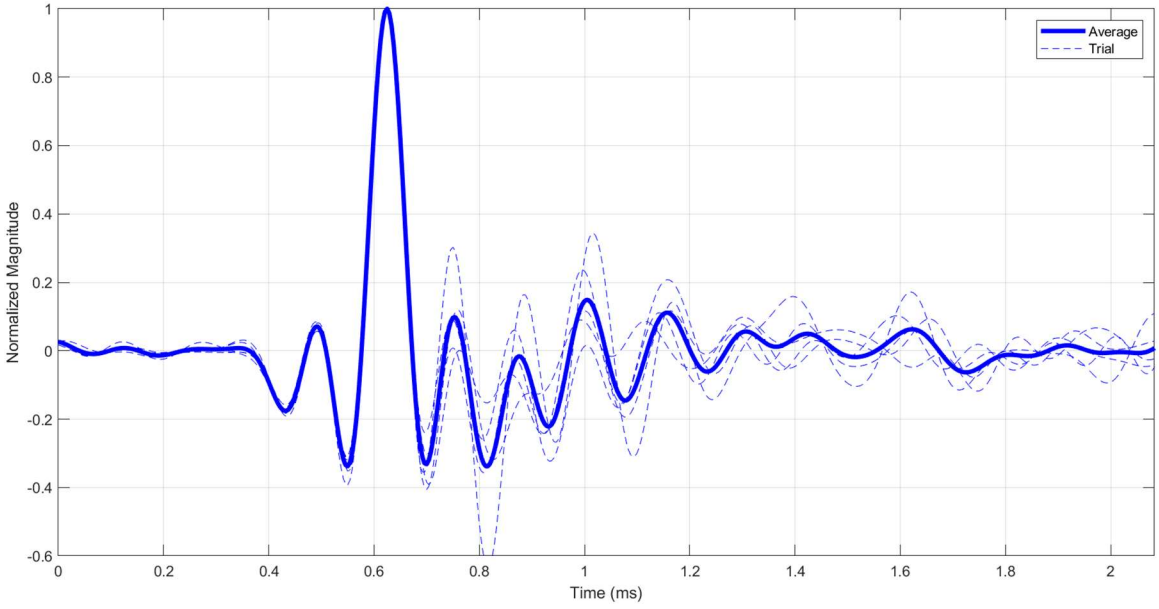

Figure 4.34: Corrected system impulse response with correction filter on Rx side

4.4.5 Magnitude Correction

Magnitude correction explores the effect of leveling out the PSD. The intuition comes from viewing the system impulse response and PSD of the Samsung Galaxy Prime with the custom receiver board and Snowball Ice microphone. Those plots are shown in Figure 4.28 and Figure 4.29. The Snowball Ice microphone had an impulse response with significantly more ringing and also a narrower 3 dB bandwidth centered around 6 kHz.

Magnitude correction uses a linear phase FIR filter designed by the frequency sampling method [42] [43]. The FIR filter is first designed to level out the PSD, then small incremental changes are made through trial and error and visual inspection to optimize performance. Table 4.6 shows the final FIR filter coefficients. Figure 4.37 shows the FIR filter magnitude and phase frequency response. Figure 4.36 shows the uncorrected and corrected PSD. The corrected PSD has a flatter response, as desired.

Figure 4.35 shows the original system impulse response, the TR phase corrected impulse response, the magnitude corrected impulse response, and phase and magnitude corrected impulse response. With magnitude correction alone, the time duration of ringing reduces. After applying phase correction to the magnitude corrected impulse response, the results are astounding. The duration and magnitude of ringing is significantly reduced. The ringing magnitude has dropped from approximately 75% of the peak down to approximately 30% of the peak. Also note the delay introduced by applying a correction filter. This delay is not an issue for TDoA measurements as long as all transmitters are corrected by the same correction filter. This constraint is the source of the requirement for identical transmitting speakers.

Figure 4.38 shows the phase, magnitude, and phase and magnitude correction filters. The phase and magnitude correction filter is the convolution of the phase with the magnitude correction filter. Adding a magnitude correction increases the filter length by 20%. This extra length is well worth the cost to reduce the ringing from 75% down to 30%.

Both phase and magnitude correction are also essential to improving the system impulse response. In some cases, magnitude correction is necessary for accurate code acquisition and symbol decoding.

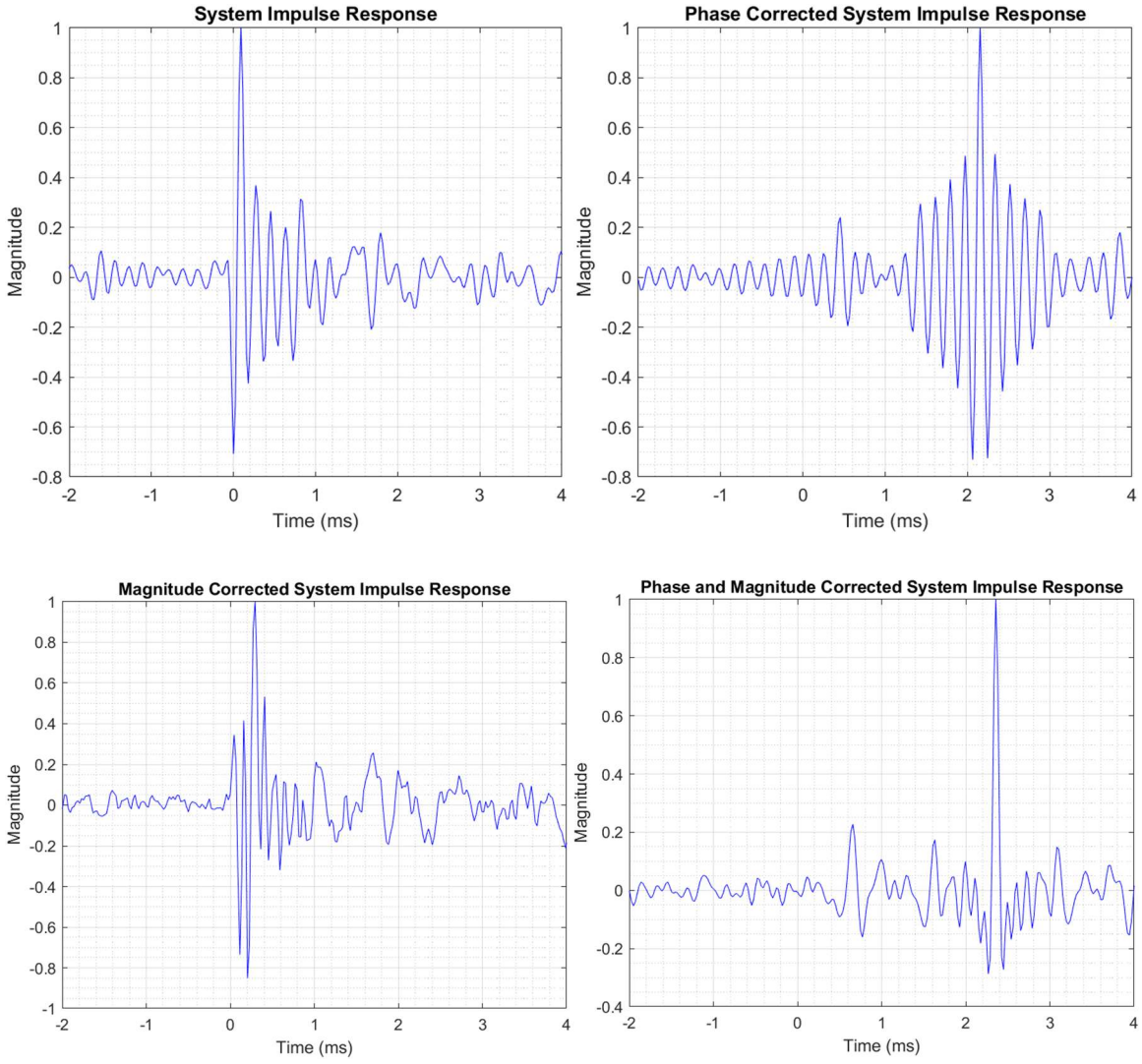

Figure 4.35: Samsung Galaxy Prime, HP Spectre x360 system impulse response with phase and magnitude correction

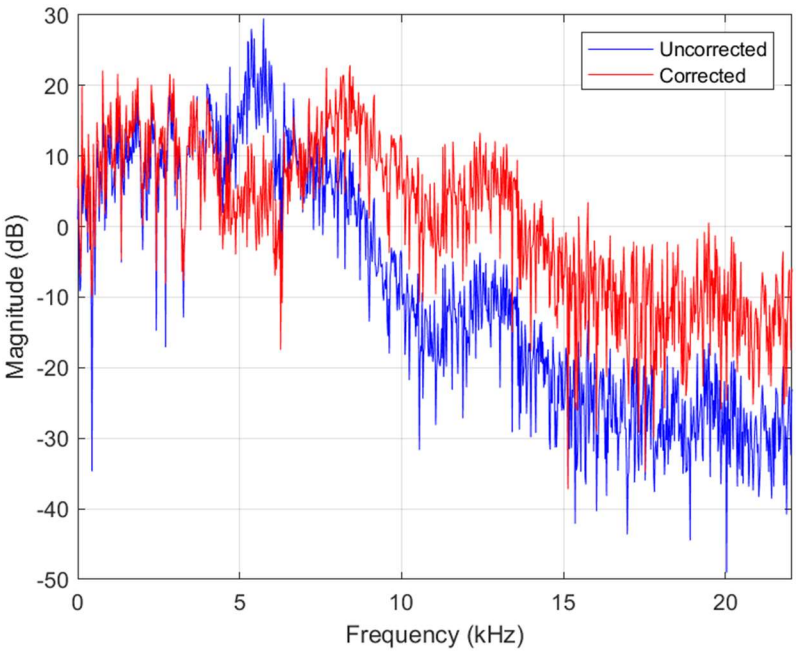

Figure 4.36: Samsung Galaxy Prime, HP Spectre x360 PSD

Table 4.6: Samsung Galaxy Prime, HP Spectre x360 FIR correction filter design by frequency sampling

Digital Frequency F (cyc/sample)	Magnitude
0/19	1
1/19	1
2/19	0.3
3/19	0.8
4/19	4
5/19	5
6/19	5
7/19	5
8/19	5
9/19	5

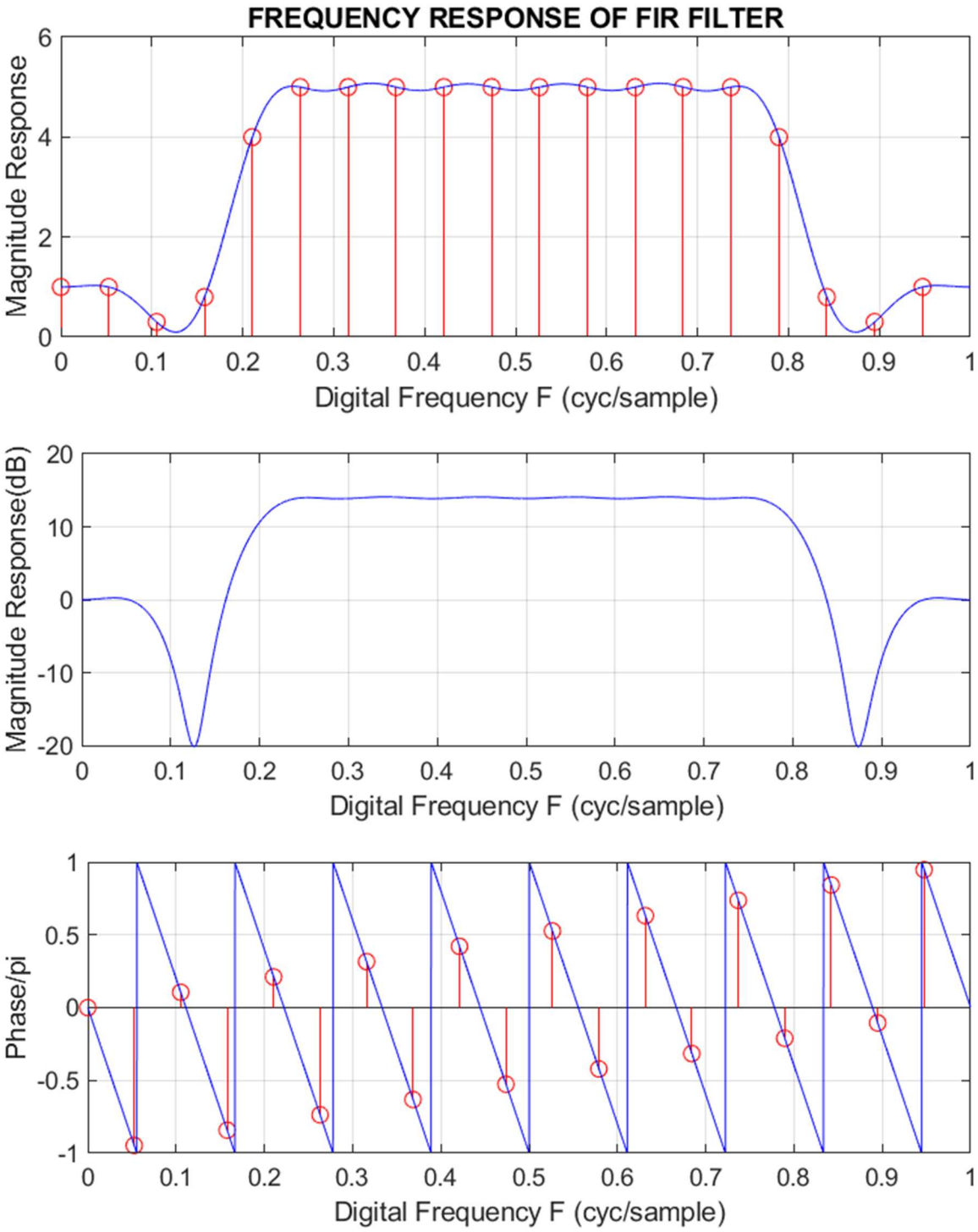

Figure 4.37: Samsung Galaxy Prime, HP Spectre x360 magnitude correction filter frequency response

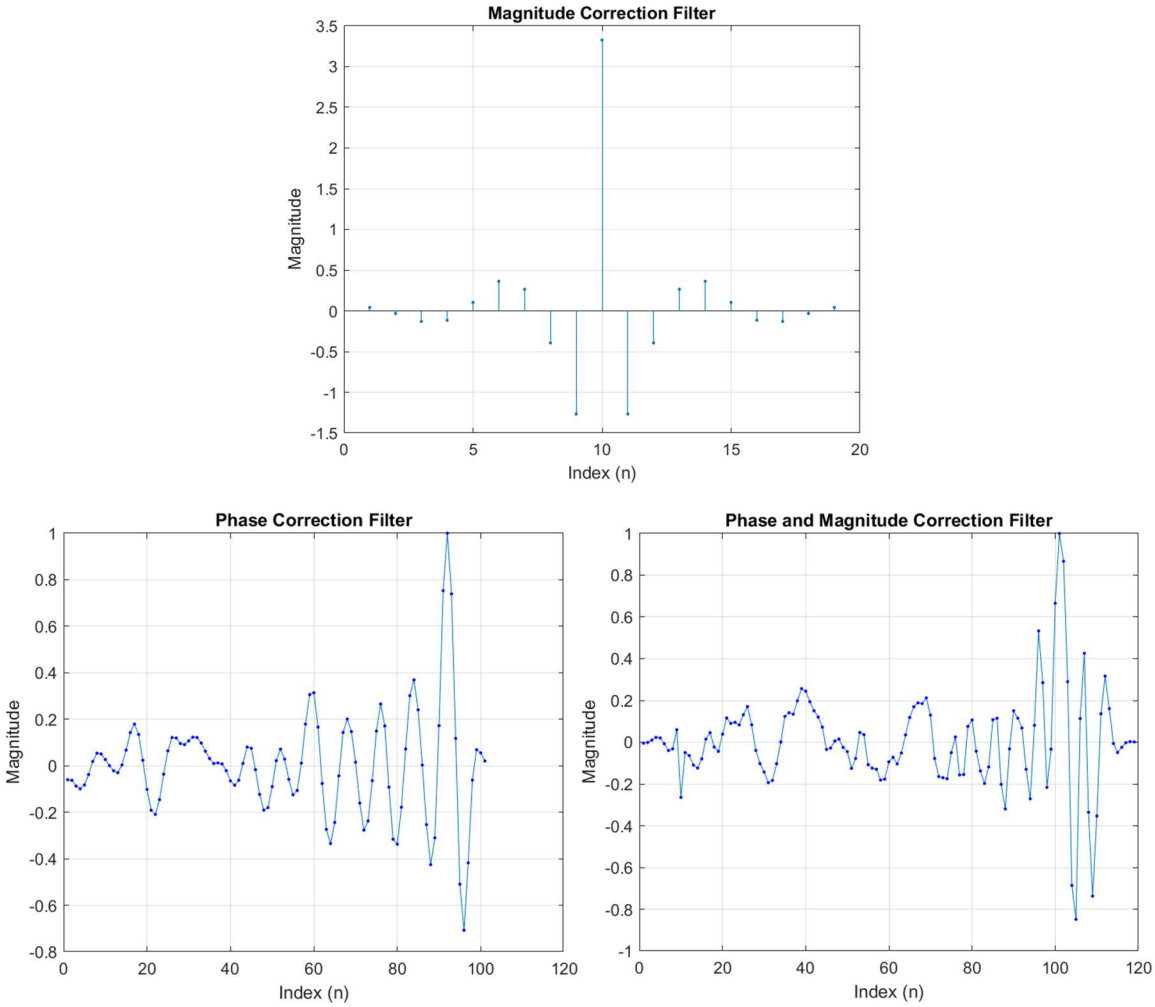

Figure 4.38: Samsung Galaxy Prime, HP Spectre x360 phase and magnitude correction filters

4.5 Simulated Infrastructure Tests

Two simulated infrastructure tests are run before implementing the infrastructure. The simulated infrastructure consists of 4 Gold codes transmitted from the same source. In the “Stacked Gold Codes” test, all 4 gold codes are aligned on top of each other. In the “345 Gold Code” test, Gold codes 2, 3, and 4 are spaced out to emulate 3, 4 and 5 meter path differences with respect to Gold code 1. The purpose of these tests is to confirm separation of multiple orthogonal Gold codes transmitted over the air. The correlated waveforms are only phase corrected for simplicity.

Figure 4.39 shows the “Stacked Gold Codes” test with phase correction. The correlated peaks of each code are aligned as expected. Figure 4.40 shows “345 Gold Codes” test is with phase correction. Gold codes 2, 3, and 4 emulated 3, 4 and 5 meter path differences with respect to Gold code 1, as expected. The simulated infrastructure tests are the final tests necessary to prove an IPS using acoustic PN based TDoA is possible.

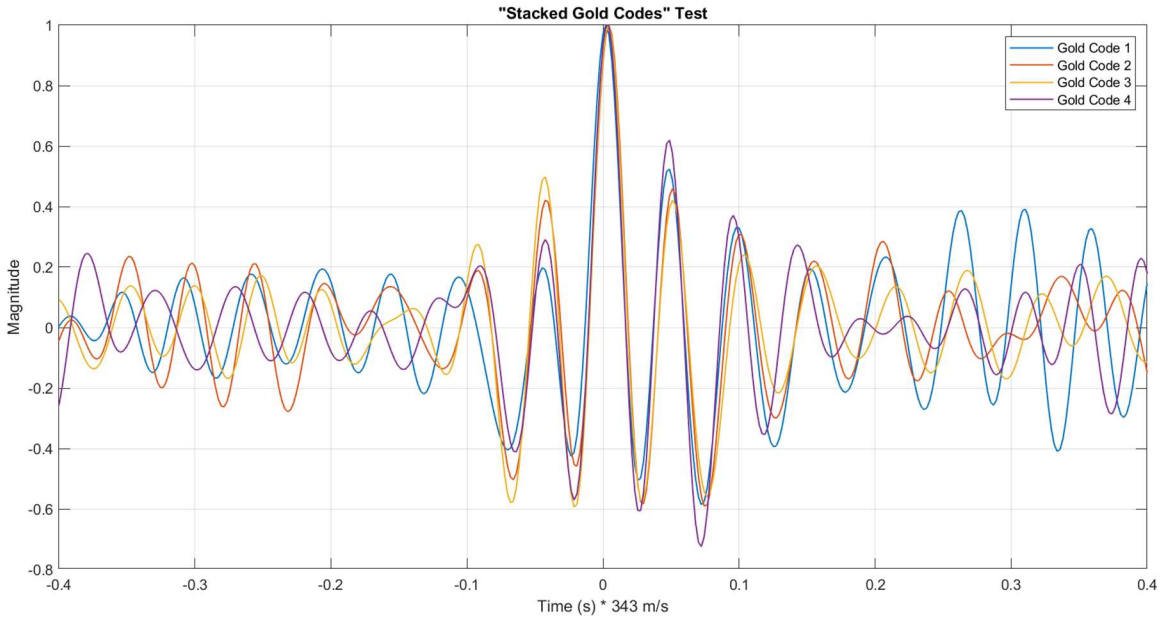

Figure 4.39: Stacked Gold codes test, after phase correction

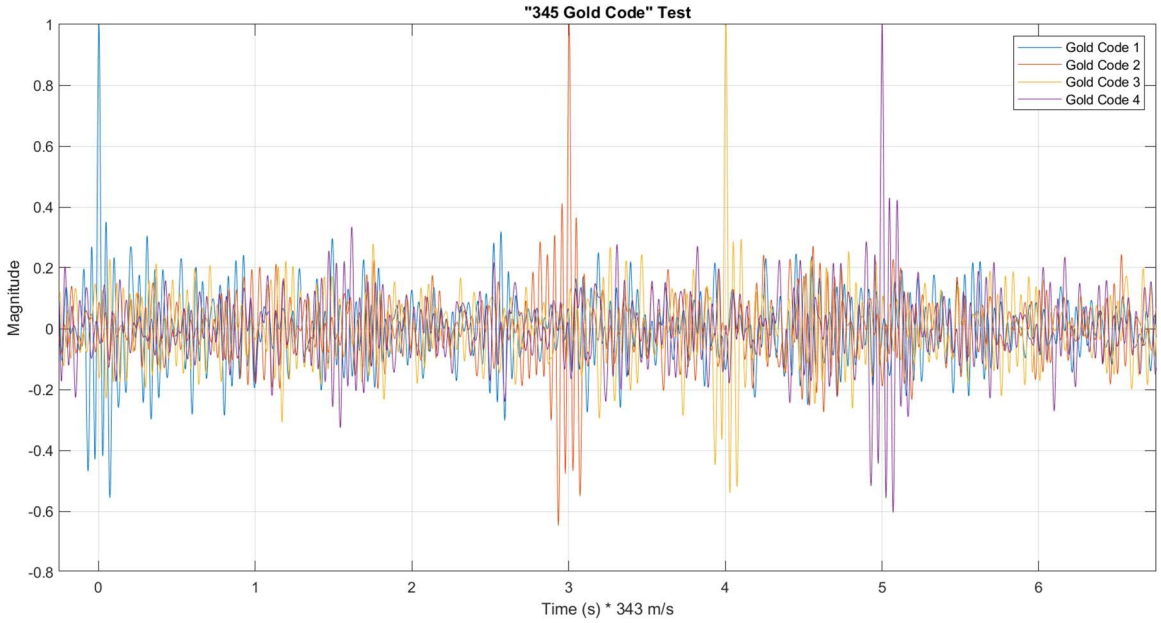

Figure 4.40: "345 Gold Code" test, after phase correction

4.6 Preliminary Testing Takeaways

Measuring the system impulse response allows for the design of a correction filter to optimize code acquisition and symbol decoding performance. The discussed MLS impulse response measurement method is accurate and also directly represents the waveform used during code acquisition and tracking. The pre-corrected system impulse response is odd symmetric and not suitable for code acquisition and symbol decoding. An LMS designed filter and TR correction filter phase corrects the system impulse response, making it even symmetric. Since both filters have similar performance, the TR filter is advantageous for its design simplicity. Finally, a linear phase FIR filter designed by frequency sampling magnitude corrects the system impulse response and reduces the ringing by flattening the PSD. The proposed IPS should always use phase and magnitude correction, as it is paramount to code acquisition and symbol decoding performance.

Results of preliminary testing prove the custom receiver board was and is well worth the effort. Discovery of magnitude correction and TR phase correction is largely due to testing with the custom receiver board. Comparison between Snowball Ice and custom receiver board pre and post corrected impulse responses provided key observations about correction filters; mainly that an even symmetric minimal ringing impulse response is possible. Moving forward the custom receiver board is useful for a real-time FPGA receiver implementation. Additionally, the custom receiver board impulse response serves as a “control” device with no black box behavior.

5 PROPOSED IPS TESTING

5.1 Test Setup

This section discusses the infrastructure, receiver and the testing environment for a four speaker implementation of the proposed IPS. The infrastructure consists of four synchronized transmitters at known locations. The receiver is the object to be located.

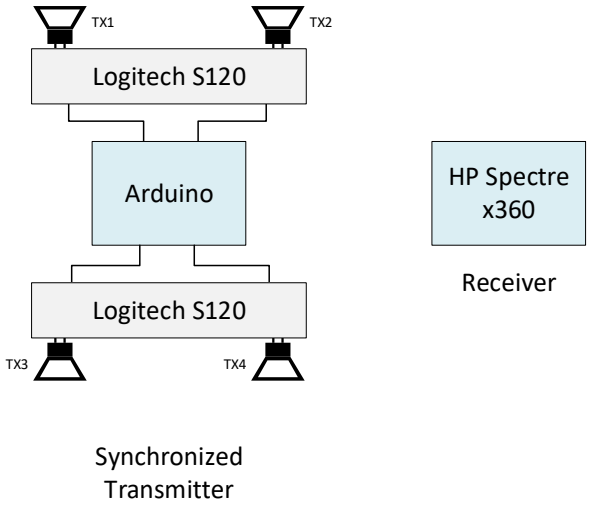

Figure 5.1: Required hardware for proposed IPS testing

5.1.1 Infrastructure

Logitech S120 stereo speakers, shown in Figure 5.2, are used as transmitters. The speakers are selected for its frequency response, AUX input capability, single speaker per channel topology, and low price. As seen from preliminary testing, larger bandwidth improves correlation performance. The Logitech S120 stereo speakers claim a 50 Hz – 20 kHz response bandwidth [30]. AUX input capability is desirable so a microcontroller can generate the Gold codes and drive the speakers directly without any amplification or power circuitry. The Logitech S120 stereo speakers also have volume control knobs, which provides flexibility during testing. Accurate infrastructure calibration requires a single speaker used on left and right channels. Section 5.2 discusses the calibration requirement. The stereo speakers are $8.49 on Amazon with Prime shipping [30].

Figure 5.2: Logitech S120 stereo speakers

An Arduino Uno generates the Gold sequences by toggling pins high and low. The output voltage of the Arduino is 0-5V, so a series 260kΩ resistor and 0.47µF capacitor AC couples the signal and limit the current to protect the Arduino and Logitech S120 speakers. An Arduino Uno is $21.90 on Amazon [44]. Figure 5.3 shows the Arduino wired up to Logitech S120 speakers.

Four speakers are used to simplify the test setup. This fulfills the transmitter requirement to position an object using TDoA measurements on a 2D plane [25] [28]. Table 5.1 shows the PN generation polynomials and tap points for each Gold code used with the transmitters. Refer to the Appendix for Gold code generation with tap points.

Table 5.1: Tx Gold code PN gen polynomials and tap points

$f_1(x)$	$x^{10} + x^3 + 1$
$f_2(x)$	$x^{10} + x^9 + x^6 + x^3 + x^2 + 1$
TX1	[2 6]
TX2	[3 7]
TX3	[4 8]
TX4	[5 9]

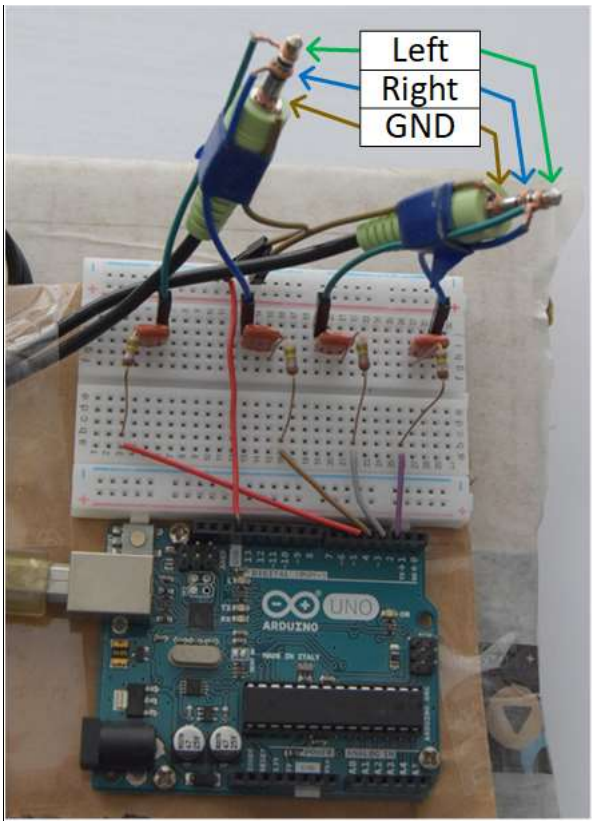

Figure 5.3: Infrastructure signal wiring

5.1.2 Receiver

The receiver is the object to be located and is the user of the positioning system. The receiver only requires a microphone and recording capability. For simplicity, a real time receiver is not implemented. Instead, the received signals are recorded and post-processed in Mathlab.

The HP Spectre x360 laptop is selected as the receiver for its portability, omnidirectional microphones, and availability. Figure 5.4 shows the HP Spectre x360. The custom receiver board has an omnidirectional microphone, but requires a portable oscilloscope to probe TP1 or hardware to read from the ADC to record data. Due to resource and time constraint, the custom receiver board is not a practical option during proposed IPS testing. The Snowball Ice microphone is portable, but has a cardioid radiation pattern [35].

Note that proposed IPS testing only uses one of the HP Spectre x360 stereo microphones. Additionally, HP's noise cancellation is turned off. HP's noise cancellation attempts to cancel the PN ranging signals and throws off results.

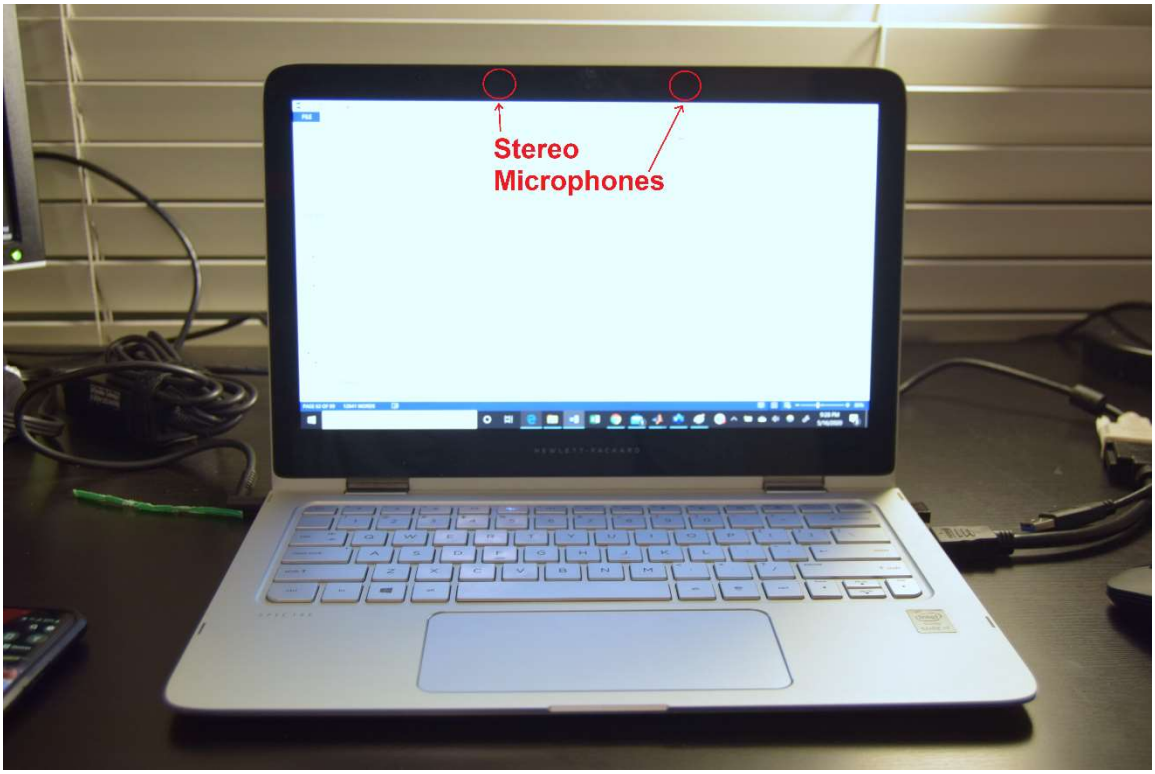

Figure 5.4: HP Spectre x360 microphone locations

5.1.3 System Characterization and Correction

Methods discussed in Sections 4.3.1 and 4.4 are used to measure the system impulse response and design a correction filter for the Logitech S120 speakers and HP Spectre x360. Figure 5.5 shows the phase and magnitude corrected impulse response. Notice how the uncorrected impulse response has less ringing compared to the CMC and Snowball system impulse responses. This is largely due to a flatter PSD. The Logitech speakers have a broader frequency response compared to the Samsung Galaxy Prime. The impulse response of the Logitech speakers is further improved after phase and magnitude correction.

The corrected Logitech S120 speakers and HP Spectre x360 system outperforms the Galaxy Prime and Snowball Ice corrected in Section 4.4.5 by approximately 10%. The Logitech corrected impulse response limits ringing to less than 20% of the peak compared to 30% in the Snowball Ice system. Recall that ringing will increase when Gold codes are used. Figure 5.9 shows the correlated waveforms when only transmitter 4

is transmitting. The Logitech system's ringing increases to approximately 30%. Also, as expected, correlating to orthogonal Gold codes yield a small cross correlation.

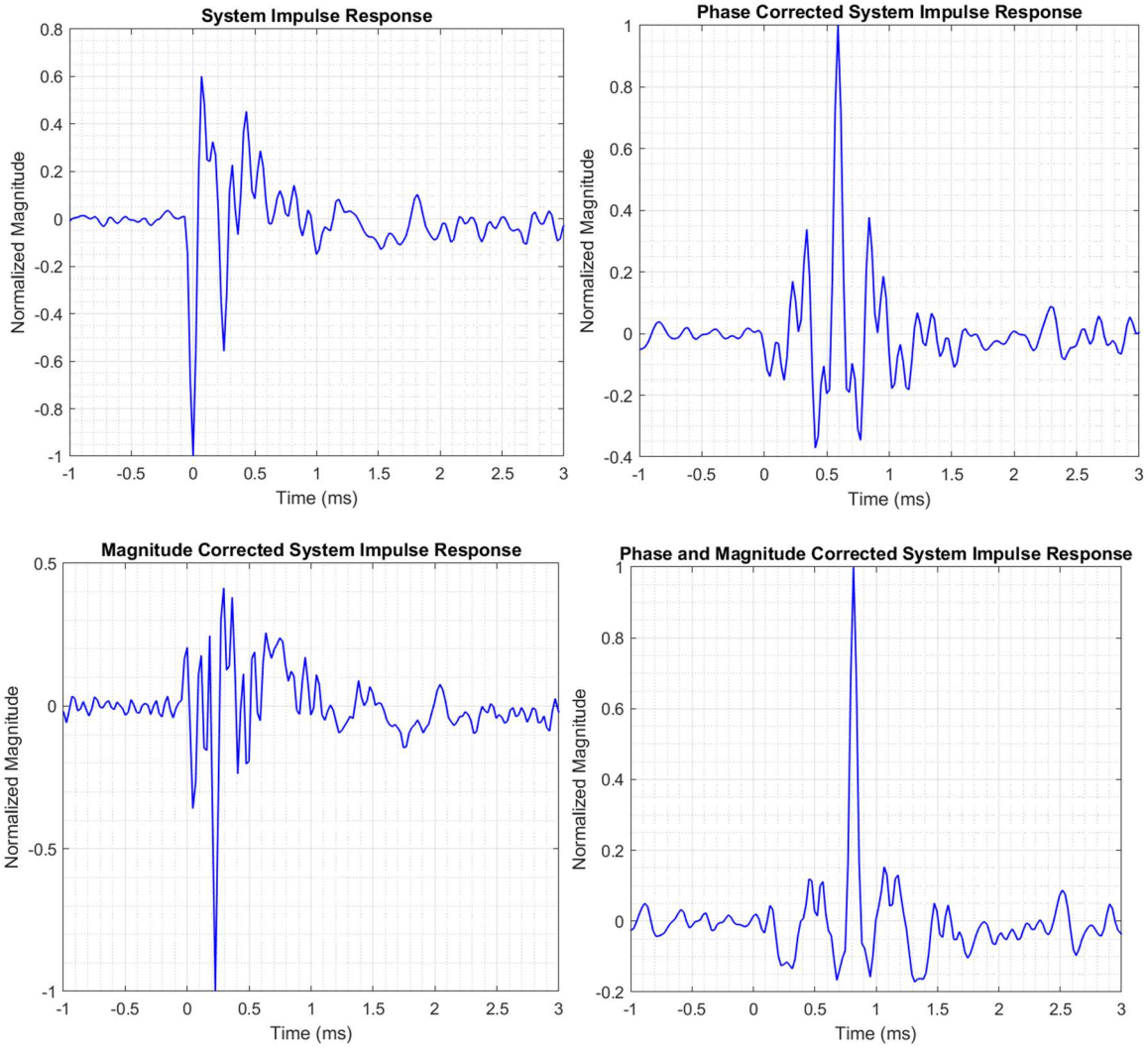

Figure 5.5: Logitech S120, HP Spectre x360 system impulse response phase and magnitude corrected

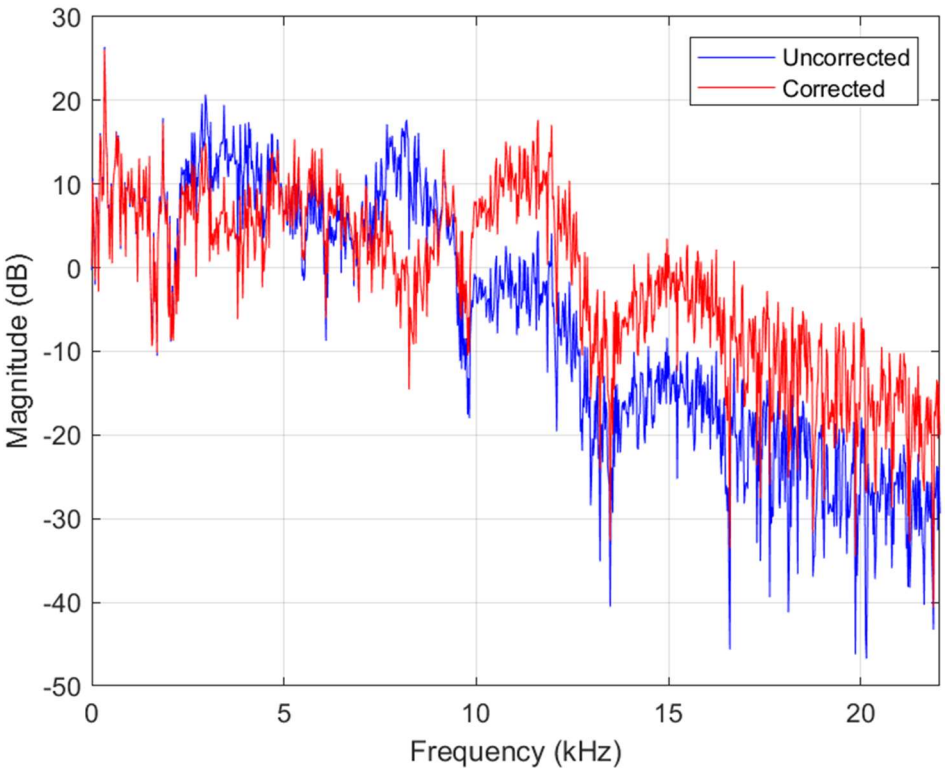

Figure 5.6: Logitech S120, HP Spectre x360 PSD

Table 5.2: Logitech S120, HP Spectre x360 correction filter design by frequency sampling

Digital Frequency F (cyc/sample)	Magnitude
0/21	2
1/21	1.8
2/21	1
3/21	3
4/21	0.4
5/21	8
6/21	8
7/21	8
8/21	8
9/21	8
10/21	8

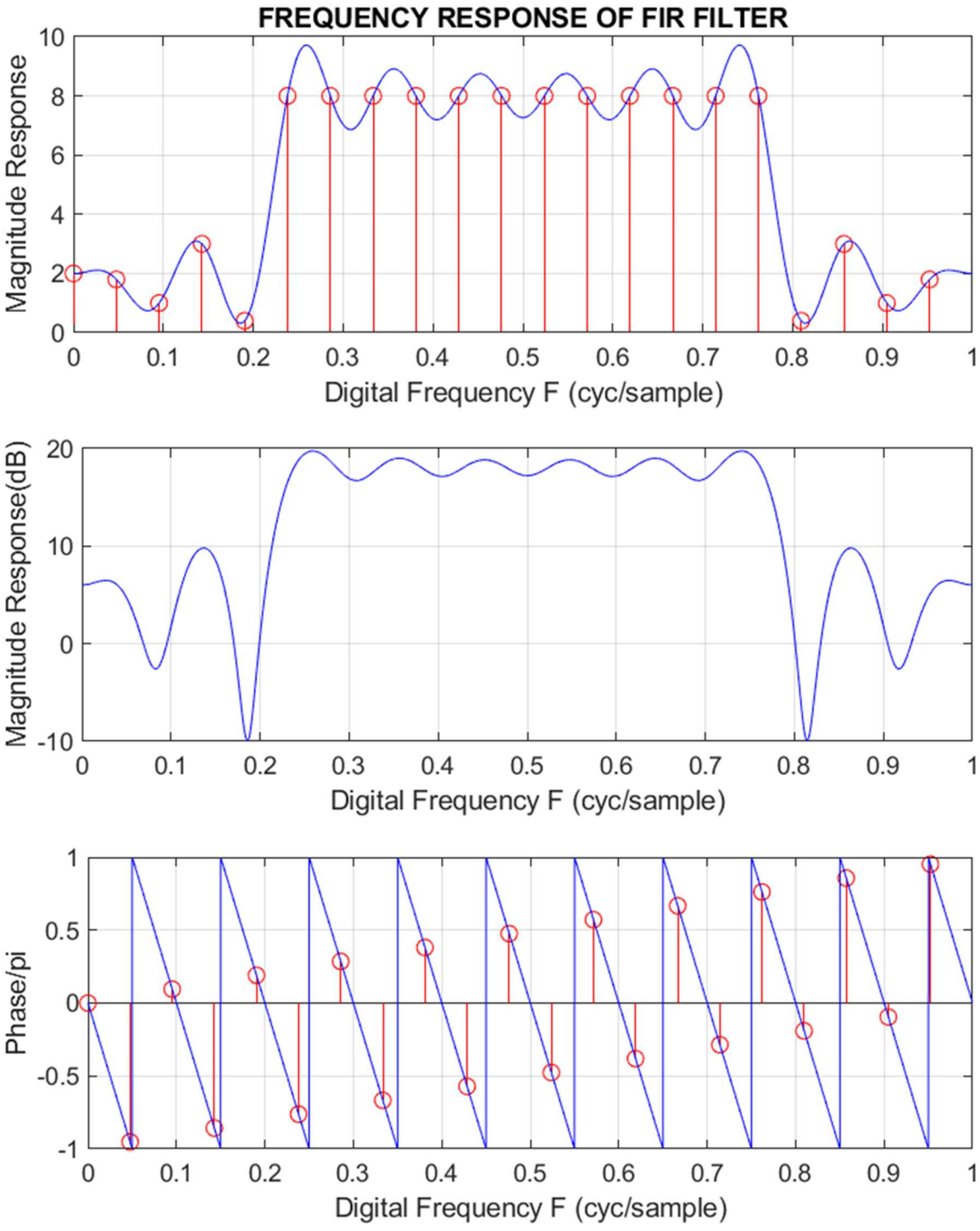

Figure 5.7: Logitech S120, HP Spectre x360 magnitude correction filter frequency response

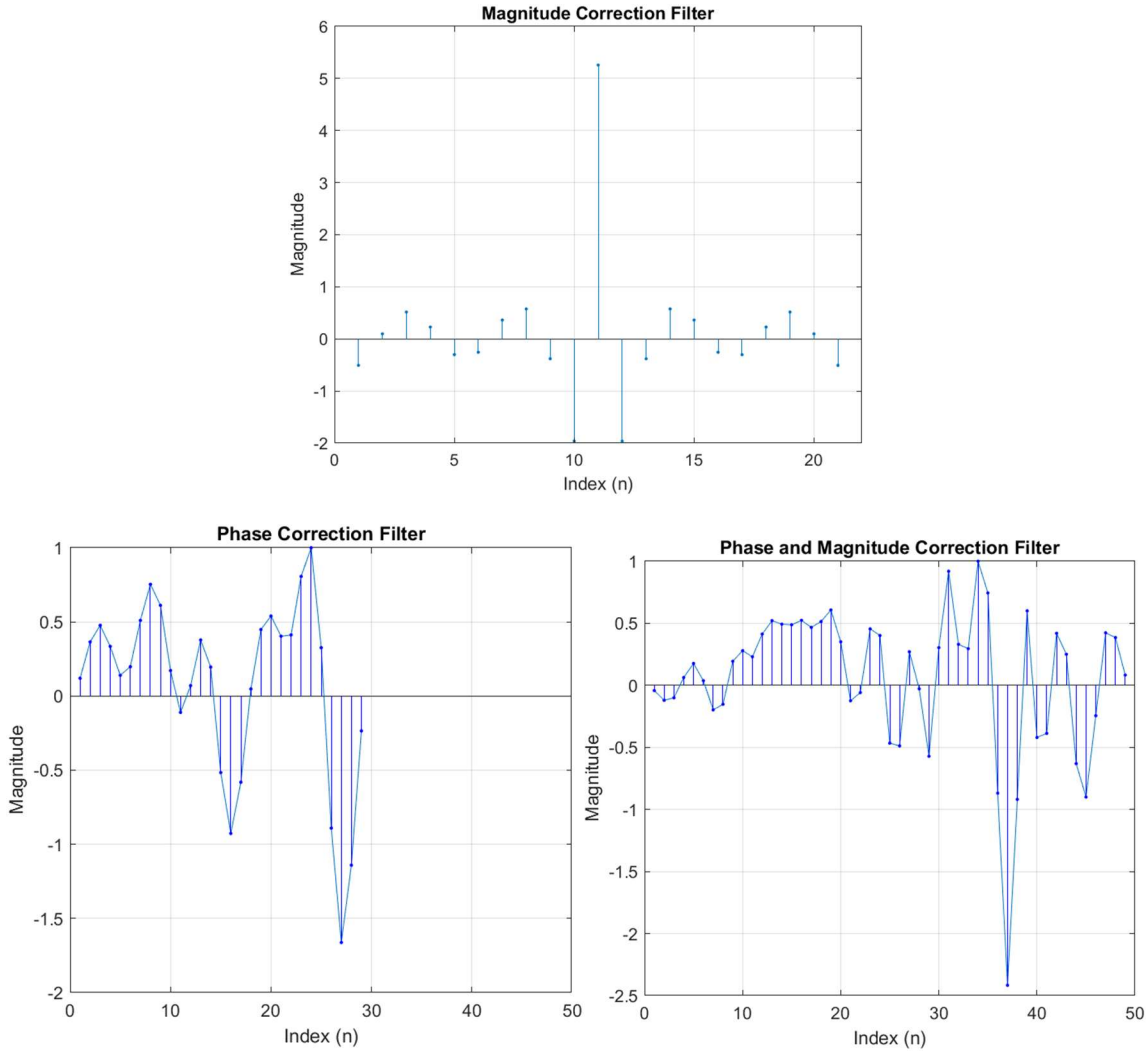

Figure 5.8: Logitech S120, HP Spectre x360 phase and magnitude correction filters

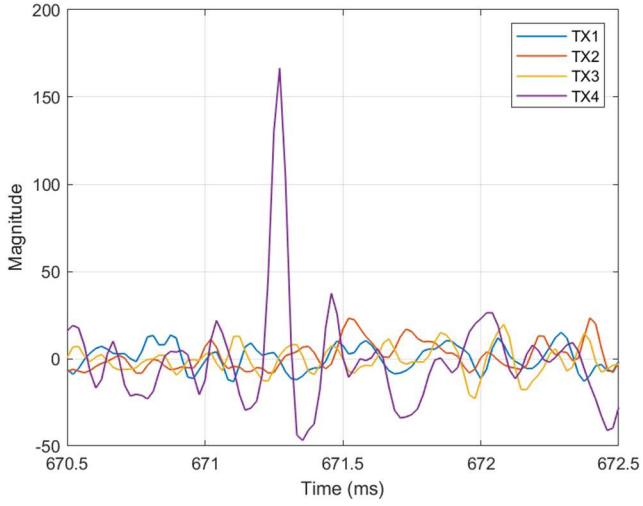

Figure 5.9: Received correlated waveform when only TX4 is transmitting

5.1.4 Testing Room

Figure 5.10 shows the room used during proposed IPS testing. It is a 12x12 ft living room with tile floor. The exposed hard surface was intentionally selected to test reflection and multi-path issues. Note each tile is approximately 1x1 ft. The room is not large enough for ranging ambiguity due to the symbol period. Recall Section 3.1 and Table 3.1, where Gold code length, and chipping period set a 28.77 ft range without ambiguity.

Figure 5.10: 12x12 ft room used for proposed IPS testing

5.2 Calibration Requirement

TDoA positioning algorithms require the position of infrastructure Tx node locations. Calibration refers to the measuring of the Tx node locations. The location of an object suffers from quantization error. Error in calibration measurements leads to ranging error which leads to object positioning error. Figure 5.11 shows Euclidian distance error due to quantization. Euclidian distance error due to quantization determines the calibration requirement.

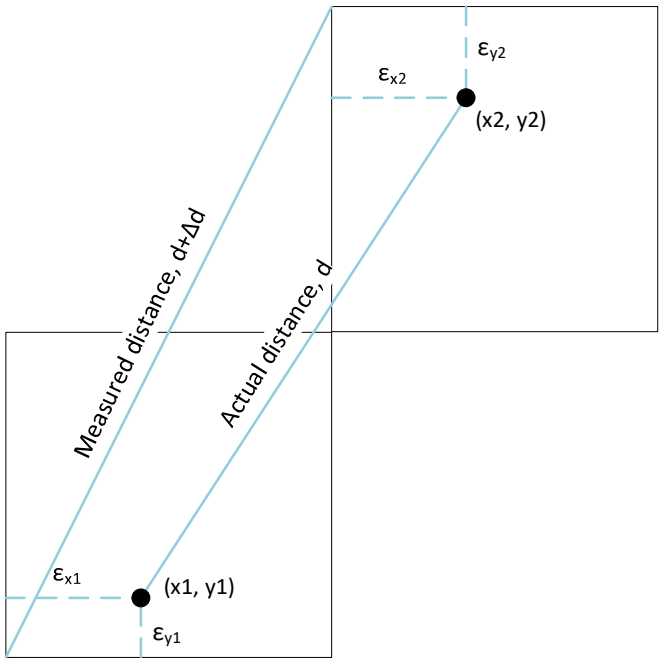

Figure 5.11: Euclidian distance error due to quantization

Equation (5.1) represents the actual Euclidian distance, d, between two 3D Cartesian coordinates. Calibration measurement error, ε, in the x, y and z components introduces a distance error, Δd, to the left side of the equation. Equation (5.2) represents this relation.

$$d = \sqrt{(x_1 - x_2)^2 + (y_1 - y_2)^2 + (z_1 - z_2)^2} \tag{5.1}$$

$$d + \Delta d = \sqrt{(\Delta x + \varepsilon)^2 + (\Delta y + \varepsilon)^2 + (\Delta z + \varepsilon)^2} \tag{5.2}$$

Solving for Δd, Equation (5.2) becomes Equation (5.3). Assuming small ε, Equation (5.3) becomes Equation (5.4). Finally, using a Taylor first order approximation, Equation (5.4) simplifies to Equation (5.5).

$$\Delta d = \frac{-2d \pm \sqrt{4d^2 + 4(2\varepsilon(\Delta x + \Delta y + \Delta z) + 3\varepsilon^2)}}{2} \tag{5.3}$$

$$\Delta d \approx \frac{-d \pm \sqrt{d^2 + 2\varepsilon(\Delta x + \Delta y + \Delta z)}}{1} \tag{5.4}$$

$$\Delta d \approx \frac{\varepsilon(\Delta x + \Delta y + \Delta z)}{d} \tag{5.5}$$

Euclidian distance error, Δd, is at a maximum when $\Delta x = \Delta y = \Delta z$. Equation (5.6) solves for worst case Euclidian distance error, Δd, from Equation (5.5). The Appendix shows the full Euclidian distance error due to quantization derivation.

$$\max(\Delta d) \approx \pm\sqrt{3}\varepsilon \tag{5.6}$$

Figure 5.12 shows the actual Euclidian distance error, Δd, and the approximated Euclidian distance error by Equations (5.5) and (5.6). In the plot Δy and Δz are held constant at 1m, ε is 0.1m, and Δx sweeps from 0.1m-2m. Note that the approximation is more accurate with smaller ε. The plot proves Equations (5.5) and (5.6) are good approximations to the actual error. Worst case Euclidian distance error occurs when $\Delta x = \Delta y = \Delta z$. Conversely, axis aligned points minimize error.

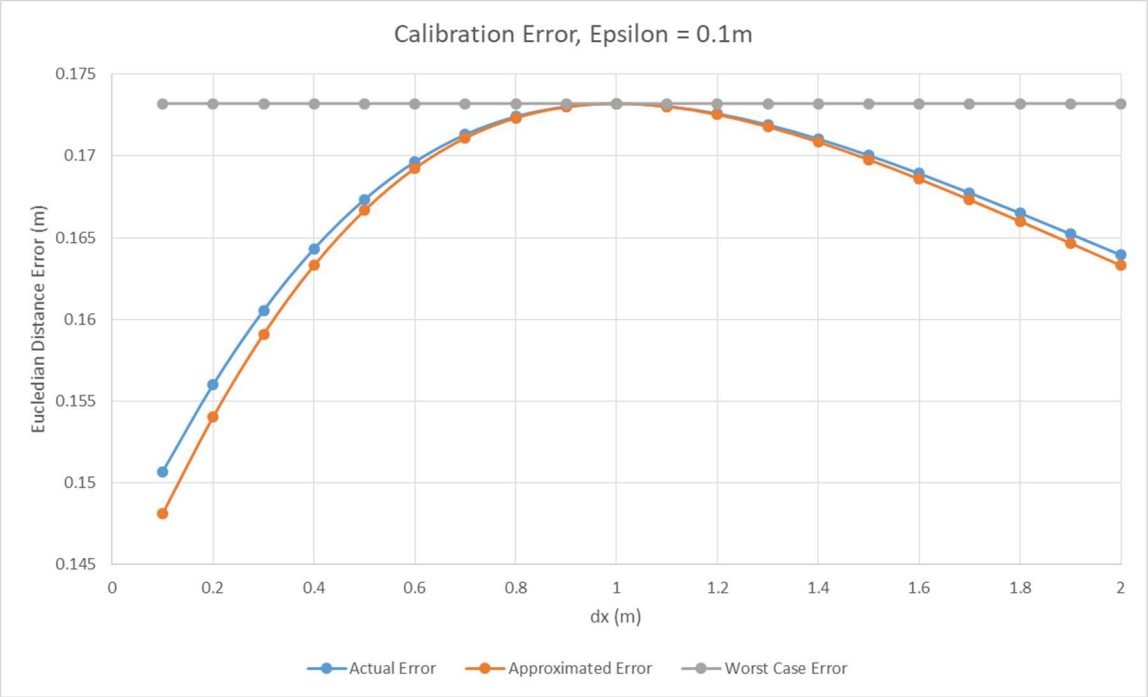

Figure 5.12: Approximated vs actual Euclidian distance error due to measurement calibration error

ToF ranging resolution, ΔR, is a function of wave speed and sampling frequency, shown in Equation (5.7) [45].

$$\pm\Delta R = \frac{1}{2} * \frac{c}{F_s} \tag{5.7}$$

The ranging error due to quantization, Δd, should not overpower ranging resolution, ΔR. This requirement yields Equation (5.8). Substituting Equations (5.6) and (5.7) into (5.8) and solving for epsilon yields Equation (5.9).

$$\max(\Delta d) < \Delta R \tag{5.8}$$

$$\varepsilon < \pm\frac{1}{2\sqrt{3}} * \frac{c}{F_s} \tag{5.9}$$

When the wave speed is 343 m/s and sampling frequency is 44.1 kHz, $\varepsilon < \pm 0.22cm$.

5.2.1 Speaker Impact on Calibration

Proposed IPS testing in this paper models speakers as a point source centered at the diaphragm of the speaker for calibration purposes. This paper does not study the validity of the model across various speaker shapes and sizes. However, measurements in Section 5.3 and 5.4 prove the model is valid with the Logitech S120 stereo speakers.

Note that multiple speakers per Gold code throws off calibration, correction filters and code acquisition. So, the IPS should not use woofer, tweeter speaker pairs or stereo speakers used as mono. Stereo speakers used as mono causes a multipath effect, since both speakers are spatially separated and transmit the same signal. Similarly, a spatially separated tweeter, woofer pair causes a variable phase shift dependent on receiver to transmitter geometry. In addition to being a requirement, a single speaker per Gold code also reduces implementation expenses.

5.3 Multipath

Multipath occurs when the transmitted signal takes two or more paths to reach the receiver. Reflections in the propagation environment cause multipath. Figure 5.13 shows a 2D multipath example where d1 and d2 are path distances between the Tx and Rx. The path difference poses a problem to code acquisition, as it results in a second peak in the correlation.

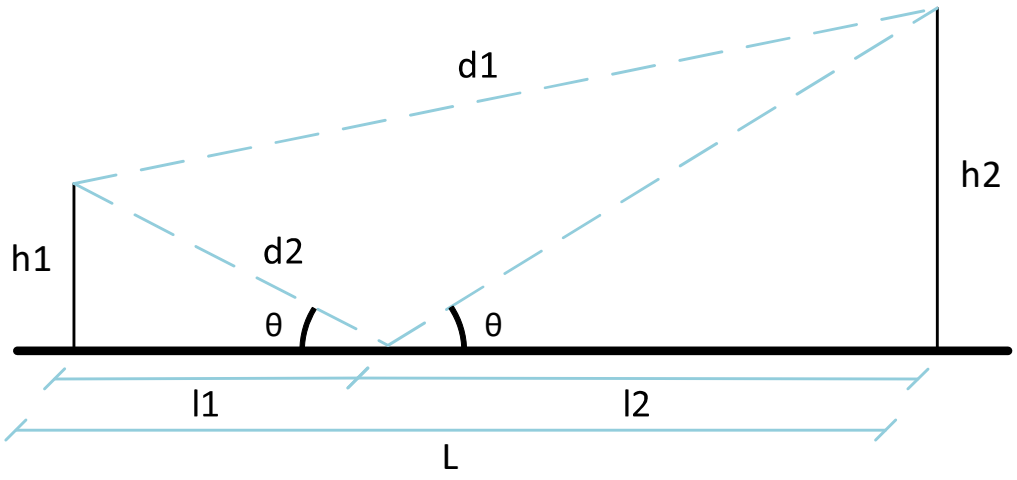

Figure 5.13: 2D multipath model

Multipath tests verify the 2nd peak is due to multipath and not from a faulty correction filter. Figure 5.14 shows the multipath test setup. The Logitech S120 speakers and HP Spectre x360 are on the ground. The Tx and Rx locations are measured to a precision of 0.5cm, as determined by the calibration requirement. Additionally, Tx and Rx are x-aligned to further minimize ranging error due to quantization.

The multipath test consists of measuring the time between peaks at various Tx and Rx spacing. The spacing sweeps from 2-6ft in increments of 1 foot. Figure 5.15 shows the overlaid correlations, aligned to the first peak. Each plotted correlations is the average of 10 trials. Table 5.3 shows the calculated expected and measured time differences between peaks.

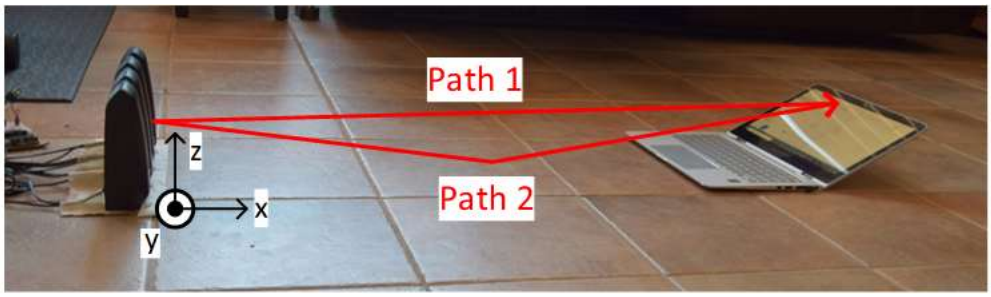

Figure 5.14: Multipath test setup

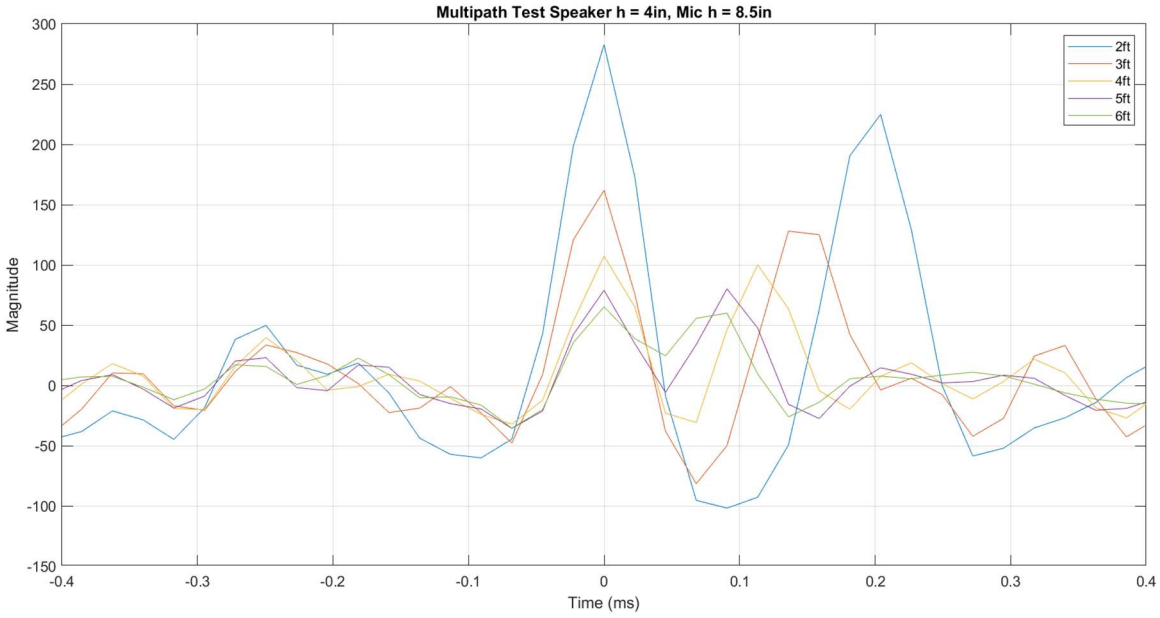

Figure 5.15: Multipath test magnitude and phase corrected correlation, h1=4in, h2=8.5in

Table 5.3: Multipath test calculated vs measured peak time differences, h1=4in, h2=8.5in

L (ft)	Calculated (ms)	Measured (ms)	Error (ms)
2	0.1956	0.2041	0.0085
3	0.1354	0.1361	0.0007
4	0.1030	0.1134	0.0104
5	0.0829	0.0907	0.0078
6	0.0694	0.0680	-0.0013

The error between calculated and measured time differences are less than half the sampling period. So, the error between the measured and calculated distance is within an acceptable range of error. Matching measured and expected time differences confirms the second peak is due to multipath. This also confirms that meeting the calibration requirement result derived in Section 5.2 yields accurate ranging measurements.

Figure 5.15 also shows that multipath time difference decreases as Tx, Rx spacing, L, increases. When the path difference is small, the second peak is close in magnitude to the first peak. The second peak becomes stronger relative to the first peak as the path difference decreases. This relates to acoustic attenuation, which refers to energy loss in a propagating sound wave. When the spacing is 5 and 6ft, the multipath delay is so small that the first and second peak side lobes are merged. Multiple peaks of equal magnitude is undesirable for code acquisition, as it may lock to the wrong peak leading to ranging error.

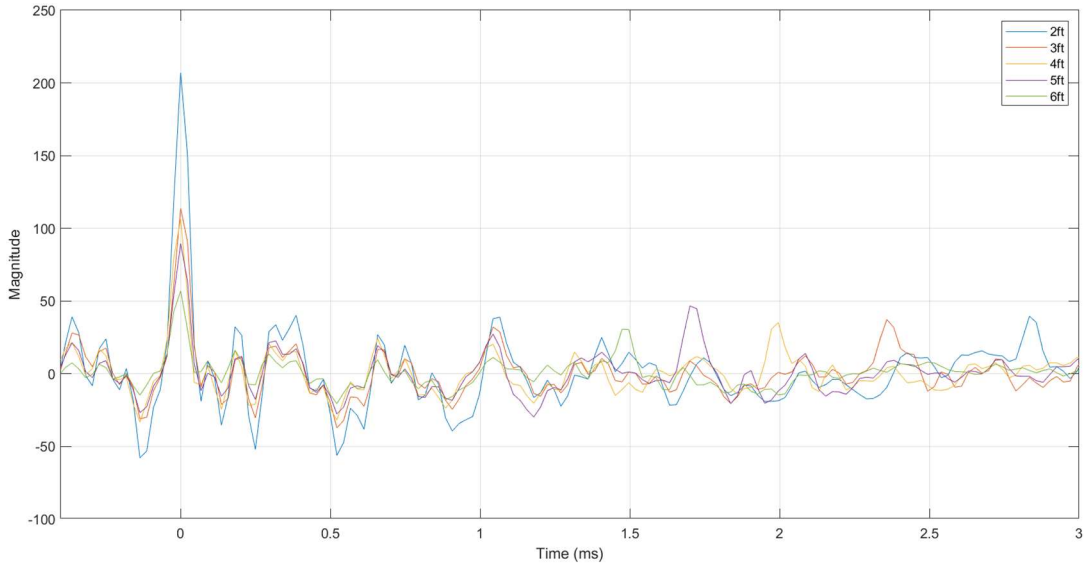

Figure 5.16: Multipath test magnitude and phase corrected correlation, h1=28in, h2=26.5in

Maximizing Tx height normal to flat surfaces is one method to combat multipath. This maximizes the path difference, and minimizes the height of the second peak. Figure 5.16 shows the same multipath test with the height increased to 28 in and 26.5 in for Tx and Rx and respectively. At the new Tx and Rx heights, the maximum path delay happens at a 2ft spacing and is equal to 2.6ms. Figure 5.16 shows the correlated

waveforms up to 3ms to look for multipath peaks. The multipath peaks have diminished and are buried in the noise floor of the correlation. Special DLL and discriminator designs in code acquisition and tracking can also combat multipath [14] [19] [20].

5.4 TDoA Measurements

Accurate TDoA measurements is the final proof of concept step for the proposed IPS. Figure 5.17 shows the TDoA measurement test setup. The infrastructure is equally spaced on the y axis by 10cm, for ease of calibration. The transmitters are elevated so multipath is not an issue and the HP Spectre x360 is on the ground to enable accurate microphone position measurements. Tx and Rx locations are accurate within 0.5cm, which is within 0.6mm of the calibration requirement derived in Section 5.2.

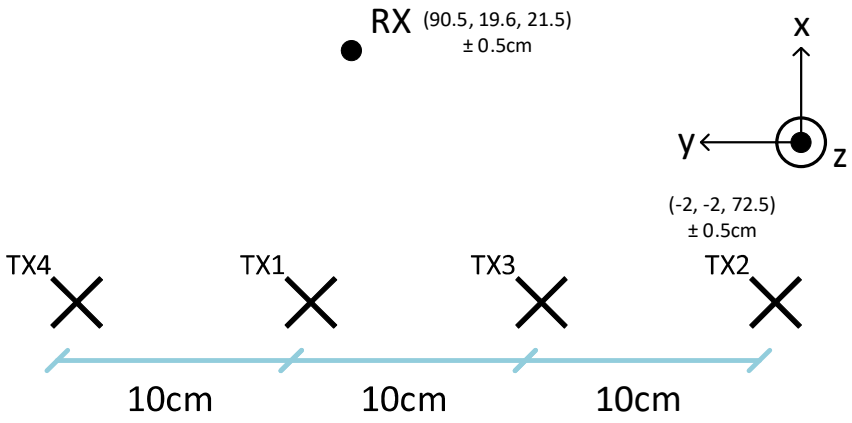

Figure 5.17: TDoA measurement test setup coordinate system

Figure 5.18 shows the received correlated waveforms. As expected, TX3 and TX2 have smaller peaks since they are further away from the Rx. Table 5.4 shows the measured time differences vs the calculated time differences. The error is less than half the sampling period, which is acceptable.

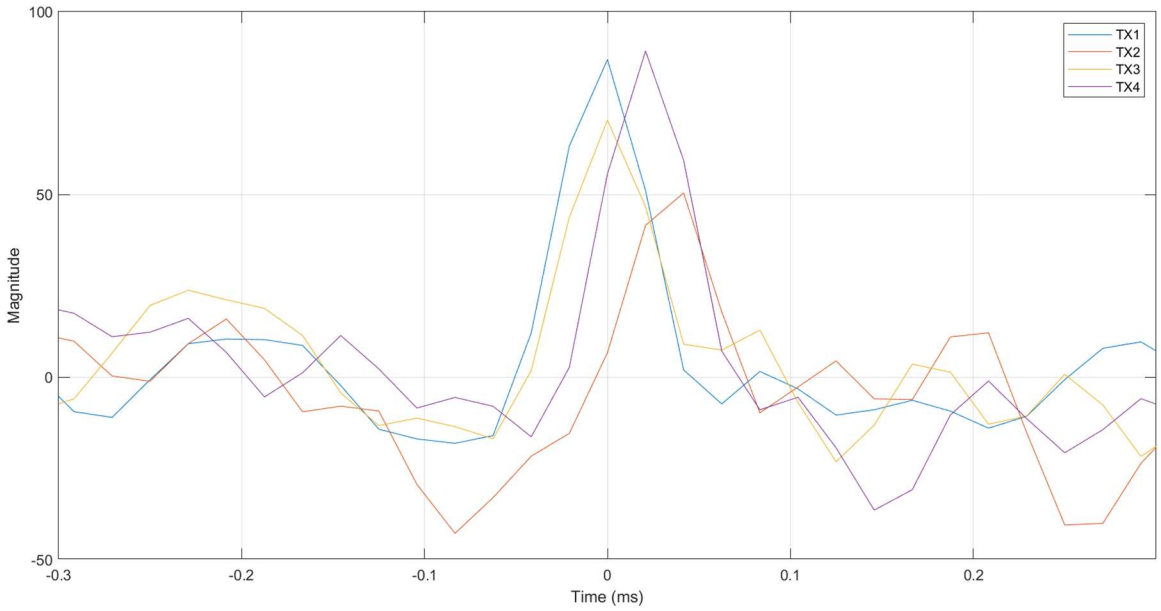

Figure 5.18: Phase and magnitude corrected TDoA measurement correlation result corresponding to Figure 5.17 test setup

Table 5.4: TDoA measured vs calculated results

	Calculated (µs)	Measured (µs)	Error (µs)
t2-t1	42	45	-4
t3-t1	7	0	7
t4-t1	20	23	-2

The proposed IPS produces accurate TDoA measurements when properly calibrated. So, it is possible to position an object using the proposed method. Note that increasing the sampling frequency yields finer ranging resolution and TDoA measurements [45]. Per Section 5.2, increasing sampling frequency imposes a stricter calibration requirement.

Recall that multiple intersection points in the hyperboles determined from TDoA measurements cause position ambiguity [21]. Collinear transmitters, such as the test setup in Figure 5.17, have many ambiguous solutions. Section 5.5.1 discusses the impact of Tx location on system accuracy and the coverage map.

5.5 Positioning Accuracy and Coverage Area

Positioning accuracy depends upon TDoA measurement accuracy, the number of transmitters and their location, and the positioning algorithm used. Proved in Section 5.2, TDoA measurement accuracy depends upon ranging accuracy which itself depends upon sampling frequency and calibration accuracy. In general, as TDoA measurement accuracy increases, so does positioning accuracy. Increasing the number of transmitters can also increase positioning accuracy. Recall that position ambiguity exists when there are multiple intersections in hyperbolic equations obtained from TDoA measurements [21]. A minimum of 4 Tx are required for 2D positioning and a minimum of 5 Tx are required for 3D positioning to determine the unequivocal position of an object [25] [28]. However, there are still methods to estimate 3D location with 4 transmitters [28], or even 3 transmitters [24].

5.5.1 2D Positioning Simulation

A positioning simulation explores the practicality of the proposed IPS by viewing the coverage map with various infrastructure, receiver parameters. Thorough positioning algorithm comparison is outside the scope of this paper. For general observations, the positioning simulation only requires a well-known, easy to implement positioning algorithm. A well-known positioning algorithm allows for easy comparison with novel positioning methods since most literature compares results to well-known methods. An easy to implement algorithm allows quick development and research into the problem. Chan and Ho's 2D positioning method is both well-known and easy to implement since it provides a closed form solution [29].

The 2D simulation uses Chan and Ho's method with theoretical proposed IPS TDoA measurements to generate positioning accuracy and coverage maps for given implementations of the proposed IPS. Adjustable simulation parameters include Tx position, grid size, and sampling frequency. The appendix includes the pseudocode for this simulation. Several simulations are shown below.

Each plot has a 1x1cm resolution. Positioning error is plot on a log scale for a more meaningful plot. Note points with positioning error less than 1mm are clipped to show a 1mm positioning error. Points with positioning error greater than 10cm are represented with white points and are considered to have unacceptable error. The coverage maps are binary images where black represents points that can achieve at least 1cm accuracy and white represents points that cannot.

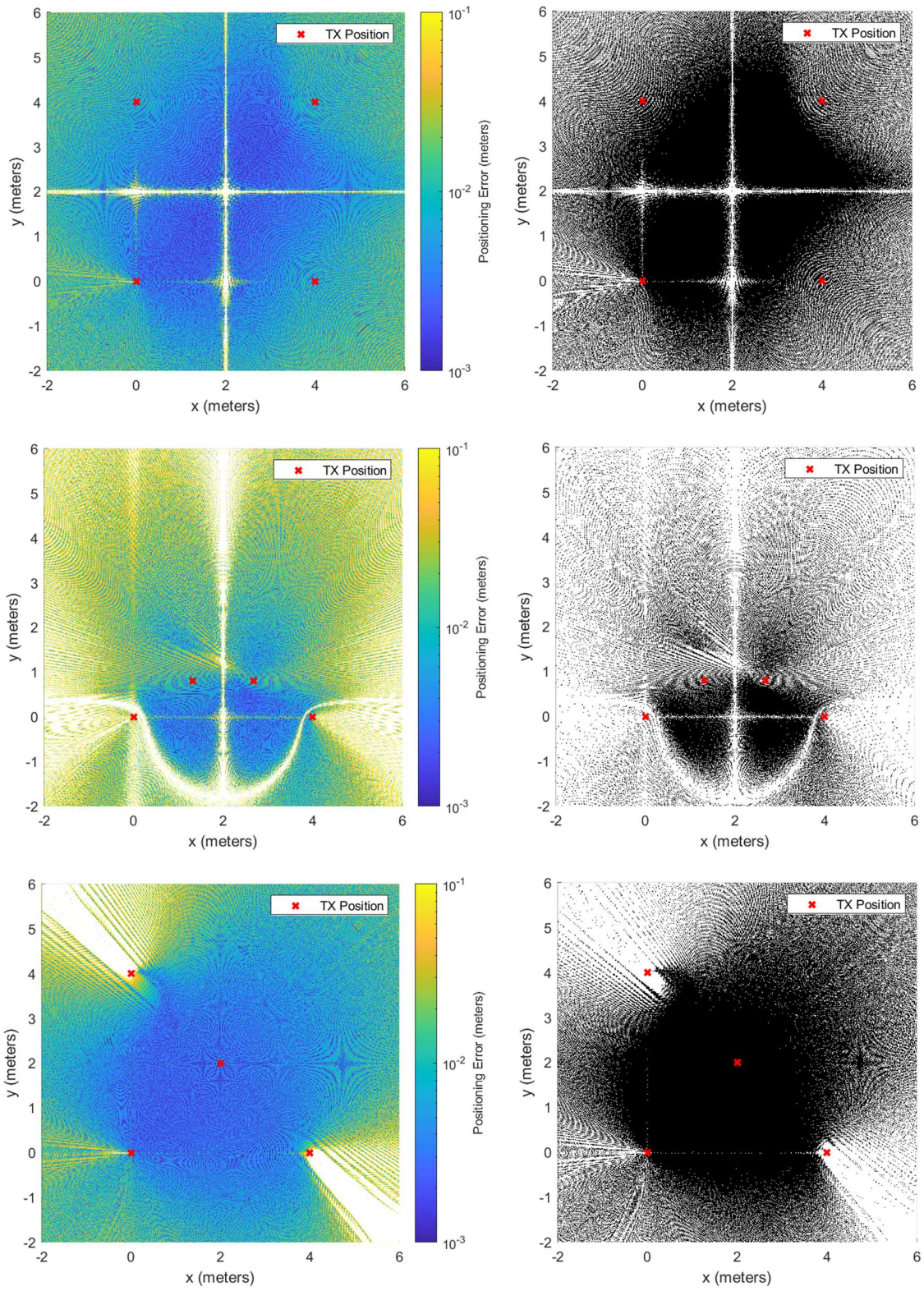

Figure 5.19: Positioning accuracy (left) and 1cm accuracy coverage map (right) using 4 transmitters in 3 different patterns

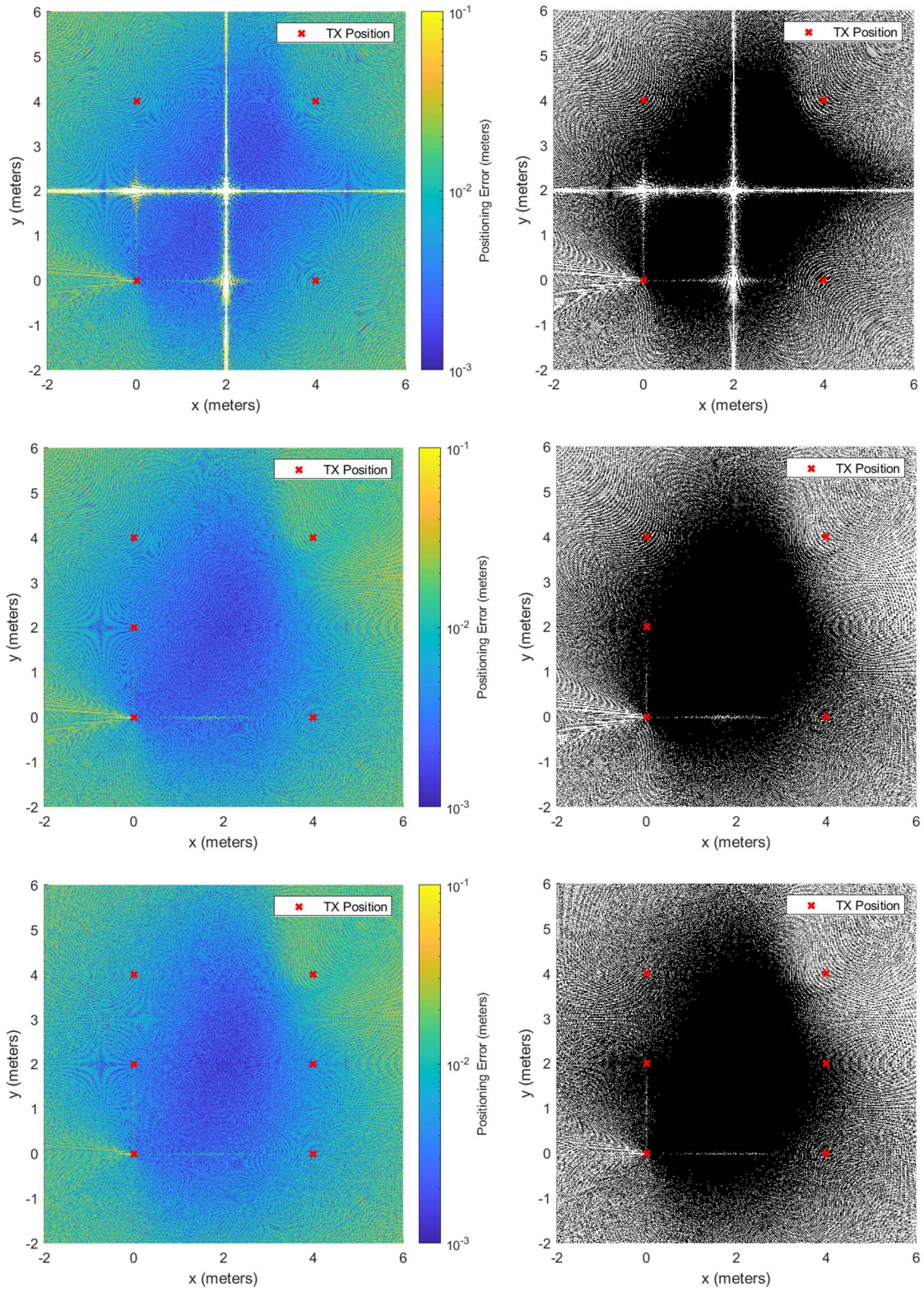

Figure 5.20: Positioning accuracy (left) and 1cm accuracy coverage map (right) using 4, 5, and 6 transmitters

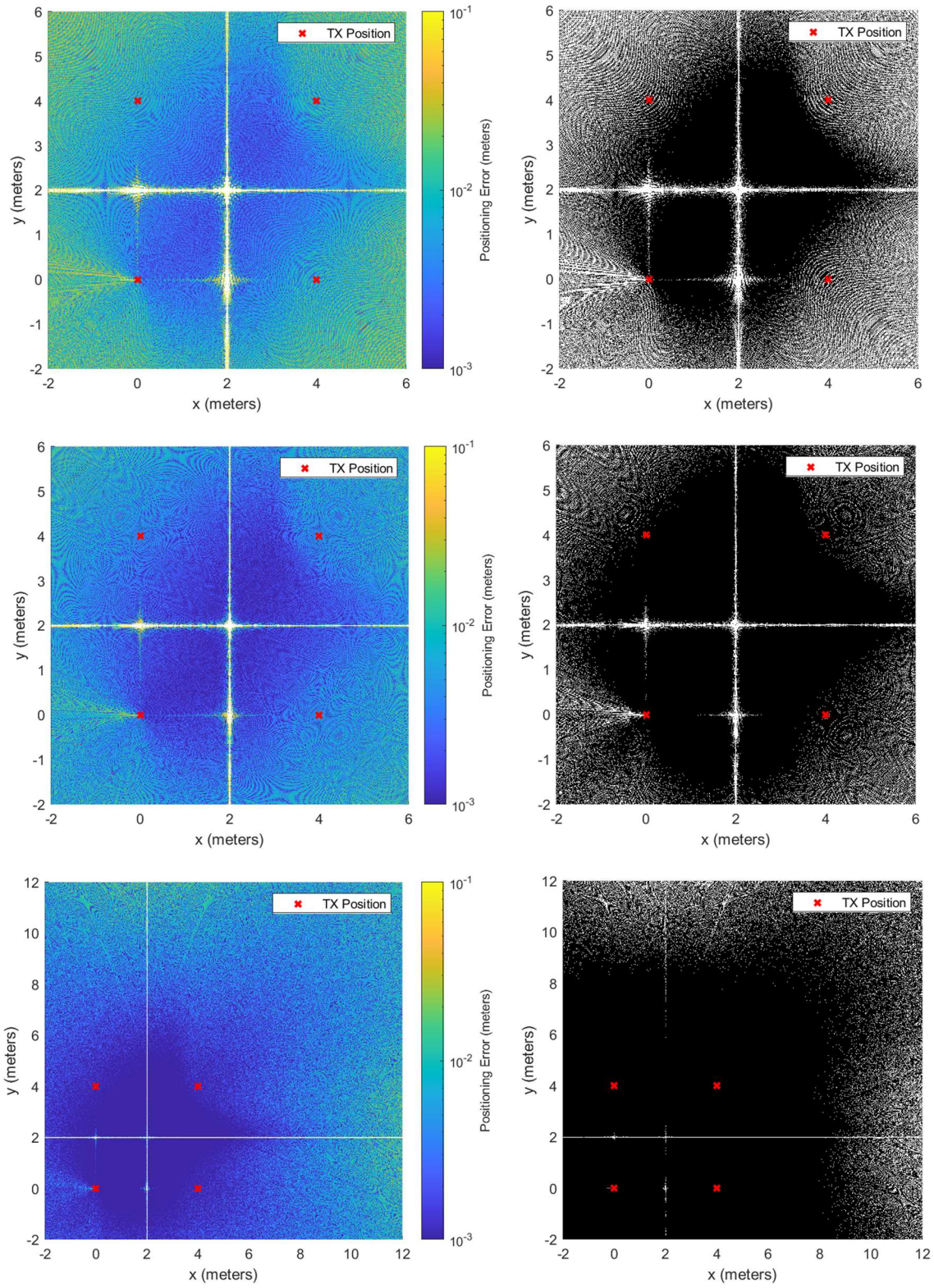

Figure 5.21: Positioning accuracy (left) and 1cm accuracy coverage map (right) with sampling frequency 44.1 kHz (top), increased by factor of 2 (middle) and increased by factor of 10 (bottom)

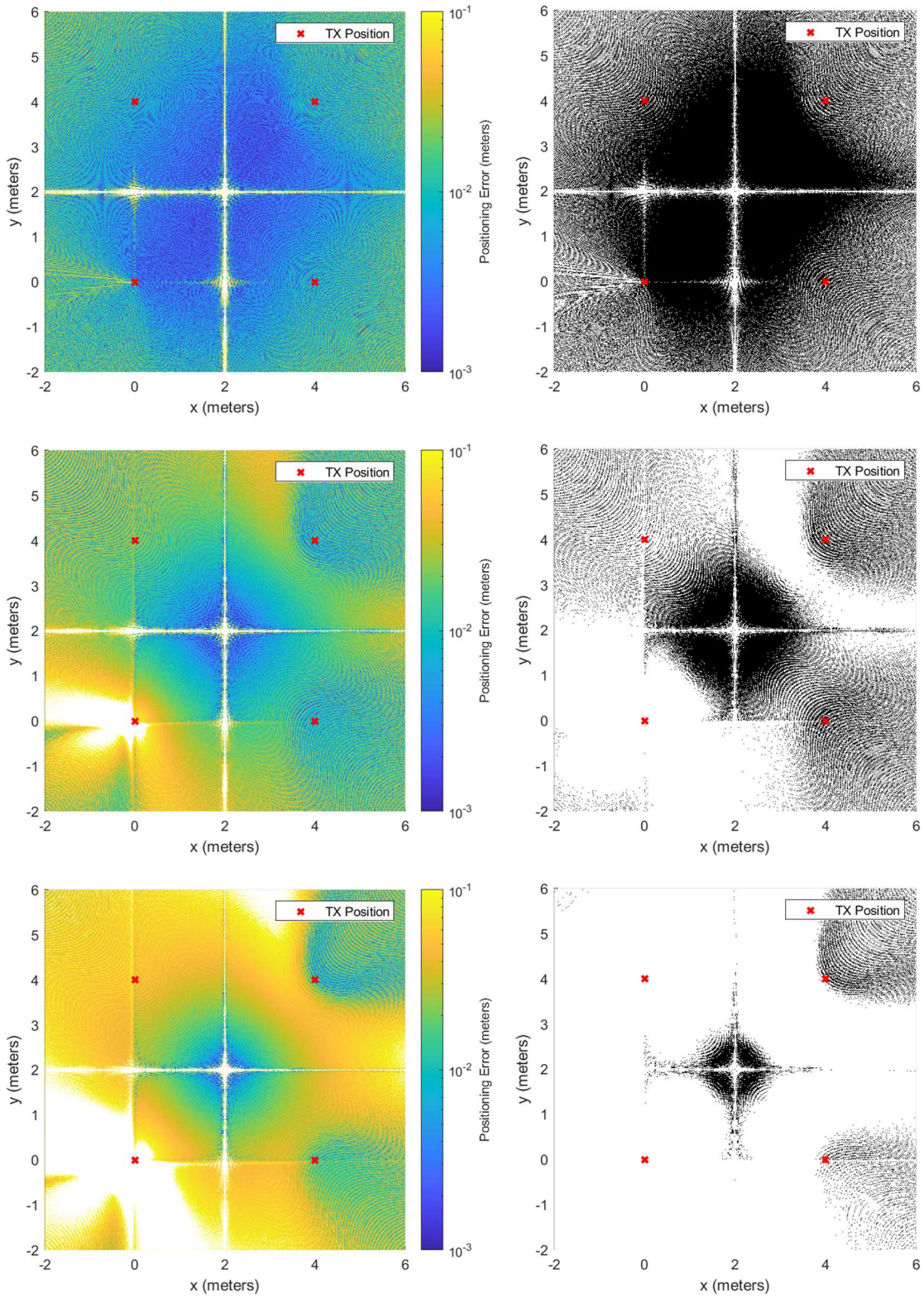

Figure 5.22: Positioning accuracy (left) and 1cm accuracy coverage map (right) when the object has a height, z, of 0m (top), 0.3m (middle) and 0.5m (bottom)

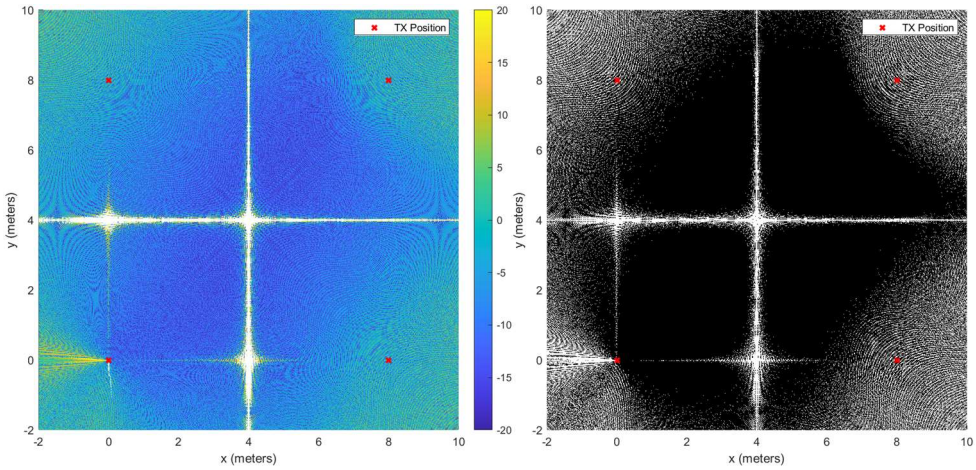

Figure 5.23: Positioning accuracy (left) and 1cm accuracy coverage map (right) using 4 transmitters spaced on an 8x8m grid

5.5.1.1 Transmitter Structure

Square Transmitter Structure

Figure 5.19 shows the simulated impact of different transmitter structures to the coverage map. The top row of Figure 5.19 shows the positioning accuracy and coverage map when four transmitters are placed on the corners of a 4x4m grid. Regions inside the transmitter array obtains consistent 1cm accurate coverage. Outside the enclosed region obtains spotty 1cm accurate coverage. Note that points on the crosshair running through the grid have ambiguous solutions. This is due to the symmetry of the transmitter structure. Moving transmitter positions moves the blind spots.

Arc Transmitter Structure

The middle row of Figure 5.19 shows the transmitters placed on an arc shape and the bottom row shows the transmitters in a triangle formation. The arc has poor performance since many ambiguous solutions exist. Again, the structure performs best within the transmitter array. Interestingly, the region of consistent 1cm coverage also extends outside the region enclosed by the transmitters. The structure still suffers from a crosshair of blind spots that runs through the consistent 1cm coverage region.

Triangle Transmitter Structure

The triangle formation, shown in the bottom row of Figure 5.19, moves the top right transmitter to the center

of the grid to form a right triangle. Moving the far transmitter to the center significantly improves the consistent 1cm coverage area. The crosshair of blind spots that used to run through the grid is no longer there. Instead, blind lines radiate from the corners of the triangle pointing into unenclosed space. This behavior is favorable since unenclosed space is likely outside the physical room where the object to be located exists. Additionally, the consistent 1cm coverage area is not split anymore like it was in the arc and square formation. Note that the triangle formation is more susceptible to the near-far problem. Section 6.1.1 discusses the near-far problem.

There may be more optimum four transmitter structures not presented in Figure 5.19. In many cases, the optimum transmitter formation is likely application dependent. The main factors include possible transmitters mounting locations and the location of desired region of consistent coverage.

5.5.1.2 Number of Transmitters

Figure 5.20 shows the simulated impact of additional transmitters on the coverage map. Again, the top row shows the positioning accuracy and coverage map when 4 transmitters are placed on the corners of a 4x4m grid. In the middle map, a 5th transmitter is placed on the y-axis at the 2m mark halfway between the other two transmitters on the y-axis. In the bottom map, a 6th transmitter is placed on the right edge of the 4x4m grid halfway between the other two transmitters on the right edge.

Five Transmiters

With five transmitters, the crosshair of blind spots that ran through the enclosed region disappears. The 5th transmitter disrupts the structure's symmetry and provides sufficient TDoA information so points on the crosshair are no longer ambiguous. Additionally, the 1cm consistent coverage area extends closer to the left edge and corners of the 4x4m grid, but moves away from the right edge and corners.

Six Transmiters

Adding the 6th transmitter gives marginal improvement. The 1cm consistent coverage area moves closer to the right edge, which was not covered in the 5-transmitter structure. It loses some coverage towards the top left corner, however.

As seen previously in Figure 5.19, the coverage map is sensitive to transmitter location. Similarly, it was just seen in that adding transmitters can also reshape the coverage map. The biggest improvements came after adding a 5th transmitter, which eliminated ROI blind spots.

5.5.1.3 Sampling Frequency

Figure 5.21 shows the impact of sampling frequency on the coverage map. Recall that increasing the sampling frequency decreases the ranging resolution, which generally increases positioning accuracy [45]. Again, the top row shows the positioning accuracy and coverage map when 4 transmitters are placed on the corners of a 4x4m grid. The middle row and bottom rows show the coverage map when increasing the sampling frequency by a factor of 2 and 10 respectively.

Increasing by Factor of 2

As seen in the middle row, increasing the sampling frequency by a factor of 2 to 88.2 kHz significantly increases positioning accuracy and the coverage map. The consistent 1cm coverage map area extends to the corners of the grid, which outperforms the 5 and 6 transmitter structures presented in Figure 5.20. The square transmitter structure is still susceptible to the crosshair of blind spots that runs through the square. However, increasing the sampling frequency thins the crosshair.

Increasing by Factor of 10

Again, increasing the sampling frequency by a factor of to 10 to 441 kHz significantly increases positioning accuracy and the coverage map. The map is rescaled to show where the coverage begins to break down. The consistent 1cm coverage area extends 4m beyond the edges of the enclosed transmitter square. Additionally, the crosshair blind region is further thinned.

Figure 5.21 demonstrates that increasing sampling frequency and ranging resolution can lead to excellent positioning accuracy and coverage map gains. Recall from Section 5.2 that a higher sampling frequency imposes a stricter calibration constraint. Increasing the sampling frequency by a factor of 10 to over 400 kHz yields a calibration constraint of less than 0.5mm. Such a calibration constraint is not practical to measure manually, nor is it an easy task when transmitters are spaced by multiple meters.

Another important note is a sampling frequency of 44.1 kHz only requires code acquisition. Code tracking is not necessary when the sampling frequency corresponds to one sample per chip. Increasing the sampling frequency also increases computational resources and power consumption. Doubling the sampling frequency also doubles the integrate and dump correlator in the code tracking DLL for each transmitter the receiver is tracking. So, increasing the sampling frequency is extremely computationally costly.

5.5.1.4 Introducing Variation in z Direction

A 2D simulation with no variation in the z direction does not accurately model all IPS. When the transmitter locations are close together, object z coordinate variation is not negligible. Object variation in the z direction introduces ranging error on the 2D scale. This ranging error leads to increased 2D positioning error. Figure 5.22 shows the impact of object z height variation from the 2D transmitter plane on positioning accuracy. The top middle and bottom row show the positioning error and coverage map when the object has a z height of 0m, 0.3m and 0.5m respectively.

A general trend seen is that as z increases, positioning accuracy and coverage map performance decreases. The consistent 1cm coverage area shrinks towards the center of the transmitters. This effect is representative of the small angle theorem. Small z variation relative to xy Euclidian distance to transmitters minimizes coplanar ranging error.

Despite the reduced performance as z increases, a majority of the region enclosed by the transmitters is still solvable and gives an accuracy of 10cm. This means object variation in the z direction is tolerable, within reason. So, a 2D positioning algorithm is still valid for some IPS applications. A priori application information about object z height to select transmitter z height can help minimize error.

5.5.1.5 Positioning Simulation Takeaways

The simulation proves the proposed IPS can achieve sub-centimeter accuracy with Chan and Ho's method. The simulation also shows that the positioning accuracy and coverage map is highly infrastructure and receiver dependent. Studying novel positioning algorithms will further enhance the positioning accuracy and coverage map of the proposed IPS.

Figure 5.23 shows a larger square grid of 8x8m. The 8x8m grid shows the same coverage pattern as the 4x4m grid. So, observations made with the 4x4m grid are scalable to different grid sizes reasonably.

6 FUTURE WORK

6.1.1 Near-Far Problem

The near-far problem occurs when a strong signal from a near source makes it difficult to decode a weak signal from a distant source. This problem is especially relevant in CDMA networks [10]. The proposed IPS uses a CDMA approach, so is also prone to the near-far problem. Because of the near-far problem, there may be additional blind areas in the coverage map close to transmitters. Increasing the PN sequence length increases noise immunity, but slows down the system. It also increases computational resources required for correlation.

The problem would be less of an issue in a flipped version of the IPS where the infrastructure consists of receivers. Note, this is only true with a small number of users and is only practical in certain applications.

Nonetheless, the near-far problem was not studied in this paper. Section 5.5.1 simulated the coverage map assuming theoretical TDoA measurements at every location. The simulation does not consider locations that suffer from the near-far problem. Studying the near-far problem will reveal the "true" coverage map of the proposed IPS.

6.1.2 3D Implementation

Many indoor positioning applications are more of a 3D problem, than a 2D problem. For that reason, a 3D implementation is vital to the practicality of the system. A high precision 3D IPS will open the door to many applications including mapping, robotics control and tracking, as well as unforeseen applications with big market potential. A 3D implementation will require an in-depth literature review on the latest positioning algorithms and infrastructure node location optimizations. This paper cites three 3D TDoA positioning algorithms [28] [24].

6.1.3 Real-Time Systems

Real time implementations of the proposed IPS will likely be application dependent. A universal implementation of the proposed IPS does not exist largely due to variable indoor environments. The application defines the infrastructure, which defines the desired positioning accuracy.

The proposed IPS is still quite modular despite the requirement for application dependent implementations. A receiver to be located only needs to know the PN codes and infrastructure node locations to leverage a system. Communication via Bluetooth, WiFi, etc. could easily transfer the information. Seamless transition between IPS similar to handover between cell towers and satellites is conceivable. The use of Bluetooth or WiFi could also allow for receiver, transmitter synchronization in ToA measurements, opening the door to more IPS opportunities

Note that the author has a parallel acquisition and tracking design partially implemented in HDL. The design would work with the custom receiver board and allow for real-time TDoA measurements. Developing a software receiver with the Galaxy Prime is an alternative to the hardware implementation as a real-time receiver. Either implementation brings opportunity to study the proposed IPS with a moving object.

7 CONCLUSION

This paper studies an acoustic PN based TDoA IPS solution. The proposed IPS uses an infrastructure of synchronized transmitters, that each transmit a unique and orthogonal Gold code. The user of the system, or object to be located makes TDoA measurements and calculates its position. One major advantage of the proposed IPS is that infrastructure and receiver hardware requirements are inexpensive and allow existing devices to leverage the system. The proposed IPS is a large and complex system, where many factors affect overall system performance. Some major factors include the system impulse response, code tracking, sampling frequency, the calibration requirement, transmitter locations, and the positioning algorithm. Studying the proposed IPS is important to the fast growing field of IPS.

The proposed IPS requires a phase and magnitude correction filter to correct the system impulse response so accurate code acquisition is possible. As seen in Section 4.3.2, the pre-corrected system impulse response is odd symmetric and has significant ringing, which would lead to code acquisition errors. A TR filter corrects the phase and a linear phase FIR filter corrects the magnitude of the system impulse response. Phase correction is important to achieve an even symmetric impulse response, and magnitude correction is important to reduce impulse response ringing. As seen in Section 4.4.5, correcting the magnitude of a system to achieve a flat PSD significantly reduced impulse response ringing. In the Snowball Ice microphone case, magnitude correction reduced ringing from approximately 75% of the peak, to below 30% of the peak. Both phase and magnitude correction filters are vital to code acquisition and symbol decoding performance. An even symmetric impulse response with minimal ringing is ideal for code acquisition and symbol decoding performance.

This paper also proves the proposed IPS can achieve accurate ranging measurements. The calibration requirement determines the ranging accuracy between a transmitter and receiver. The calibration requirement is directly related to the system sampling frequency which also determines the resolution of ranging measurements. The calibration requirement is important because it directly impacts the resolution and accuracy of ranging measurements. Increasing the sampling frequency may not improve system accuracy if the system is not calibrated to the given sampling frequency. TDoA and multipath measurement tests used the calibration requirement and obtained results accurate within half the sampling period. This level of

accuracy is acceptable and proves the proposed IPS can extract accurate TDoA information and can therefore locate an object.

The 2D Chan and Ho's positioning simulation proves the proposed IPS can achieve sub-centimeter accuracy with a sampling frequency of 44.1 kHz and a 4-transmitter square structure. Adding a 5^{th} transmitter eliminates ambiguous solutions that runs through the square in a crosshair shape. Increasing the sampling frequency significantly improves the coverage map and system accuracy. However, recall that increasing the sampling frequency also requires more computational resources in the correlators and requires code tracking. A system with a 44.1 kHz sampling frequency only has one sample per chip, and only requires code acquisition. The simulation shows that system accuracy is sensitive to transmitter locations, and sampling frequency. Using a 2D positioning algorithm limits coverage to a 2D plane, and positioning accuracy diminishes when the receiver has 3D variation off the plane. Studying 3D positioning algorithms in future works will improve the coverage map and system accuracy. Note that the near-far problem was not taken into account in the simulation. Studying the near-far problem with the proposed IPS will reveal the true coverage map of the system. Nonetheless, the Chan and Ho's 2D positioning simulation provides a strong foundation for future work with the proposed IPS.

This paper experimentally proves the fundamental theory behind an acoustic PN based TDoA IPS. The sub-centimeter accuracy achieved in simulation makes the proposed IPS look promising for high precision, inexpensive IPS applications. Future work involves studying improvements to the proposed IPS coverage map and real-time implementations. It is important to note that the proposed IPS reuses many existing techniques that have already been extensively studied, but not necessarily applied to IPS yet. This is a major advantage, since there is an abundance of available literature for researching issues associated with the proposed IPS and future works.

REFERENCES

[1] Brena, Ramon & García-Vázquez, Juan & Galván Tejada, Carlos & Munoz, D. & Vargas-Rosales, Cesar & Fangmeyer Jr, James & Palma, Alberto. (2017). Evolution of Indoor Positioning Technologies: A Survey. Journal of Sensors. 2017. 10.1155/2017/2630413.

[2] M. O. Khyam, M. Noor-A-Rahim, X. Li, C. Ritz, Y. L. Guan and S. S. Ge, "Design of Chirp Waveforms for Multiple-Access Ultrasonic Indoor Positioning," in IEEE Sensors Journal, vol. 18, no. 15, pp. 6375-6390, 1 Aug.1, 2018, doi: 10.1109/JSEN.2018.2846481.

[3] C. Medina, J. Segura, and Á. De la Torre, “Ultrasound Indoor Positioning System Based on a Low-Power Wireless Sensor Network Providing Sub-Centimeter Accuracy,” Sensors, vol. 13, no. 3, pp. 3501–3526, Mar. 2013.

[4] Li, Jian & Han, Guangjie & Zhu, Chunsheng & Sun, Guiqing. (2016). An Indoor Ultrasonic Positioning System Based on TOA for Internet of Things. Mobile Information Systems. 2016. 1-10. 10.1155/2016/4502867.

[5] Ito, Nobuo & Iyota, Taketoshi. (2011). Verification of CDMA and accuracy on echo ranging system using spread spectrum ultrasonic signals. 476-479. 10.1109/ICARA.2011.6144840.

[6] S. Cao, X. Chen, X. Zhang and X. Chen, "Effective Audio Signal Arrival Time Detection Algorithm for Realization of Robust Acoustic Indoor Positioning," in IEEE Transactions on Instrumentation and Measurement, doi: 10.1109/TIM.2020.2981985.

[7] T. Suzuki and S. Ogiso, "The effect of the mixture ratio of audible positioning signal and music on the signal and sound quality," 2019 IEEE 8th Global Conference on Consumer Electronics (GCCE), Osaka, Japan, 2019, pp. 850-852, doi: 10.1109/GCCE46687.2019.9015242.

[8] G. Feferman, M. Blatt and A. Eilam, "Indoor Positioning with Unsynchronized Sound Sources," 2018 IEEE International Conference on the Science of Electrical Engineering in Israel (ICSEE), Eilat, Israel, 2018, pp. 1-4, doi: 10.1109/ICSEE.2018.8646313.

[9] Y.Nakashima, R. Kaneto, and N. Babaguchi, “Indoor positioning system using digital audio watermarking,” Transactions on Information and Systems, vol.94, no.11, pp.2201–2211, 2011.

[10] Guimaraes, Dayan Adionel. Digital Transmission: A Simulation-Aided Introduction with VisSim/Comm. 1st Ed. 2009. ed. Berlin, Heidelberg: Springer Berlin Heidelberg : Imprint: Springer, 2009. Signals and Communication Technology. Web.

[11] B. P. Kumar and C. S. Paidimarry, "Development and analysis of C/A code generation of GPS receiver in FPGA and DSP," 2014 Recent Advances in Engineering and Computational Sciences (RAECS), Chandigarh, 2014, pp. 1-5, doi: 10.1109/RAECS.2014.6799658.

[12] S. Traithavil, "Simulation of PN Code Sequences for Cellular Systems," The Australian National University, 2006.

[13] "Global Positioning System (GPS) Standard Positioning Service (SPS) Performance Standard", 4th edition, approved by DoD Position, Navigation, and Timing Executive Committee, Sept. 2008. <https://www.gps.gov/technical/ps/2008-SPS-performance-standard.pdf>.

[14] D. Plaušinaitis. (2009). Code Tracking; Multipath [Slides]. Available: http://kom.aau.dk/~dpl/courses/mm13_slides.pdf

[15] B. N. Vu and M. Andrle, "The code and carrier tracking loops for GPS signal," Proceedings of the 16th International Conference on Mechatronics - Mechatronika 2014, Brno, 2014, pp. 569-574, doi: 10.1109/MECHATRONIKA.2014.7018322.

[16] Chih-Cheng Sun and Shau-Shiun Jan, "GNSS signal acquisition and tracking using a parallel approach," 2008 IEEE/ION Position, Location and Navigation Symposium, Monterey, CA, 2008, pp. 1332-1340, doi: 10.1109/PLANS.2008.4570121.

[17] S. Lohan. (2009). Lecture 3: Basics of code acquisition and tracking [Slides]. Available: http://www.cs.tut.fi/kurssit/TLT-5606/Lec3_TLT5606_S.pdf

[18] Y. Zheng, "A software-based frequency domain parallel acquisition algorithm for GPS signal," 2010 International Conference on Anti-Counterfeiting, Security and Identification, Chengdu, 2010, pp. 298-301, doi: 10.1109/ICASID.2010.5551340.

[19] L. Cheng, K. Wang, M. Ren and G. Yan, "Adaptive Filter Approach for GPS Multipath Estimation Under Correntropy Criterion in Dynamic Multipath Environment," in IEEE Transactions on Signal Processing, vol. 67, no. 22, pp. 5798-5810, 15 Nov.15, 2019, doi: 10.1109/TSP.2019.2946028.

[20] N. Jardak and N. Samama, "Short Multipath Insensitive Code Loop Discriminator," in IEEE Transactions on Aerospace and Electronic Systems, vol. 46, no. 1, pp. 278-295, Jan. 2010, doi: 10.1109/TAES.2010.5417162.

[21] S. Potluri, “Hyperbolic Position Location Estimator with TDOAs From Four Stations,” M.S. thesis, Department of Electrical and Computer Engineering, New Jersey Institute of Technology, NJ, 2002.

[22] Kossonou, Ignace & El hillali, Yassin & Bocquet, Michael & Menhaj, Atika & Assaad, Jamal. (2014). Non-iterative three dimensional positioning algorithm based on time difference of arrival technique.

[23] Le, Trung-Kien & Ono, Nobutaka. (2016). Closed-Form and Near Closed-Form Solutions for TDOA-Based Joint Source and Sensor Localization. IEEE Transactions on Signal Processing. PP. 1-1. 10.1109/TSP.2016.2633784.

[24] Lee, Kyunghoon & Hwang, Wonjun & Ryu, Hyunseok & Choi, Hyung-Jin. (2017). New TDOA-based three-dimensional positioning method for 3GPP LTE system. ETRI Journal. 39. 264-274. 10.4218/etrij.17.0116.0554.

[25] M. Khalaf-Allah, "An extended closed-form least-squares solution for three-dimensional hyperbolic geolocation," 2014 IEEE Symposium on Industrial Electronics & Applications (ISIEA), Kota Kinabalu, 2014, pp. 7-11, doi: 10.1109/ISIEA.2014.8049862.

[26] Wu, & Su, Liangbin & Zuo, & Anfu, Guo & Sun, Zhongmin & Wen,. (2019). Time Difference of Arrival (TDoA) Localization Combining Weighted Least Squares and Firefly Algorithm. Sensors. 19. 2554. 10.3390/s19112554.

[27] Jin, Bonan & Xu, Xiaosu & Zhang, Tao. (2018). Robust Time-Difference-of-Arrival (TDOA) Localization Using Weighted Least Squares with Cone Tangent Plane Constraint. Sensors (Basel, Switzerland). 18. 10.3390/s18030778.

[28] Díez-González, Javier & Álvarez, Rubén & Sánchez, Lidia & Fernández-Robles, Laura & Perez, Hilde & Limas, Manuel. (2019). 3D Tdoa Problem Solution with Four Receiving Nodes. Sensors. 19. 2892. 10.3390/s19132892.

[29] Y. T. Chan and K. C. Ho, "An efficient closed-form localization solution from time difference of arrival measurements," Proceedings of ICASSP '94. IEEE International Conference on Acoustics, Speech and Signal Processing, Adelaide, SA, 1994, pp. II/393-II/396 vol.2, doi: 10.1109/ICASSP.1994.389638.

[30] "Logitech S120 2.0 Stereo Speakers." Amazon.com. <https://www.amazon.com/Logitech-S120-2-0-Stereo-Speakers/dp/B000R9AAJA>.

[31] CUI Inc. CMC-6015-42P. <https://www.cuidevices.com/product/resource/cmc-6015-42p.pdf>.

[32] J. Caldwell. "Single-Supply, Electret Microphone Pre-Amplifier Reference Design," Texas Instruments, 2015. < http://www.ti.com/lit/ug/tidu765/tidu765.pdf?&ts=1589661745073>.

[33] Maxim Integrated. "Analog Filter Design Demystified," Feb 2003. <https://www.maximintegrated.com/en/design/technical-documents/tutorials/1/1795.html>.

[34] S. Norcross and J. Bradley, "Comparison of room impulse response measurement methods", Canadian Acoustics, vol. 22, no. 3, pp. 47-48, Sep. 1994.

[35] Blue. Snowball Ice. < https://s3.amazonaws.com/cd.bluemic.com/pdf/manuals/snowball-ice/Blue_Snowball_iCE_QuickStart-EN.pdf>.

[36] Wancheng Zhang, A. W. H. Khong and P. A. Naylor, "Adaptive inverse filtering of room acoustics," 2008 42nd Asilomar Conference on Signals, Systems and Computers, Pacific Grove, CA, 2008, pp. 788-792, doi: 10.1109/ACSSC.2008.5074517.

[37] H. Yu, Class Lecture, Topic: "Adaptive Filters – Introduction." EE515, College of Engineering, Cal Poly, San Luis Obispo, Nov., 2019.

[38] J. G. Proakis and D. K. Manolakis, "Adaptive Filters," in Digital Signal Processing, 4th ed. Upper Saddle River, NJ, USA. of Prentice-Hall, Inc., 2006, ch. 13, pp. 880–909.

[39] W. M. Dyab, T. K. Sarkar and M. Salazar-Palma, "Time reversal compared to inverse filtering," Proceedings of the 2012 IEEE International Symposium on Antennas and Propagation, Chicago, IL, 2012, pp. 1-2, doi: 10.1109/APS.2012.6348873.

[40] Y. Chen et al., "Time-Reversal Wireless Paradigm for Green Internet of Things: An Overview," in IEEE Internet of Things Journal, vol. 1, no. 1, pp. 81-98, Feb. 2014, doi: 10.1109/JIOT.2014.2308838.

[41] Tanter, Mickaël & Thomas, J & Fink, Mathias. (2000). Time reversal and the inverse filter. The Journal of the Acoustical Society of America. 108. 223-34. 10.1121/1.429459.

[42] W. Pilkington, Class Lecture, Topic: “FIR Filter Design.” EE419, College of Engineering, Cal Poly, San Luis Obispo, Mar., 2019.

[43] K. P. Pushpavathi and B. Kanmani, "Frequency Sampling method of FIR Filter design: A comparative study," 2018 International Conference on Electrical, Electronics, Communication, Computer, and Optimization Techniques (ICEECCOT), Msyuru, India, 2018, pp. 588-595, doi: 10.1109/ICEECCOT43722.2018.9001661.

[44] “ARDUINO UNO R3 [A000066].” Amazon.com. <https://www.amazon.com/Arduino-A000066-ARDUINO-UNO-R3/dp/B008GRTSV6/ref=sr_1_3?dchild=1&keywords=arduino+uno&qid=1589693496&sr=8-3>.

[45] Thorbjornsen, Bjorn & White, Neil & Brown, Andrew & Reeve, Jeffrey. (2010). Radio Frequency (RF) Time-of-Flight Ranging for Wireless Sensor Networks. Measurement Science and Technology. 21. 035202. 10.1088/0957-0233/21/3/035202.

APPENDICES

I – GPS Gold Code Generation

Figure 8.1 shows a GPS C/A code generator. Note that Coarse/Acquisition (C/A) codes are Gold codes. The generator uses two MLS generators, G1 and G2. Equations (8.1) and (8.2) represent the generation polynomials for G1 and G2 respectively. Xoring the 10^{th} bit of G1 with the xor product of two tap points in G2 yields the C/A code. Figure 8.1 uses tap points at the 2^{nd} and 6^{th} bit indexes. The tap points determine the satellite ID [11].

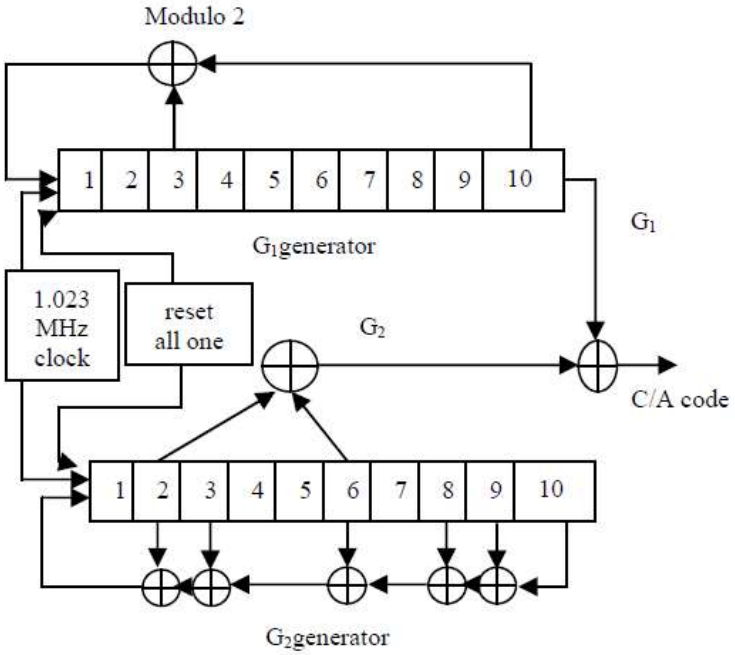

Figure 8.1: GPS C/A code generator where "+" is logical xor [11]

$$f_1(x) = x^{10} + x^3 + 1 \quad (8.1)$$

$$f_2(x) = x^{10} + x^9 + x^6 + x^3 + x^2 + 1 \quad (8.2)$$

II – Euclidian Distance Error Derivation Due To Quantization

$$d = \sqrt{(x_1 - x_2)^2 + (y_1 - y_2)^2 + (z_1 - z_2)^2}$$

$$d + \Delta d = \sqrt{(\Delta x + \varepsilon)^2 + (\Delta y + \varepsilon)^2 + (\Delta z + \varepsilon)^2}$$

$$d + \Delta d = \sqrt{(\Delta x)^2 + (\Delta y)^2 + (\Delta z)^2 + 2\varepsilon(\Delta x + \Delta y + \Delta z) + 3\varepsilon^2}$$

$$d^2 + 2d\Delta d + \Delta d^2 = \Delta d^2 + 2\varepsilon(\Delta x + \Delta y + \Delta z) + 3\varepsilon^2$$

$$\Delta d^2 + 2d\Delta d - (2\varepsilon(\Delta x + \Delta y + \Delta z) + 3\varepsilon^2) = 0$$

$$\Delta d = \frac{-2d \pm \sqrt{4d^2 + 4(2\varepsilon(\Delta x + \Delta y + \Delta z) + 3\varepsilon^2)}}{2}$$ Quadratic Equation

$$2\varepsilon(\Delta x + \Delta y + \Delta z) + 3\varepsilon^2 \approx 2\varepsilon(\Delta x + \Delta y + \Delta z)$$ For small ε

$$\Delta d \approx \frac{-d \pm \sqrt{d^2 + 2\varepsilon(\Delta x + \Delta y + \Delta z)}}{1}$$

$$\frac{\Delta d}{d} \approx -1 \pm \sqrt{1 + \frac{2\varepsilon(\Delta x + \Delta y + \Delta z)}{d^2}}$$

$$\sqrt{1 + x} \cong 1 + \frac{x}{2}$$ Taylor Approx.

$$\frac{\Delta d}{d} \approx -1 \pm 1 + \frac{\varepsilon(\Delta x + \Delta y + \Delta z)}{d^2}$$

$$\Delta \boldsymbol{d} \approx \frac{\boldsymbol{\varepsilon}(\Delta \boldsymbol{x} + \Delta \boldsymbol{y} + \Delta \boldsymbol{z})}{\boldsymbol{d}}$$

$$Max\ when\ \Delta x = \Delta y = \Delta z$$

$$d = \sqrt{3(\Delta x)^2}$$

$$\max(\Delta d) \approx \frac{\varepsilon(3\Delta x)}{\sqrt{3(\Delta x)^2}}$$

$$\max(\Delta d) \approx \frac{3}{\sqrt{3}}\varepsilon$$

$$\mathbf{max}(\Delta \boldsymbol{d}) \approx \sqrt{\mathbf{3}}\boldsymbol{\varepsilon}$$

III – 2D Positioning Coverage Map Simulation Pseudocode

1. Initialize grid size, resolution, infrastructure node locations, sampling frequency
2. For each point in the grid
    a. Calculate Euclidian distance in meters to each node
    b. Convert distances to time (assume 343 m/s speed of sound)
    c. Get time differences between each measurement
    d. Quantize time difference measurements according to sampling frequency
    e. Use Chan's method to compute 2D location
    f. Calculate Euclidian distance error between Chan's method and actual position
    g. Label point with the error
3. Display errors as an image